The Suzaku Technical Description

Version: October, 2006

Announcement of Opportunity #2

Institute of Space and Astronautical Science (ISAS/JAXA)
and the
X–ray Astrophysics Laboratory
NASA/Goddard Space Flight Center

Contents

List of Figures

List of Tables

1

Chapter 1

Introduction

Suzaku is the fifth in the series of Japanese astronomy satellites devoted to observations of celestial X–ray sources, following the highly successful Hakucho, Tenma, Ginga and *ASCA* satellites. Like *ASCA*, *Suzaku* is a joint Japanese-US mission, developed by the Institute of Space and Astronautical Science (part of the Japan Aerospace Exploration Agency, ISAS/JAXA) in collaboration with the National Aeronautics and Space Administration's Goddard Space Flight Center (NASA/GSFC) and many other institutions. *Suzaku* was launched on a Japanese M-V rocket on July 10, 2005 from the JAXA Uchinoura Space Center. Despite initial success, on August 8, 2005 a thermal short between the helium and neon tanks resulted in the liquid helium coolant venting to space, leaving the X–Ray Spectrometer (XRS) inoperable. However, the X–ray Imaging Spectrometer (XIS) and Hard X-ray Detector (HXD) are all working well. As a result, *Suzaku* retains its excellent X–ray sensitivity, with high throughput over a broad-band energy range of 0.2 to 600 keV. *Suzaku*'s broad bandpass, low background, and good CCD resolution makes it a unique tool capable of addressing a variety of outstanding problems in astrophysics.

Guest observing time on *Suzaku* will be awarded on a competitive basis and proposals will be judged on their scientific merits and their relevance to *Suzaku* observing capabilities. The overall purpose of this document is to aid potential users of *Suzaku* in proposing for time during the Guest Observer (GO) phase of the mission. In particular, upon reading this document, the proposer should be able to determine whether or not *Suzaku* is best suited to conduct the investigation in question. This should be demonstrated in the proposal, preferably using simulations of the proposed observations. All proposals should clearly answer the following four questions:

1. Is *Suzaku* capable of the proposed observation?

2. Is it the best available instrument for the investigation?

3. When can *Suzaku* observe a given source?

4. How much exposure time is required to meet the scientific goals?

Chapter 2 summarizes the principal characteristics of the detectors on-board *Suzaku*. Chapter 3 covers how the satellite time will be allocated. This includes the data rights and available time for GOs, as well as policies regarding Targets of Opportunity (TOOs). In addition, observational constraints due to the orbit, sun angle, and the pointing accuracy are described. Finally, the proposal process is reviewed, including how to submit a proposal, how they will be evaluated, and how observations will be scheduled, performed, and the results disseminated. US proposers should note especially the NASA requirements regarding the relevance of the proposed science to NASA's mission.

Chapter 4 explains how to write a strong proposal, including a summary of what constraints must be met, and what must be included in the proposal. In most cases, existing X–ray data can be used to estimate the likely *Suzaku* count rates. Simulation tools, including **XSPEC** and **PIMMS**, will assist in this and are covered in detail with examples.

The last three chapters describe the telescopes and instruments on *Suzaku*. Chapter 5 covers the five X–ray Telescopes (XRTs) on *Suzaku*. Chapter 6 reviews the X–ray Imaging Spectrometers (XISs), four CCDs with moderate spectral resolution and a large field of view. Chapter 7 explains the operation of the Hard X–ray Detector (HXD), which extends the high energy bandpass of *Suzaku* to 600 keV.

Disclaimer:

This document was prepared using the best current knowledge of the *Suzaku* satellite by the *Suzaku* teams at ISAS/JAXA and NASA/GSFC as of October 2006. It is possible that information contained in this document may contain inadvertent errors or omissions. We welcome suggestions for corrections or clarifications. Revisions of this document will be available on the *Suzaku* Web sites listed in Appendix C. Users interested in more details can also access the different instrument papers.

1. Spacecraft paper:
   `ftp://legacy.gsfc.nasa.gov/suzaku/doc/general/suzakumemo-2006-33.pdf`

2. XRT paper:
   `ftp://legacy.gsfc.nasa.gov/suzaku/doc/xrt/suzakumemo-2006-34.pdf`

3. XIS instrument paper:
   `ftp://legacy.gsfc.nasa.gov/suzaku/doc/xis/suzakumemo-2006-35.pdf`

4. XIS simulations paper:
   `ftp://legacy.gsfc.nasa.gov/suzaku/doc/xis/suzakumemo-2006-39.pdf`

5. HXD instrument paper:
   `ftp://legacy.gsfc.nasa.gov/suzaku/doc/hxd/suzakumemo-2006-36.pdf`

6. HXD in-flight performance paper:
   `ftp://legacy.gsfc.nasa.gov/suzaku/doc/hxd/suzakumemo-2006-37.pdf`

Chapter 2

Mission Description

This chapter is a brief introduction to the satellite and its instruments, and is intended as a simplified guide for the proposer. Reading it thoroughly should provide the reader with the necessary information to understand the capabilities of the instruments at a level sufficient to prepare the feasibility section of an *Suzaku* proposal.

In its first year of operation, *Suzaku* has accumulated data from calibration, SWG and GO observations. The list of all observations performed is available at `http://suzaku.gsfc.nasa.gov/docs/suzaku/aehp_time_miss.html`.

Suzaku is in many ways similar to ASCA in terms of orbit, pointing, and tracking capabilities. *Suzaku* uses the same station (USC) as ASCA did for uplink and downlink, although downlink at NASA DSN is not possible with Suzaku (see footnote in subsection 2.2.2). As a result, the operational constraints for *Suzaku* are also similar to those of ASCA. *Suzaku* is placed in a near-circular orbit with an apogee of 568 km, an inclination of 31.9 degrees, and an orbital period of about 96 minutes. The maximum slew rate of the spacecraft is 6 degrees/min, and settling to the final attitude takes ~ 10 minutes, using the star trackers. The normal mode of operations will have the spacecraft pointing in a single direction for at least 1/4 day (10 ksec; but see "raster-scanning" in section 2.2.1). With this constraint, most targets will be occulted by the Earth for about one third of each orbit, but some objects near the orbital poles can be observed nearly continuously. The observing efficiency of the satellite as measured after a year of operation is about 45%.

2.1 A Brief Introduction to *Suzaku*

The scientific payload of *Suzaku* (Fig. 2.2) initially consisted of three distinct co-aligned scientific instruments. There are four X–ray sensitive imaging CCD cameras (X–ray Imaging Spectrometers, or XISs), three front-illuminated (FI; energy range 0.4-12 keV) and

4
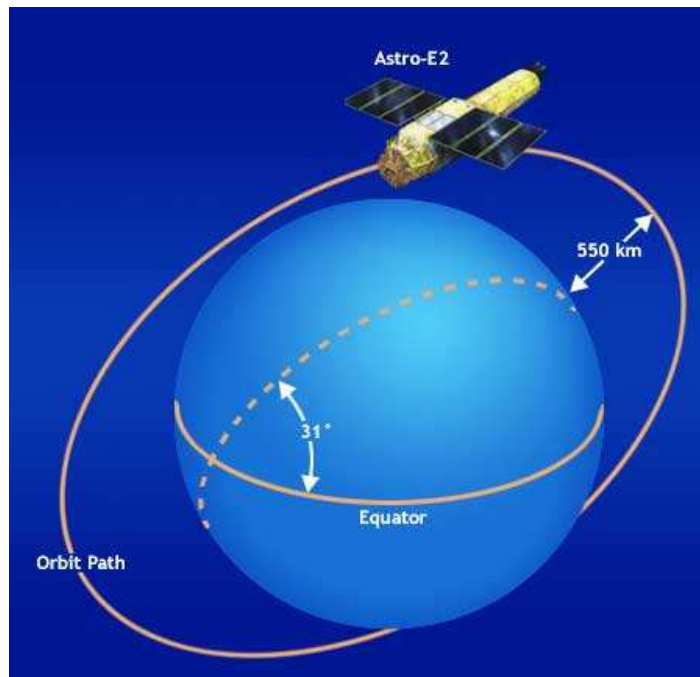
Figure 2.1: The 96 minute *Suzaku* orbit.
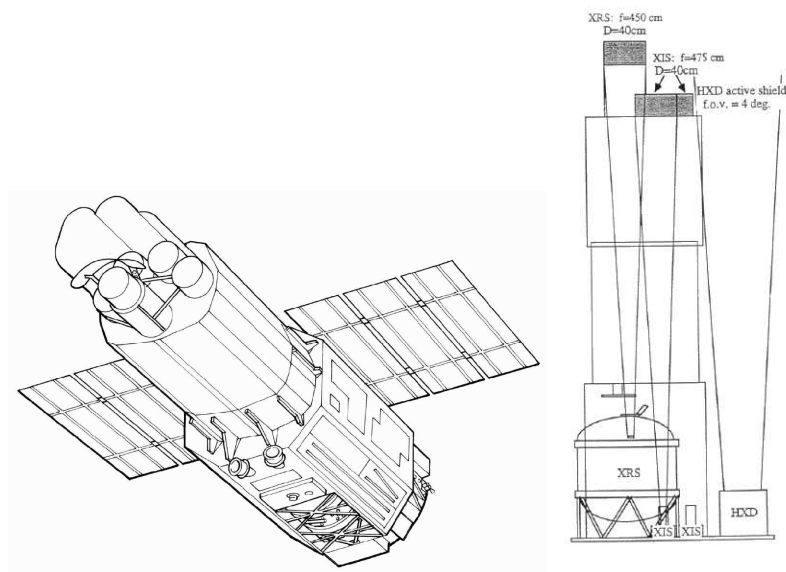
Figure 2.2: [Left] Schematic picture of the bottom of the *Suzaku* satellite. [Right] A side view of the instrument and telescopes on *Suzaku*.

S/C	Orbit Apogee	568 km
	Orbital Period	96 minutes
	Observing Efficiency	$\sim 45\%$
XRT	Focal length	4.75 m
	Field of View	$17'$ at 1.5 keV
		$13'$ at 8 keV
	Plate scale	0.724 arcmin/mm
	Effective Area	440 cm^2 at 1.5 keV
		250 cm^2 at 8 keV
	Angular Resolution	$2'$ (HPD)
XIS	Field of View	$17.8' \times 17.8'$
	Bandpass	0.2–12 keV
	Pixel grid	1024×1024
	Pixel size	24 μm× 24 μm
	Energy Resolution	~ 130 eV at 6 keV
	Effective Area	340 cm^2 (FI), 390 cm^2 (BI) at 1.5 keV
	(incl XRT-I)	150 cm^2 (FI), 100 cm^2 (BI) at 8 keV
	Time Resolution	8 s (Normal mode), 7.8 ms (P-Sum mode)
HXD	Field of View	$4.5° \times 4.5°$ ($\gtrsim 100$ keV)
	Field of View	$34' \times 34'$ ($\lesssim 100$ keV)
	Bandpass	$10 - 600$ keV
	– PIN	$10 - 70$ keV
	– GSO	$40 - 600$ keV
	Energy Resolution (PIN)	~ 4.0 keV (FWHM)
	Energy Resolution (GSO)	$7.6/\sqrt{E_{MeV}}$ % (FWHM)
	Effective area	~ 160 cm^2 at 20 keV, ~ 260 cm^2 at 100 keV
	Time Resolution	61 μs
HXD-WAM	Field of View	2π (non-pointing)
	Bandpass	50 keV – 5 MeV
	Effective Area	800 cm^2 at 100 keV / 400 cm^2 at 1 MeV
	Time Resolution	31.25 ms for GRB, 1 s for All-Sky-Monitor

Table 2.1: Overview of *Suzaku* capabilities

one back-illuminated (BI; energy range 0.2-12 keV), capable of moderate energy resolution. Each XIS is located in the focal plane of a dedicated X–ray telescope. The second instrument is the non-imaging, collimated Hard X–ray Detector (HXD), which extends the bandpass of the observatory to much higher energies with its 10–600 keV pointed bandpass. The X–Ray Spectrometer (XRS) is no longer operational, and will not be discussed further. Interested readers are invited to access the XRS instrument paper at http://www.astro.isas.jaxa.jp/suzaku/doc/suzakumemo/suzakumemo-2006-38.pdf.
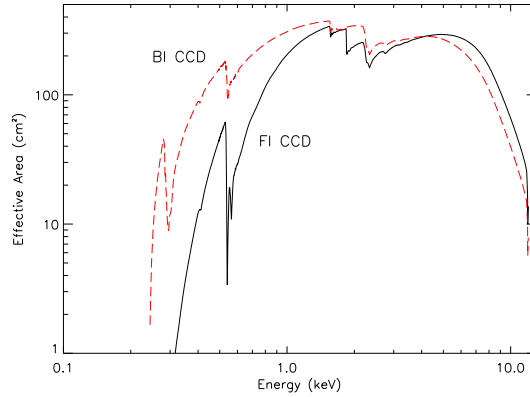
Figure 2.3: XIS Effective area of one XRT + XIS system, for both the FI and BI chips. (No contamination included)

All of the instruments on *Suzaku* operate simultaneously. Each of the co-aligned XRTs features an X–ray mirror with an angular resolution (expressed as Half-Power Diameter, or HPD) of $\sim 2'$ (cf. Fig. 2.4). Figure 2.3 shows the total effective area of the XIS+XRT, which includes features due to the elemental composition of the XIS and XRT. K-shell absorption edges from the oxygen (0.54 keV) and aluminum (1.56 keV) in the blocking filters are present, as well as a number of weak M-shell features between 2–3 keV arising from the gold in the XRT.

The four XISs (cf. Fig. 6.2) are true imagers, with a large field of view ($\sim 18' \times 18'$), and moderate spectral resolution.
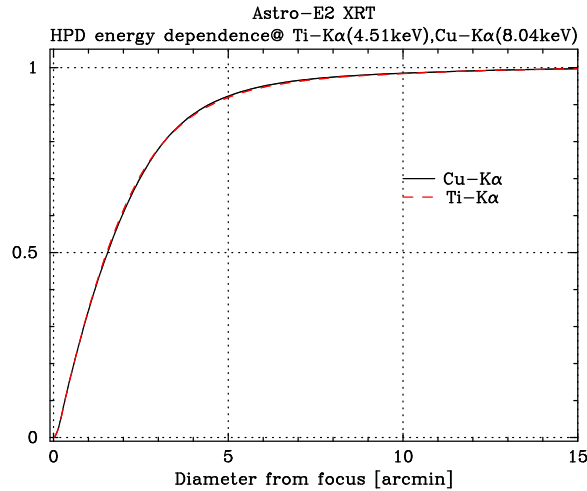
Figure 2.4: The Encircled Energy Function (EEF) showing the fractional energy within a given radius for one quadrant of the XRT-I telescopes on *Suzaku* at 4.5 and 8.0 keV.
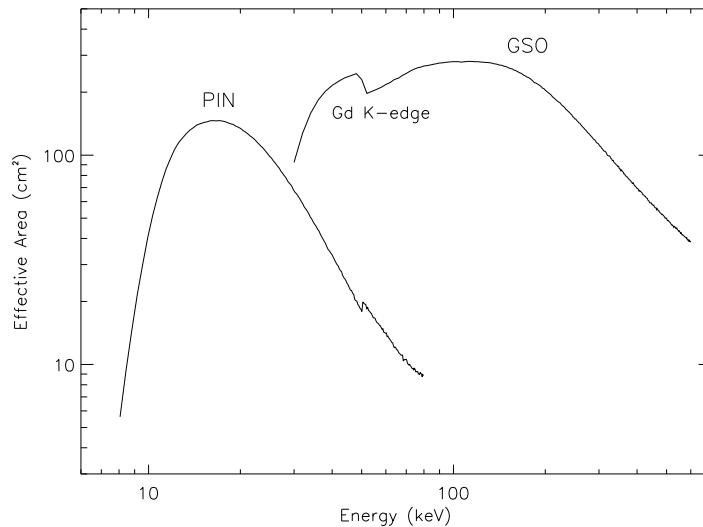
Figure 2.5: Total effective area of the HXD detectors, PIN and GSO, as a function of energy.

The HXD (cf. Fig. 7.1) is a non-imaging instrument with an effective area of $\sim 260\,\mathrm{cm^2}$, featuring a compound-eye configuration and an extremely low background. It dramatically extends the bandpass of the mission with its nominal sensitivity over the 10 – 600 keV band (cf. Fig. 2.5). The HXD consists of two types of sensors: 2 mm thick silicon PIN diodes sensitive over 10 – 70 keV, and GSO crystal scintillators placed behind the PIN diodes covering 40 – 600 keV. The HXD field of view is actively collimated to $4.5° \times 4.5°$ by the well-shaped BGO scintillators, which, in combination with the GSO scintillators, are arranged in the so-called phoswich configuration. At energies below ~ 100 keV, an additional passive collimation further reduces the field of view to $34' \times 34'$. The energy resolution is ~ 4.0 keV (FWHM) for the PIN diodes, and $7.6/\sqrt{E}$ % (FWHM) for the scintillators (where E is energy in MeV). The HXD time resolution for both sensors is 61 μs. While the HXD is intended mainly to explore the faintest hard X–ray sources, it can also tolerate very bright sources up to ~ 10 Crab. The HXD also performs as an all-sky monitor (the Wide-band All-sky Monitor (WAM), which can detect GRB and other sources. Although observers will receive data from the WAM, it cannot be proposed for directly and has special rules regarding data rights; see Chapter 3.

Because the HXD bore-sight axis, with the highest effective area, is about 3.5 arcmin shifted from that of the XISs, *Suzaku* supports two aimpoints, XIS and HXD oriented. Users are requested to select which pointing axis is best for your observations. For the XIS, choosing the XIS aimpoint provides a $\sim 10\%$ larger XIS effective area than the HXD aimpoint. Conversely for the HXD, the HXD aimpoint provides a $\sim 10\%$ larger

HXD effective area than the XIS aimpoint. Note that a 10% increase in effective area corresponds to a 20% increase in observing time for background dominated observations. For source dominated observations, the effect is 10%. Please take into account these effects in your observation plan.

2.2 Operational Constraints of *Suzaku*

2.2.1 Raster-scanning

While a substantial change of the spacecraft attitude (more than a few degrees) is time-consuming, small offsets can be made efficiently. Such offsets would require that no new stars need to be acquired by the star trackers, and thus are limited to $\sim 30'$. This is particularly useful in checking for point sources that in the HXD FOV but outside the XIS FOV. The minimum total time is still 10 ksec, and each point in the raster scan must be observed for at least 3 ksec. Raster-scanning observations over a regular grid can be specified as a single target with multiple observations. In this case, use the Remarks section to specify the details of rastering (such as "use 3 x 3 grid separated by 15 arcmin each"). For irregularly spaced pointings, the PI must specify each as a separate target with its own coordinates. If the raster-scan pattern is complex or unusual, PIs are encouraged to contact the *Suzaku* team at ISAS/JAXA or the NASA *Suzaku* GOF for assistance before submitting a proposal.

2.2.2 Telemetry rates

Suzaku carries a 6 Gbit data recorder. Data will be downlinked to USC at a rate of 4 Mbps for a total of 2 Gbits per pass, up to 5 times a day. This allows a maximum of 10 Gbits of data to be obtained per day, but fewer passes may be available to *Suzaku* as it will share the use of USC ground station with other ISAS satellites[1]. Data can be recorded at 4 different rates: Super-High (524 kbps), High (262 kbps), Medium (131 kbps), and Low (33 kbps). The recording rate will be changed frequently throughout an observation, according to a sequence that will be determined by the operations team at ISAS. This is to optimize the selection of the data rates and the usage of the data recorder, taking into account the expected count rates supplied by the proposers. Thus an accurate estimation of the count rates is important for the optimization of the mission operation. We emphasize that proposers cannot arbitrarily choose the data recording rate.

On-source data will usually be recorded at High (during contact orbits, during which the satellite passes over USC) or Medium (during remote orbits, without USC passes)

---

[1]Unlike ASCA, NASA DSN stations will not be used, since a 4 Mbps down-link is not possible at DSN stations.

data rate. The Low rate will primarily be used for times of Earth occultations and SAA passages, as the background rates in the XIS and HXD exceed their telemetry allocation limit at Low data rate. The telemetry limits for the XIS are presented in Chapter 6. The XIS data mode will be chosen for each data recording rate used to prevent telemetry saturation, based on the count rate supplied by the proposer.

2.2.3 Summary

Suzaku excels for observations such as:

- Studies of diffuse soft X-ray sources with low surface brightness: the low background, soft X-ray sensitivity, and near-Gaussian response of the XIS BI CCD makes such targets an excellent use of *Suzaku*.

- Observations requiring sensitivity both above and below 10 keV, especially measuring the Fe K complex simultaneously with the hard (> 10 keV) continuum.

- Rapid variability studies on 10 msec time scales. The best time resolution available on the XIS is ~ 7.8 ms, while the HXD time resolution is $\sim 61\mu$sec (see Table 2.1)

Suzaku is less appropriate for:

- Studies requiring primarily high spatial resolution. *Chandra*'s PSF is $\sim 100\times$ smaller than *Suzaku*'s, while the *XMM-Newton* PSF is $\sim 10\times$ smaller.

- Studies requiring primarily high spectral resolution. The gratings on *Chandra* and *XMM-Newton* have significantly higher resolution than the XIS.

2.3 *Suzaku* Calibration

Calibration observations for *Suzaku* started ~ 4 weeks after the launch. The list of all calibration targets done during Phase-1A can be found on the *Suzaku* websites listed in Appendix C.

Table 2.2 summarizes the calibration items of all scientific instruments, the current status, and their expected and measured accuracy.

These values are the 90% limits, equivalent to 1.6σ. Note that the values listed are those required from the scientific purpose and ultimate goals which are possible to be realized on the basis of the instrument design.

Table 2.2: Error Budgets of Scientific Instrument Calibrations

	Calibration Item	October 2006	October 2005	Requirement	Goal
XRT−I/XIS	On-axis effective area [a]	$\sim$2%	$\sim$10%	5%	5%
	Vignetting[a]	$\sim$10%	$\sim$50%	5%	2%
	On-axis EEF [b]	$\sim$20%	$\sim$20%	5%	1%
	Off-axis EEF [c]	$\sim$20%	$\sim$30%	20%	2%
	Optical axis position in XIS	$\sim$0.5$'$	$\sim$0.5$'$	$< 0.2'$	$<0.2'$
	Energy scale[d]	max(0.2%, 5eV)	0.3%	0.1%	0.1%
	Energy resolution (FWHM) at 5.9 keV	5%[e]	5%	1%	1%
	Contamination thickness[f]	10^{18}cm^{-2}	N/A	N/A	N/A
	OBF integrity	unbroken	unbroken	broken/unbroken	broken/unbroken
HXD	Absolute effective area	20%	20%	20%	5%
	Relative effective area	15%	10%	10%	5%
	Vignetting	5%	5%	10%	5%
	Background modeling (PIN)[g]	$3 \sim 5$%	5%	10%	1%
	Background modeling (GSO)[g]	$3 \sim 5$%	10%	10%	3%
	Absolute timing[h]	600 μs		300 μs	100 μs
	Relative timing[h]	3×10^{-8}		10^{-8}	10^{-10}
	GRB absolute timing	$\sim$2ms		100 ms	15 ms

Note $\cdots$ All the values quoted are preliminary.

a: Valid in 2-10 keV band. Calibration uncertainty may become larger outside this energy range, especially below 0.3 keV (BI chip) and above 10 keV. We calibrated the effective area using spectral parameters of the Crab emission as those given by Toor & Seward (1974, AJ, 79, 995)

b: For all integration radii from $1'$-$6'$. No error on attitude control is included.

c: As on-axis but for all XIS f.o.v. No calibration is currently scheduled.

d: For the normal mode data. Uncertainties of the energy scale increase when the burst and/or window options are applied.

e:When xisrmfgen is used. Note that an error of 5% in the energy resolution could produce an artificial line width of as large as $\sim$25 eV in sigma at the iron band. Energy resolution with the spaced-row charge injection is under investigation.

f:Uncertainty represented as the carbon-equivalent column density. Valid only at the center of the field of view.

g: Modeling accuracy depends on energy-band and exposure. See Chapter 7 for detail. Presented are example for 15-40 keV with 100 ks (PIN),and 50-100 keV with 100 ks (GSO), with rev1.2 BGD modeling. Study continues.

h: The Crab and PSR 1509 pulses are clearly detected in the quick look analysis of calibration data.

Chapter 3

Observation Policies

In AO2, 100% of the observing time available is used for GO observation. The current schedule for the time allocation between Japanese and US PI is given in Table 3.1. The AO will run for a year starting in April 2007. After a year of operation, we know that the actual observing efficiency is a little higher than the 37 ks per day estimated for AO1, but for the purpose of proposal selection, we assume the same (37 ks) good on-source time per day, and 360 days of operations per year. From the total of 13320 ks, we subtract 4% of the available time as observatory time used for satellite maintenance and similar purposes, and 3% for ongoing calibration observations. Finally, 5% is earmarked as Director's Discretionary Time (DDT) for unproposed Target of Opportunity (TOO) proposals (including observations of gamma-ray bursts) and other important observations, granted at the mission director's discretion. Therefore $13320 \times 0.88 = 11722$ ks are nominally available to the community via the proposal selection process.

The project will oversubscribe this total by 40% including category C targets whose observations are not guaranteed (see §3.4 below). If the actual sum of the observatory, calibration, and director's times is less than 12%, additional C targets will be observed.

In this AO, 50% of the total observing time is assigned to Japanese observations and 37.5% goes to US observations. The reminder 12.5% is set aside for Japan-US joint investigations. When the respective national reviews have selected the same target, the two proposals will be merged if both teams indicated their willingness to collaborate on the RPS form, and the observation will be counted against the Japan-US time. If such mergers do not take up 12.5% of total time, the remainder will be divided between separate Japanese and US investigations. An additional 8% of the total observing time from within the "Japanese" allocation, is reserved for proposals submitted to ESA as joint Japan-ESA observations. This means that the total time available to US researchers is 4396 ks, plus 1465 ks of joint time, identical to what it was for AO1. European (ESA) proposals will receive 938 ks of observing time. Proposals from non-US, non-ESA countries will be accepted within the Japanese time up to the ESA portion.

Phase	Months Post-Launch	SWG	Japan (ESA)	US	Japan/US
AO-2	21-32	0	50 (8)	37.5	12.5
AO-2		0	5861 ks (938 ks)	4396 ks	1465 ks

Table 3.1: *Suzaku* percentage (first line) and actual ks (second line) of time allocated to each group of observers The ESA time is in parentheses as it is part of the Japanese allotment.

The nationality of the PI's institution determines which agency should receive the proposal. That is, resident researchers at US institutions must submit their proposals to NASA and those at institutions in ESA member countries must submit theirs to ESA (regardless of their actual nationality). While the ISAS/JAXA proposal process is primarily aimed at researchers resident in Japan, proposals from researchers in other (non-US, non-ESA) countries will also be considered. In addition, Co-Is from any country may be part of any proposal.

3.1 Data Rights

The data rights policy for *Suzaku* is similar to previous missions. The normal exclusive period for both SWG and GO data is one year, except that all Phase Ia SWG science data will be made available at the end of this AO. DDT data are made public immediately.

During AO-2, category A and B targets will be considered complete if 90% (for A targets) or 70% (for B targets) of the proposed time is obtained on the source.

During the GO phase, data from calibration and TOOs requested outside the proposal process (see below) will not be considered proprietary.

Data taken during spacecraft maneuvers (often called "slew data") will be proceeded and made public immediately. Maneuver data is defined as data taken when the source out of the *Suzaku* FOV, defined as being more than 1° away. Observation time, however, will not begin until the source is stable in the FOV.

3.2 Target of Opportunity proposals

TOO proposals are allowed for *Suzaku* through the normal proposal process, although they must be ranked as category A targets (see below) to be accepted. Proposals with TOOs should not be mixed with non-TOO targets. TOO proposals are allowed for short-lived events on known objects whose timing is uncertain. These should only include unpredictable phenomena in a specific target (*e.g.* SS Cyg in outburst; "Triggered Observations" in *XMM-Newton* parlance), not a generic target (*e.g.* the next Galactic supernova). The

triggering criteria **must** be explicit and quantifiable, and stated in detail in the proposal text; a brief summary should appear in the Remarks section of the target form. In addition, TOO proposals **must** provide an estimated probability of a successful trigger during the AO-2 period. It **is** the PI's responsibility to notify the *Suzaku* project when the criteria are met. **Generic TOOs without a specific target (such as "a nearby supernova") will not be accepted. In the same spirit, the number of targets in TOO proposals should not exceed 5.** Gamma-ray bursts or any genuinely unpredictable events may be observed outside the proposal process, as part of the 5% DDT. Data from such observations will not have a proprietary period.

To request such unproposed TOO observations, please send an e-mail to:

    suzaku_managers@astro.isas.jaxa.jp

3.3 Pointing constraints

The Solar panels on the *Suzaku* satellite are fixed. This places a restriction on the pointing direction with respect to the satellite-Sun line: the Sun angle constraint is normally 65 – 110 degrees. This means that at any given time of the year, only a swath of the sky 45 degrees wide is accessible for astronomical observations, and thus most celestial sources are available for observations for about 50 days every 6 months. If a specific observing date or a coordinated observation with other missions is required, the proposer must first determine if the observation is possible. This can be done using the "Viewing" tool on the *Suzaku* proposal website (see Appendix C). **Note that a constrained observation must be ranked as Category A (see below) to be accepted.**

It is anticipated that long (>1 day) observations will be the norm for *Suzaku*, based on the *Suzaku* SWG target list. In addition, a large number of short observations is an inefficient use of the satellite because of the unusable time during slews and attitude settling. The pointing is expected to be accurate to 0.3 arcmin and can be reconstructed to better than 0.2 arcmin, except during the initial settling period of up to 10 minutes. Moreover, there is a limit on the number of slews that can be uploaded to *Suzaku*. For these reasons, a minimum exposure time of 10 ksec has been set for all proposed observations. However, raster observations over a small ($< 0.5°$) area of the sky may be allowed where the individual pointings are at least 3 ksec. For such observations, the total exposure time (which must still be at least 10 ksec) and the number of separate pointings should be entered into the RPS form. Particularly complicated operations may not be feasible; please contact either the ISAS/JAXA *Suzaku* team or the NASA *Suzaku* GOF for assistance on difficult or unusual observation plans.

There are also orbital constraints upon the orientation of the projection of the XIS CCDs on the sky. Since the *Suzaku* XIS arrays are square, with calibration sources in

different corners, selecting a specific roll angle is rarely significant. However, if a specific roll angle is scientifically advantageous, the proposer must first determine if it is allowed. This can be done using the MAKI tool described in §4.7. Then the required roll range can be entered on the RPS proposal form. For objects close to the ecliptic poles it is possible to arrange for any XIS orientation by scheduling observations at a specific time, but for those located close to the ecliptic, the XIS will project on the sky in a nearly fixed orientation. **Note that any roll constraint will make a proposal time critical.** Due to their increased overhead, only a fraction of the total available time can be used for constrained observations, and proposers should justify their requirements carefully.

During a pointed observation, there will be interruptions due to the location of *Suzaku* in a low Earth orbit. Normally, a target will be occulted by the Earth for ~30 minutes every satellite orbit. In addition, *Suzaku* will pass through the South Atlantic Anomaly (SAA) during parts of 5 or 6 orbits every day. Due to the harsh radiation environment of the SAA, scientific observation is not possible during SAA passages. There are other variations in the particle background, depending primarily on the cut-off rigidity[1]. The optimal criteria to reduce times of high background while maximizes the science return is still being determined from SWG observations; please check the *Suzaku* websites (see Appendix C) for the most up-to-date suggestions.

3.4   Sequence of events after submission

After the *Suzaku* proposal deadline, there will be three independent proposal reviews for the US, Japan, and ESA proposals. Each review will create a target list from the proposed observations, ranking the accepted targets as category A, B, or C. Only category A and B targets are guaranteed to be observed. As stated above, TOOs and constrained observations are only accepted if they are in category A. Category C targets will be observed as time permits, and will not be carried over into the next AO if not observed in this AO. An international merging committee will collate the three target lists and produce a single, unified list. Overlaps between US and Japanese targets will be resolved, either by merging the investigations (if both parties are willing) or by choosing one. In the latter process, the priority given by the national reviews, as well as the lengths of the accepted observations, will be considered. The final target list will be ~ 40% oversubscribed. Category A targets will have 50% of the available time, category B 40%, and category C 50%. US PIs, or US Co-Is on foreign PI projects, may propose for funding once notified that their target has been accepted. This process is described in ROSES-2006 document; further details of this process will be made available on the NASA *Suzaku* GOF website listed in Appendix C.

---

[1]*Suzaku* is protected from solar and cosmic-ray particles by the geomagnetic field; cut-off rigidity is an indicator of the minimum momentum required for a particle to reach a specific location, given the average geomagnetic field configuration.

Even though observations are scheduled to acquire roughly the approved exposure time, and ASCA experiences suggest this will usually be achieved with *Suzaku*, occasional losses of usable observation time are inevitable. As mentioned above, Category A observations will be deemed complete when they have received at least 90% of the approved time. Note that this will be judged based on the good time intervals of the cleaned XIS event files after the standard screening. Dead times (including those due to the use of the burst option) are not taken into account. Also, the standard screening for the HXD is more strict, so the effective exposure for the HXD is often smaller than that of the XIS by 20% or more. Additional observations will be scheduled automatically for non-time-critical targets whose observations are considered incomplete by the project scientist at ISAS. In the case of time-critical observations which are incomplete or unusable, it will be the PI's responsibility to determine the best course of action.

Each PI will be assigned a contact scientist, either at ISAS or the NASA *Suzaku* GOF, who will work with the PI to assure the maximum science return. This will include double-checking coordinates, count rates and finalizing configurations (nominal pointing, XIS modes,...). It is important to note that once an observation has been scheduled, any delay in responding to questions from the contact scientist may result in targets being removed from the schedule. We do not have a mechanism to approve coordinated observations with *Suzaku* and another observatory through a single proposal. It is the PI's responsibility to secure observing time with other observatories, when simultaneous observations are desirable. **Please note that the *Suzaku* component of such a proposal may be approved contingent on the success of other proposals.** Special scheduling request and TOOs will be accommodated on a best effort basis. For simultaneous observations, the mission scheduler at ISAS, in consultation with the contact scientist, will contact the PI in advance for detailed scheduling information, and will often work directly with schedulers of other missions. During AO1 observing period, the *Suzaku* scheduling team made all efforts to accommodate requests of coordinated/simulatenous observations with other facilities and we expect that it will continue to do so during AO2.

Once the observation has been completed, the data will be promptly run through the processing pipeline and put into both the US and Japanese archives, initially in encrypted form. The PI will be sent the decryption key along with instructions on how to download and decrypt the data. The only exception to the one year exclusive period for GO data, concerns the HXD Wide-band All-sky Monitor (WAM) data (see Chapter 7). The WAM is primarily used for anticoincidence shielding in the HXD, but it can also be used as an all-sky monitor, detecting solar flares, gamma-ray bursts, and other bright X-ray sources (*e.g.* Cyg X-1). All data from the WAM will be monitored by the HXD team, which will alert the GRB community to any detected bursts. In addition, the HXD team will make analysis results from WAM, such as light curves and fluences, available to the public as soon as possible. These may be used to put limits on GRBs or other events triggered by other satellites or observatories. However, the PI will receive the complete WAM data from

their observation and will share data rights with the *Suzaku* team for the normal 1 year proprietary period. This unusual arrangement is due to the time-critical and non-source-specific nature of the WAM data.

With the exception of the code that converts raw binary telemetry into FITS format files, all *Suzaku* software is written as FTOOLS and distributed through the *Suzaku* team at ISAS/JAXA and the NASA/GSFC HEASARC. This includes the tools used in the processing. All calibration files are distributed through the HEASARC `caldb` (Calibration Database) system. This enable users to apply any calibration updates themselves. The *Suzaku* team at ISAS and the NASA *Suzaku* GOF provide additional FTOOLS that may be necessary or desirable in analyzing *Suzaku* data. Use of other software packages will only be supported at a lower priority level.

Chapter 4

Guide to Writing A Successful *Suzaku* Proposal

Each *Suzaku* proposal must include at a minimum the source coordinates, exposure time, instrument configuration and expected count rates, and any observing constraints within the four page limit. The review panels will base their decision primarily upon the justification of the proposed science to be done with the data. This chapter describes how to prepare a strong proposal, including the various software tools available to assist the proposer.

4.1 First checks to do before starting

4.1.1 Using Viewing

One of the first tasks in preparing a proposal is determining when and for how long a target can be observed as there is very little use to simulate a source that cannot be observed. This can be easily done with Viewing, a simple Web-based interactive tool (see Appendix C) that can determine visibility for many different satellites. To use Viewing, simply enter the target name or coordinates, and select the satellite. Viewing will return all the available dates when that target is observable.

4.1.2 Previous Observations

Another initial check to be performed before starting sophisticated simulations it to ensure that the target has not yet been observed by *Suzaku*. At the time of the writing of this document, the observation database is not available via `Browse` but users can check the different target lists. The SWG target is available in Appendix B or on line at

`http://suzaku.gsfc.nasa.gov/docs/suzaku/tlminfo/swg_060829update.html`. The calibration is available at `http://suzaku.gsfc.nasa.gov/docs/suzaku/tlminfo/ao1_caltargets.html` while the list of accepted AO1 targets is at `http://suzaku.gsfc.nasa.gov/docs/suzaku/tlminfo/ao1list.html` Users should also check the observations log located at `http://suzaku.gsfc.nasa.gov/docs/suzaku/aehp_time_miss.html` as some of the targets (category C) may have been accepted but not observed.

4.2 Ingredients of a Successful *Suzaku* Proposal

While it is conceivable that one would wish to study a previously unknown X–ray source with *Suzaku*, a more likely scenario would involve a spectroscopic study of an object with known X–ray flux. A viable proposal should state the scientific objective of the observation and show that *Suzaku* can achieve this objective. Observations that require one or more of *Suzaku*'s unique capabilities would be especially strong canditates.

Every *Suzaku* proposal must have an estimate of the expected source count rates from the proposed target for all detectors. This rate is used both by the reviewers to evaluate the viability of the proposal and the operations team to evaluate any safety concerns. The simplest tool to use in estimating the expected XIS or HXD count rate is PIMMS. This tool is freely available as a stand-alone tool or on the Web as WebPIMMS (see Appendix C). The next level of detail is provided via simulations using XSPEC, and such simulations should provide significant insight into the expected spectrum obtained from a proposed observation. A brief guide to XSPEC simulations is given in § 4.4. In many case, this should be sufficient for a point source. There are also tools available to simulate imaging data, which may be useful for an extended source or a particularly bright source. In particular, the most powerful tool is `xissim`, which can use a FITS format image with an assumed spectral shape of the source to estimate the distribution of events in all elements of the XIS detectors.

4.3 Using PIMMS and WebPIMMS

This tool is an interactive, menu-driven program, which has an extensive HELP facility. It is also available as the web-based tool WebPIMMS. In either case, users specify the flux and spectral model with its parameters, and PIMMS/WebPIMMS returns the predicted counting rate. PIMMS/WebPIMMS can be used for a variety of other instruments, so if for instance the counting rate and spectrum of a given source observed with the ROSAT PSPC is known, it can calculate the flux, which in turn can be used as input to estimate the expected counting rates. The limitations of the input source must be considered carefully. For example, ROSAT had no significant response to X–rays above $\sim 2.4\,\mathrm{keV}$, and so is not useful when estimating the HXD GSO count rate.

4.4   Using XSPEC to Simulate an Observation

Perhaps the easiest tool for simulating X–ray spectra is the XSPEC program (a part of the XANADU software package), which is designed to run on a variety of computer platforms and operating systems and is freely distributed on the NASA GSFC HEASARC Website (see Appendix C). The simulation of an XIS or HXD observation requires the current instrument redistribution matrix (the so-called .rmf file) and the energy-dependent effective area of the instrument (the so-called .arf file), both available on the Web or via anonymous FTP (see Appendix C).

The procedure for simulations is relatively simple: if the XSPEC program is installed, one should start XSPEC making sure that the proper .rmf and .arf files are accessible. Within XSPEC, one should specify the spectral model, such as hot thermal plasma or the like (via the *model* command). Specifying the model will drive XSPEC to query for the model parameters (such as temperature and abundances for an APEC collisional plasma model), as well as normalization. The key command to create a simulated spectrum is the *fakeit* command, which will query for the redistribution response (the .rmf file), and the ancillary response (the .arf file) or in the case of the HXD for response matrices (.rsp files). The *fakeit* command also will request the simulated data filename, and the length of simulated observation. One can now use this file within XSPEC to determine the sensitivity of the simulated data file to changes in the model parameters. Users should adjust the normalization of their input models to reflect the actual count rate or flux (absorbed or unabsorbed) of their source.

4.4.1   Using WebSPEC to Simulate an Observation

Some of the features of XSPEC are also available as a web-based tool on the HEASARC website (see Appendix C). WebSPEC calls XSPEC behind the scenes, so all the issues described above apply here as well.

After selecting the instrument, WebSPEC allows the user to choose the spectral model, such as an absorbed collisional plasma or a power-law spectrum with an absorption component. The next page will then query for the model parameters (such as temperature and abundances for an APEC collisional plasma model), as well as normalization, exposure, upper and lower energies, and the number of bins to use in the spectral plot. WebSPEC will then create a simulated spectrum after clicking the "Show me the Spectrum" button, using the *fakeit* command. This folds the specified model through the instrument response and effective area, calculating the observed count rate and fluxes as well. WebSPEC will then allow one to download the postscript file of the spectrum, change the model parameters, or replot the data.

4.5   Examples

To show how to estimate the proper exposure, we include some simple examples of XIS and HXD observations that illustrate the process.

4.5.1   Detecting Faint Oxygen Emission from the Local Hot Bubble

The Local Hot Bubble is the proposed origin for at least some of the 1/4 keV emission seen in the ROSAT All-Sky Survey at all latitudes. Although *Suzaku* has some sensitivity at 1/4 keV, a more profitable approach to finding this emission is to detect the OVII emission that should accompany it. In this case we need to calculate the expected count rate from the OVII and compare it to the expected background.

We first need the expected flux, based on published papers or the PI's model. In this case, we expect the surface brightness to be 0.34 ph/cm^2/s/sr, based on a number of papers. Since the XIS field of view is $18' \times 18'$, this value corresponds to a total surface brightness in one XIS of 9.3×10^{-6} ph/cm^2/s. The next question is the effective area of the XIS instruments at the line energy. OVII is in fact a complex of lines, centered around 0.57 keV. Examining the effective area plots for the XIS in Chapter 2, we see that the effective area at 0.57 keV in the BI CCD is $\sim 140\,\mathrm{cm}^2$; for the FI CCDs it is $\sim 90\,\mathrm{cm}^2$. The curves shown on Fig **??** do not include the contamination effect. The computation below is only given as an example. **Please note that the more current effective area curves for the FI and BI CCDs can also be found by loading their responses into XSPEC and using the `plot efficiency` command.** *Warning*: The XIS .rmf response matrices are **not** normalized, and so must be combined with the .arf files to determine the total effective area. With the expected flux and the effective area, we can now determine the expected count rate in the BI and FI CCDs to be 1.3 and 0.87 cts/ks. This is obviously a extremely low count rate and so the expected background is very important. The resolution of the XIS is quite good, as shown in Chapter 6, at 0.57 keV a bin of width 60 eV will contain most of the emission. The XIS background rate (see §6.8) at this energy is only 0.05 cts/s/keV in both the FI and BI detectors, so we can expect a background of 3 cts/ks. In both the FI and BI detectors the line will be below the background, but this does not intrinsically hinder detection. As will be seen below, in the HXD this is the norm rather than the exception. One aid for this observation is that the OVII line is relatively isolated in this energy range, with the exception of the nearby OVIII line. Assume we wish to detect the OVII feature with 3σ significance. Then the total count rate in the XIS-S1 (the BI CCD) in our energy band will be 4.3 cts/ks, with 3 cts/ks of background. In an N ks observation, we will measure the signal to be $1.3 \times N \pm \sqrt{4.3 \times N}$. To achieve a 3σ result, then, we need $1.3 \times N/\sqrt{4.3 \times N} > 3$, or $N > 23\,\mathrm{ks}$.

4.5.2 Detecting the hard tail of an XRB

Another common observation will be to search for faint hard X–ray tails from sources such as X–ray binaries. We describe here how to simulate such an observation, including the all-important HXD background systematics, which will dominate all such observations.

The first step is to download the latest versions of the background template files and the response files from the website listed in Appendix C. The HXD website will also describe the current best value for the systematic error in background estimation. For this AO, proposers should carefully read Chap.7 and evaluate the systematic errors for the PIN and the GSO backgrounds in the energy band of interest, and at the exposure level chosen and not just "use a number". For example, with 100 ks exposure, the value for PIN in the 15-40 keV band is 3%, and that for the GSO in the 50-100 keV is 3%. Since these energy bands are important in this case, the associated errors should be first estimated and then, used in the procedure described below. In addition, the proposer should also check if contaminating sources exist in the FOV of the HXD, using existing hard X–ray source catalogs from satellite such as RXTE-ASM, INTEGRAL, and Swift, before beginning this process.

We set up XSPEC to use these by reading the background template files as both data and background along with the response files.

```
XSPEC12>data ae_hxd_pinbkg_20060929.pha ae_hxd_gsobkg_20060929.pha


2 spectra  in use

Source File: ae_hxd_pinbkg_20060929.pha
Net count rate (cts/s) for Spectrum:1  5.709e-01 +/- 8.934e-04
 Assigned to Data Group 1 and Plot Group 1
  Noticed Channels:  1-256
  Telescope: SUZAKU Instrument: HXD  Channel Type: PI
  Exposure Time: 7.153e+05 sec
 No response loaded.

Source File: ae_hxd_gsobkg_20060929.pha
Net count rate (cts/s) for Spectrum:2  3.643e+01 +/- 3.626e-02
 Assigned to Data Group 1 and Plot Group 2
  Noticed Channels:  1-512
  Telescope: SUZAKU Instrument: HXD  Channel Type: PI
  Exposure Time: 2.771e+04 sec
 No response loaded.
```

```
    ***Warning!  One or more spectra are missing responses,
                 and are not suitable for fit.
    XSPEC12>back ae_hxd_pinbkg_20060929.pha ae_hxd_gsobkg_20060929.pha
    Net count rate (cts/s) for Spectrum:1  -0.000e+00 +/- 1.263e-03 (-0.0 % total)
    Net count rate (cts/s) for Spectrum:2  -0.000e+00 +/- 5.128e-02 (-0.0 % total)
    ***Warning!  One or more spectra are missing responses,
                 and are not suitable for fit.
    XSPEC12>resp ae_hxd_pinhxnom_20060814.rsp ae_hxd_gsohxnom_20060321.rsp
    Response successfully loaded.
    ***Warning: Detected response matrix energy bin value = 0 (or neg).
        XSPEC will instead use small finite value (response file will not be altered).
    Response successfully loaded.
    XSPEC12>
```

Now we assume a spectrum for our source; here, we use a Crab-like spectrum (photon index 2.1) with a 10 mCrab flux. This can be set up in XSPEC via the following commands:

```
    XSPEC12>model powerlaw

    Input parameter value, delta, min, bot, top, and max values for ...
                  1        0.01           -3          -2          9           10
    1:powerlaw:PhoIndex>2.1
                  1        0.01            0           0        1e+24       1e+24
    2:powerlaw:norm>0.08


    ========================================================================
    Model powerlaw<1> Source No.: 1   Active/On
    Model Model Component  Parameter  Unit       Value
     par  comp
       1    1   powerlaw   PhoIndex              2.10000       +/-  0.0
       2    1   powerlaw   norm                  8.00000E-02  +/-  0.0

    ------------------------------------------------------------------------


     Chi-Squared =        164109.3 using 768 PHA bins.
     Reduced chi-squared =       214.2419 for    766 degrees of freedom
     Null hypothesis probability =   0.000000e+00
     Valid fit does not exist.
    XSPEC12>
```

Now we can create fake PIN and GSO data with the "fakeit" command. The result

will be simulated spectral files which include the instrumental background, effective area, and resolution.

```
XSPEC12>fakeit
 Use counting statistics in creating fake data? (y): y
 Input optional fake file prefix:
 Fake data file name (ae_hxd_pinbkg_20060929.fak): pin_10mCrab_100ks.fak
 Exposure time, correction norm (715271., 1.00000): 1e+5
 Fake data file name (ae_hxd_gsobkg_20060929.fak): gso_10mCrab_100ks.fak
 Exposure time, correction norm (27708.8, 1.00000): 1e+5

No ARF will be applied to fake spectrum #1

No ARF will be applied to fake spectrum #2
XSPEC12>
```

We have now created our 'faked' spectral files, named `pin_10mCrab_100ks.fak` and `gso_10mCrab_100ks.fak`. Now we fit these datasets with the same Crab-like model. We will use three different background spectral models–low, medium, and high–which vary by as much as 3% for the PIN and 5% for the GSO. This takes into account the fact that the "true" background will likely vary within these limits. One item of note is that we do **not** use the "faked" background files afterwards which were also created by the fakeit command. That process assumes that the background is obtained together with the actual observation, *e.g.* using the outer region of the CCD image. In an HXD observation, this is not the case. The background is generated by modeling from the database, and users should use the template background throughout the simulation and also the future analysis.

We load the background files twice, once as background and once as a correction file ("corfile") which will allow us to easily vary the total background within XSPEC.

```
XSPEC12>back ae_hxd_pinbkg_20060929.pha ae_hxd_gsobkg_20060929.pha
Net count rate (cts/s) for Spectrum:1  4.741e-01 +/- 3.354e-03 (45.4 % total)
Net count rate (cts/s) for Spectrum:2  2.732e-01 +/- 4.101e-02 (0.7 % total)

 Chi-Squared =          402.11 using 768 PHA bins.
 Reduced chi-squared =        0.52494 for     766 degrees of freedom
 Null hypothesis probability =   1.000000e+00
 Valid fit does not exist.
XSPEC12>corfile ae_hxd_pinbkg_20060929.pha ae_hxd_gsobkg_20060929.pha
Net count rate (cts/s) for Spectrum:1  -9.678e-02 +/- 3.354e-03 (-20.4 % total)
 After correction of 5.709e-01 (using cornorm 1.000)
Net correction flux: 0.570921
```

```
  Net count rate (cts/s) for Spectrum:2  -3.616e+01 +/- 4.101e-02 (-13234.4 % total)
   After correction of 3.643e+01 (using cornorm 1.000)
  Net correction flux: 36.4349


  Chi-Squared =        820773.2 using 768 PHA bins.
  Reduced chi-squared =       1071.505 for     766 degrees of freedom
  Null hypothesis probability =   0.000000e+00
  Valid fit does not exist.
 XSPEC12>
```

All the necessary data files are now loaded, and we now experiment with different background levels, set by the value of "cornorm". A value of 0 gives the "normal" background, for example, and 0.05 increases it by 5%.

```
 XSPEC12>cornorm 1 2 0.0
  Spectrum 1 correction norm set to 0
  Spectrum 2 correction norm set to 0

  Chi-Squared =         402.11 using 768 PHA bins.
  Reduced chi-squared =       0.52494 for     766 degrees of freedom
  Null hypothesis probability =   1.000000e+00
  Valid fit does not exist.
 XSPEC12>ignore 1:**-8.0 2:**-30.0 600.0-**

     21 channels (1-21) ignored in source #     1
     15 channels (1-15) ignored in source #     2
    213 channels (300-512) ignored in source #    2
  Chi-Squared =         372.97 using 519 PHA bins.
  Reduced chi-squared =       0.72142 for     517 degrees of freedom
  Null hypothesis probability =   9.999996e-01
  Valid fit does not exist.

 XSPEC12>setplot energy
 XSPEC12>setplot rebin 3 30
 XSPEC12> fit
  renorm: no renormalization necessary

 Chi-Squared  Lvl Par #         1              2
 371.19        -3    2.12717       0.0859883
 371.017       -4    2.13012       0.0869248
 371.017       -5    2.13          0.0869009
```

```
==============================
 Variances and Principal Axes
                  1        2
 5.23E-04 |   -0.97     -0.23
 3.32E-07 |    0.23     -0.97
-----------------------------


=======================
  Covariance Matrix
   1           2
4.941e-04   1.192e-04
1.192e-04   2.910e-05
-----------------------


=========================================================================
Model powerlaw<1> Source No.: 1   Active/On
Model Model Component  Parameter  Unit      Value
 par  comp
   1    1    powerlaw   PhoIndex             2.13000       +/-  2.22290E-02
   2    1    powerlaw   norm                 8.69009E-02  +/-  5.39471E-03

-------------------------------------------------------------------------


 Chi-Squared =          371.02 using 519 PHA bins.
 Reduced chi-squared =       0.71763 for     517 degrees of freedom
 Null hypothesis probability =   9.999998e-01
XSPEC12>plot ldata res
```

This result in the plot shown in 4.1.

Now we check that the same source signal would be detectable with a high background taken to be 3% for the PIN and 5% for the GSO.

```
XSPEC12>cornorm 1 2 0.03 0.05
 Spectrum 1 correction norm set to 0.03
 Spectrum 2 correction norm set to 0.03
 Spectrum 2 correction norm set to 0.05

 Chi-Squared =         2241.79 using 519 PHA bins.
 Reduced chi-squared =       4.33616 for     517 degrees of freedom
 Null hypothesis probability =   1.066435e-212
 Valid fit does not exist.
XSPEC12>fit
```

Power–law 2.1/0.08 –– 100 ks ––– PIN/GSO ––– corfile norm =0
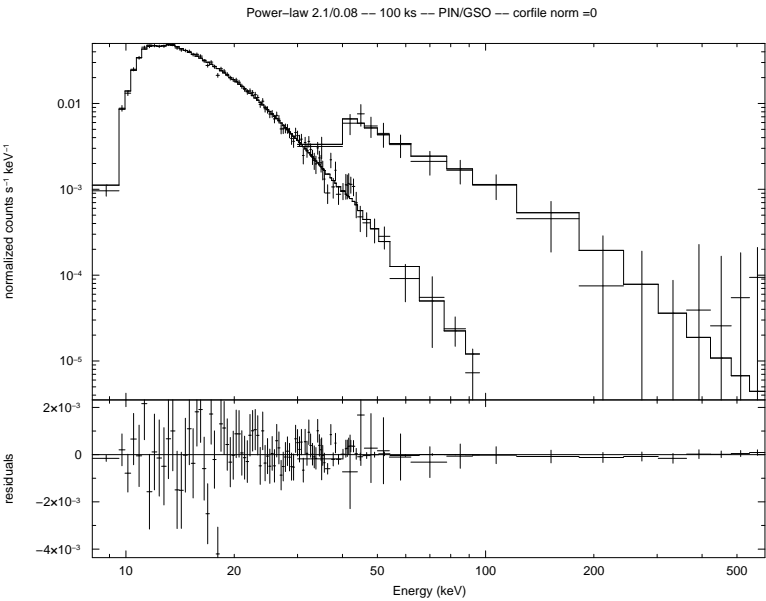
Figure 4.1: First simulation with cornorm of the two background files put to 0.

```
renorm: no renormalization necessary

Chi-Squared  Lvl Par #          1             2
2140.84        -2    2.22739       0.106249
2117.04        -2    2.27366       0.122154
2111.9         -3    2.33389       0.143755
2108.09        -4    2.32609       0.142699
2108.08        -5    2.32845       0.143611
==============================
 Variances and Principal Axes
                  1          2
 7.08E-04 |   -0.93      -0.36
 8.98E-07 |    0.36      -0.93
------------------------------


========================
  Covariance Matrix
    1            2
6.145e-04   2.398e-04
2.398e-04   9.462e-05
------------------------
```

```
========================================================================
Model powerlaw<1> Source No.: 1   Active/On
Model Model Component  Parameter  Unit       Value
 par  comp
   1    1   powerlaw   PhoIndex               2.32845      +/-  2.47885E-02
   2    1   powerlaw   norm                   0.143611     +/-  9.72724E-03

------------------------------------------------------------------------


  Chi-Squared =          2108.08 using 519 PHA bins.
  Reduced chi-squared =         4.07753 for      517 degrees of freedom
  Null hypothesis probability =  1.564232e-190
XSPEC12>plot ldata res
```

This result in the plot shown in Fig.4.2, and it clear from that figure that the signal is undetectable at all in the GSO band.
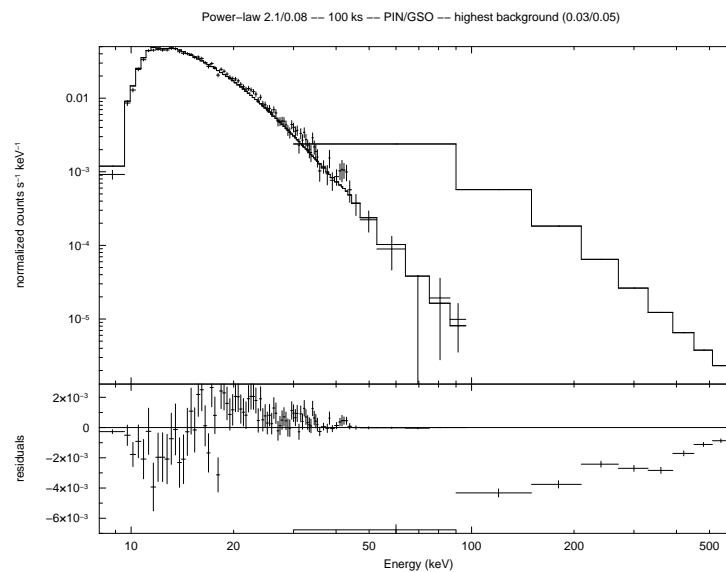
Figure 4.2: Simulation with the highest possible background for both PIN and GSO.

Finally, we check the source signal using low backgrounds.

```
XSPEC12>cornorm 1 2 -0.03 -0.05
 Spectrum 1 correction norm set to -0.03
 Spectrum 2 correction norm set to -0.03
 Spectrum 2 correction norm set to -0.05
```

```
 Chi-Squared =           2554.67 using 519 PHA bins.
 Reduced chi-squared =         4.94133 for     517 degrees of freedom
 Null hypothesis probability =  4.818636e-266
 Valid fit does not exist.
XSPEC12>fit
 renorm: no renormalization necessary

Chi-Squared  Lvl Par #           1               2
2348.3         -2    2.15864        0.0898853
2082.36        -2    2.04224        0.0695179
2029.76        -2    1.97611        0.0585291
2022.53        -3    1.88443        0.0441994
1990.53        -4    1.85165        0.0416839
1990.32        -5    1.84426        0.0408499
1990.3         -6    1.84234        0.0406345
1990.3         -7    1.84183        0.0405767
=============================
 Variances and Principal Axes
                 1         2
 3.57E-04 |   -0.99      -0.11
 6.89E-08 |    0.11      -0.99
-----------------------------


========================
  Covariance Matrix
   1           2
3.527e-04   4.077e-05
4.077e-05   4.783e-06
------------------------


===========================================================================
Model powerlaw<1> Source No.: 1   Active/On
Model Model Component  Parameter  Unit      Value
 par  comp
   1    1   powerlaw   PhoIndex                1.84183      +/-  1.87814E-02
   2    1   powerlaw   norm                    4.05767E-02  +/-  2.18699E-03
---------------------------------------------------------------------------


 Chi-Squared =          1990.30 using 519 PHA bins.
 Reduced chi-squared =         3.84971 for     517 degrees of freedom
 Null hypothesis probability =  2.232519e-171
```

```
XSPEC12>plot ldata res
```

The result in the plot shown in 4.3 where now the GSO spectrum is largely above background. By comparing the different fit results from these different runs, the total
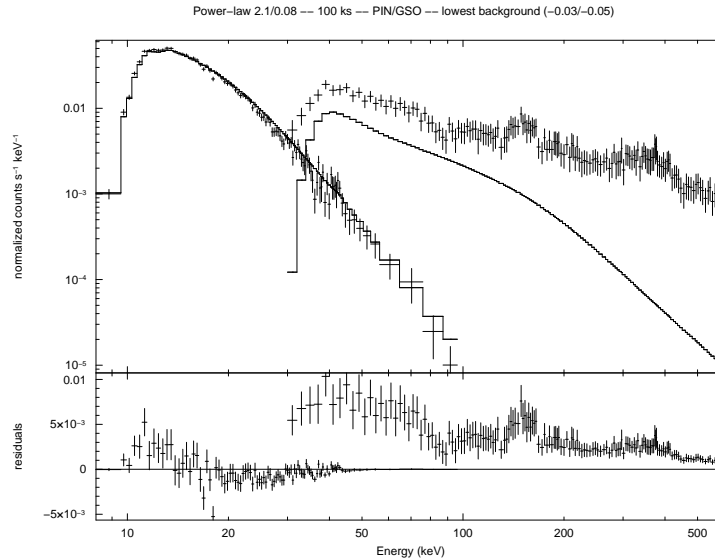
Figure 4.3: Simulation with the lowest possible background for both PIN and GSO.

expected error in the slope and normalization can be estimated.

4.6 XISSIM

xissim is a *Suzaku* XIS event simulator, based on the tool xrssim. It reads a FITS format photon list file, traces photon paths in the telescope (via ray-tracing), and outputs a simulated XIS event file. XRT thermal shield transmission and XIS detection efficiency are taken into account if requested. Each record of the photon list file describes the celestial positions, arrival time, and energy of the input photon. The mkphlist ftool can create such photon list files from FITS images (e.g., ROSAT HRI or *Chandra* images) and spectral models (which may be created in XSPEC). The xissim output event file may be analyzed just like a real data, using standard analysis tools such as xselect.

xissim has been released through the latest version of FTOOLS

4.7   Using MAKI

MAKI is another Web-based interactive tool (see Appendix C) that can determine the orientation of the XIS CCDs on the sky as a function of the observation epoch within the visibility window of the target. For *Suzaku*, the orientation of the solar panels with respect to the spacecraft is fixed, and at the same time, the range of the angles between the vector normal to the solar panels and the vector pointing to the Sun is restricted, which in turn restricts the roll angle of the spacecraft.

When using the tool, general instructions are available via the "Help" button. section. To check the visibility and available roll angles for a target, first load an image. This can be done with either an existing FITS image, or by entering the RA and Declination of the source and clicking the "New Graph" button. This creates an image upon which the *Suzaku* XIS field of view (FOV) will be shown.

The "Mission and Roll Selector" (in the upper right of the display) allows different instruments from different missions to be selected. Then the FOV will appear on your image. This can be rotated using the "Roll angle" slider bar.

4.8   Guide to Using the RPS

RPS, or the Remote Proposal Submission tool, must be used to enter the basic proposal data into the ISAS/JAXA, HEASARC, or ESA database. Proposers should make sure they use the appropriate RPS, since they are multiple reviews. See Appendix C for the list of RPS websites and addresses. Two versions of RPS are available: a character-oriented version, where the user submits all the required information via e-mail, or a Web-oriented version.

One aspect of RPS that is not immediately obvious is how to specify the time-constrained observations. For instance, a need for such an observation may arise for a study of a spectrum of a binary system in a particular orbital phase. If some particular aspect of the observation cannot be clearly specified in the RPS form, the user should detail it in the "comments" field of the RPS form and/or contact either the *Suzaku* team at ISAS/JAXA or the NASA *Suzaku* GOF before submitting.

4.9   Checklist

A successful *Suzaku* proposal, from a technical point of view, must include the following elements:

Coordinates: The PI is responsible for supplying the correct J2000 coordinates. For extended sources, specify single FOVs (coordinates for the center of XIS or the HXD)

or rastering parameters (a schematic drawing overlaid on images would be the least ambiguous; equivalent textual descriptions are acceptable).

XIS Count rate and exposure time: Explain how they were calculated (for a highly variable source, added explanation — such as "excluding any bursts" — would be helpful).

HXD Count rate and exposure time: If the source is not expected to be a hard X–ray source, this can be set to 0.0 since only the source counts are to be included.

Aimpoint – XIS or HXD : The HXD and XIS aimpoints differ by $3.5'$. To get the full effective area for a given instrument, the instrument-specific aimpoint must be chosen (the HXD aimpoint is at (DETX,DETY)=(-3.5$'$, 0) on the XIS image). The reduction in effective area for the non-selected instrument is $\sim 10\%$.

Performing Charge Injection – Yes or No: The current recommendation is to apply "the charge injection" (CI) option. The simulation tools and response files provided for AO-2 proposers assume CI, with a better spectral resolution compared to the non-CI case. However, the CI option may not be usable with some combinations of the window and burst options. Compatible combinations of the options are found in the Suzaku web page. Proposers requesting observations of bright sources that require window and burst options should consider the consequences, should CI be unavailable for the observation mode, and watch out for possible updates from the XIS team.

Observing constraints, if any: These include monitoring, coordinated, phase-dependent, and roll-dependent; TOOs are allowed, but the triggering criteria and the probability of triggering must be spelled out in text, and summarized in target remarks.

Note that the GOs are welcome to propose for targets already approved for the SWG or AO1 time (see the Announcement of Opportunity). However, in the interest of maximizing the scientific return from *Suzaku*, the proposal must explain why the already-approved observation does not meet their scientific objectives. Valid reasons include a much longer exposure time; incompatible time constraints; different positions within an extended source.

We note also that the XISs are also subject to count rate limitations, because of possible multiple events in an XIS pixel within one frame (see § 6.9.1). This is much less of a problem than with the ACIS aboard *Chandra*, as *Chandra*'s mirror focuses the X–ray flux into a region of a CCD that is orders of magnitude smaller. The rule of thumb is that the XIS can tolerate a point source with a count rate up to ~ 40 cts s^{-1} per CCD with essentially no loss of counts or resolution. For brighter sources, these limitations can be reduced via a variety of XIS modes, such as the use of a sub-array of the XIS, as discussed in § 6.5.

Finally, it is important to remember that because HXD is a non-imaging detector, contaminating sources in the field of view can significantly affect your results. The HXD

field of view is defined by a collimator with a square opening. The FWHM of the field of view is $34.4' \times 34.4'$ below ~ 100 keV and $4.6^{\text{o}} \times 4.6^{\text{o}}$ above ~ 100 keV. Considering that twice the FWHM value is required to completely eliminate the contamination in a collimator-type detector, and the source may happen to be located at the diagonal of the square, nearby bright sources within a radius of $50'$ and 6.5^{o} from the aim point can contaminate the data in the energy band below and above ~ 100 keV, respectively. If you specify the roll-angle to avoid the source, the limit will be reduced to $\sim 35'$ and $\sim 4.6^{\text{o}}$, respectively. It is the proposer's responsibility to show that any source with a flux level comparable to or brighter than that of your interest does not exist within these ranges. The proposer can check this in the minimum level by using the hard X-ray source catalogs from such satellites as RXTE-ASM, INTEGRAL, and Swift amongst others.

4.10   Additional Requirements for US Proposers

There are three additional NASA-specific proposal rules that must be followed by US-based proposers:

1. Proposals to NASA must be submitted through AKBAR/RPS. The user interface of AKBAR/RPS is similar to that of "classic" RPS except that the PI must first create an AKBAR account and/or join the Suzaku RPS group. Having done so, the Suzaku RPS form can be accessed via AKBAR/RPS.

2. The estimated level of effort (in FTEs) of any NASA civil servants among the team (PI or co-Is) must be entered into the AKBAR/RPS form. Enter 0 if no NASA civil servant is part of the team.

3. As described in the NRA, the NASA Office of Space Science **requires** all proposals to demonstrate their relationship to NASA Goals and Research Focus Areas (RFAs). Therefore, each proposal should include a sentence stating its specific relevence to one of the RFAs given in Table 1 of the Summary of Solicitation. In particular, *Suzaku* science will often address the science themes in the "Astronomical Search for Origins" and the "Structure and Evolution of the Universe."

Chapter 5

X–Ray Telescopes (XRTs)

Suzaku has five light-weight thin-foil X–Ray Telescopes (XRTs). The XRTs have been developed jointly by NASA/GSFC, Nagoya University, Tokyo Metropolitan University, and ISAS/JAXA. These are grazing-incidence reflective optics consisting of compactly nested, thin conical elements. Because of the reflectors' small thickness, they permit high density nesting and thus provide large collecting efficiency with a moderate imaging capability in the energy range of 0.2–12 keV, all accomplished in telescope units under 20 kg each.

Four XRTs onboard *Suzaku* (XRT-I) are used on the XIS, and the other XRT (XRT-S) is for the XRS. XRT-S is no longer functional. The XRTs are arranged on the Extensible Optical Bench (EOB) on the spacecraft in the manner shown in Figure 5.1. The external dimensions of the 4 XRT-Is are the same (See Table 5.1, which also includes a comparison with the ASCA telescopes).

The angular resolutions of the XRTs range from $1.8'$ to $2.3'$, expressed in terms of half-power diameter, which is the diameter within which half of the focused X–ray is enclosed. The angular resolution does not significantly depend on the energy of the incident X–ray in the energy range of *Suzaku*, 0.2-12 keV. The effective areas are typically 440 cm^2 at 1.5 keV and 250 cm^2 at 8 keV. The focal lengths are 4.75 m for the XRT-I. Actual focal lengths of the individual XRT quadrants deviate from the design values by a few cm. The optical axes of the quadrants of each XRT are aligned within $2'$ from the mechanical axis. The field of view for XRT-Is is about $17'$ at 1.5 keV and $13'$ at 8 keV. (see also Table 2.1)

5.1   Basic Components of XRT

The *Suzaku* X–Ray Telescopes (XRTs) consist of closely nested thin-foil reflectors, reflecting X–ray at small grazing angles. An XRT is a cylindrical structure, having the following layered components: 1. a thermal shield at the entrance aperture to help maintain a uniform temperature; 2. a pre-collimator mounted on metal rings for stray light elimination;
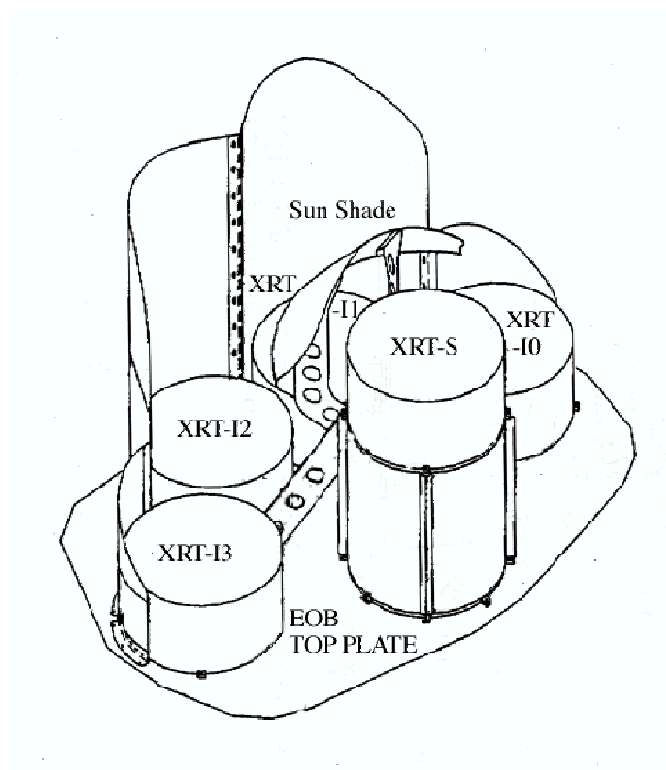
Figure 5.1: Layout of the XRTs on the *Suzaku* spacecraft.

	Suzaku XRT-I	ASCA
Number of telescopes	4	4
Focal length	4.75 m	3.5 m
Inner Diameter	118 mm	120 mm
Outer Diameter	399 mm	345 mm
Height	279 mm	220 mm
Mass/Telescope	19.5 kg	9.8 kg
Number of nested shells	175	120
Reflectors/Telescope	1400	960
Geometric area/Telescope	873 cm^2	558 cm^2
Reflecting surface	Gold	Gold
Substrate material	Aluminum	Aluminum
Substrate thickness	155 μm	127 μm
Reflector slant height	101.6 mm	101.6 mm

Table 5.1: Telescope Dimensions and Parameters of XRT-I

Figure 5.2: A Suzaku X–Ray Telescope

3. a primary stage for the first X–ray reflection; 4. a secondary stage for the second X–ray reflection; 5. a base ring for structural integrity and interface with the EOB of the spacecraft. All these components, except the base rings, are constructed in 90° segments. Four of these quadrants are coupled together by interconnect-couplers and also by the top and base rings (Figure 5.2). The telescope housings are made of aluminum for an optimal strength to mass ratio. Each reflector consists of a substrate also made of aluminum and an epoxy layer that couples the reflecting gold surface to the substrate.

Including the alignment bars, collimating pieces, screws and washers, couplers, retaining plates, housing panels and rings, each XRT-I consists of over 4112 mechanically separated parts. In total, nearly 7000 qualified reflectors were used and over 1 million cm^2 of gold surface was coated.

5.1.1 Reflectors

In shape, each reflector is a 90° segment of a section of a cone. The cone angle is designed to be the angle of on-axis incidence for the primary stage and 3 times that for the secondary

stage. They are 101.6 mm in slant length and with radii extending approximately from 60 mm at the inner part to 200 mm at the outer part. The reflectors are nominally 178 μm in thickness. All reflectors are positioned with grooved alignment bars, which hold the foils at their circular edges. There are 13 alignment bars at each face of each quadrant, separated at approximately 6.4° apart.

To properly reflect and focus X–ray at grazing incidence, the precision of the reflector figure and the smoothness of the reflector surface are important aspects. Since polishing of thin reflectors is both impractical and expensive, reflectors in *Suzaku* XRTs acquire their surface smoothness by a replication technique and their shape by thermo-forming of aluminum. In the replication method, metallic gold is deposited on extrusion glass mandrel ("replication mandrel"), of which the surface has sub-nanometer smoothness over a wide spatial frequency, and the substrate is subsequently bonded with the metallic film with a layer of epoxy. After the epoxy is hardened, the substrate-epoxy-gold film composite can be removed from the glass mandrel and the replica acquires the smoothness of the glass. The replica typically has ∼0.5 nm rms roughness in the mm or smaller spatial scale, which is sufficient for excellent reflectivity at incident angle less than the critical angle. The *Suzaku* XRTs are designed with on-axis reflection at less than critical angle, which is approximately inversely proportional to X–ray energy.

In the thermo-forming of the substrate, pre-cut, mechanically rolled aluminum foils are pressed onto a precisely shaped "forming mandrel", which is not the same as the replication mandrel. The combination is then heated until the aluminum softened. The aluminum foils acquire the figure of the properly shaped mandrel after cooling and release of pressure. In the *Suzaku* XRTs, the conical approximation of the Wolter-I type geometry is used. This approximation fundamentally limits the angular resolution achievable. More significantly, the combination of the figure error in the replication mandrels and the imperfection in the thermo-forming process (to about 4 micrometers in the low frequency components of the figure error in the axial direction) limits the angular resolution to about 1 minute of arc.

5.1.2   Pre-collimator

The pre-collimator, which blocks off stray light that otherwise would enter the detector at a larger angle than intended, consists of concentrically nested aluminum foils similar to that of the reflector substrates. They are shorter, 22 mm in length, and thinner, 120 micrometers in thickness. They are positioned in a fashion similar to that of the reflectors, by 13 grooved aluminum plates at each circular edge of the pieces. They are installed on top of their respective primary reflectors along the axial direction. Due to their smaller thickness, they do not significantly reduce the entrance aperture in that direction more than the reflectors already do. Pre-collimator foils do not have reflective surfaces (neither front nor back). The relevant dimensions are listed in Table 5.2.

	XRT-I
Number of Collimators	4
Height	32 mm
Blade Substrate	Aluminum
Blade Thickness	120 μm
Blade Height	22 mm
Height from Blade Top to Reflector Top	30 mm
Number of nested shells	175
Blade/Telescope	700
Mass/Collimator	2.7 kg

Table 5.2: Design Parameters for Pre-collimator
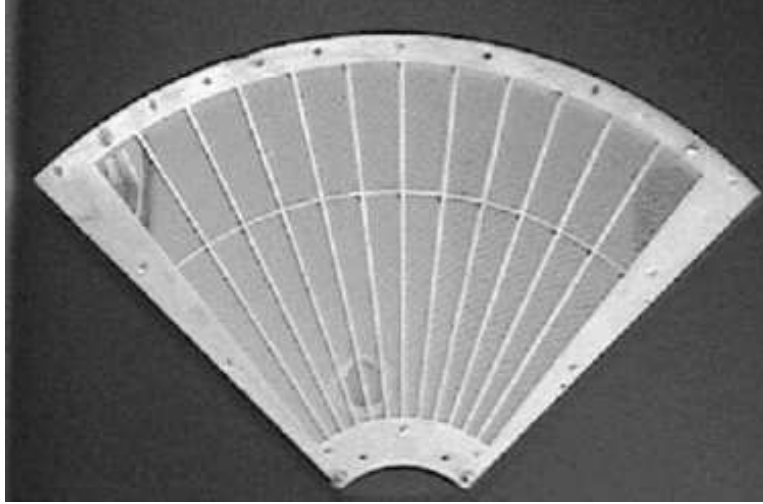
Figure 5.3: A thermal shield.

5.1.3 Thermal Shields

The *Suzaku* XRTs are designed to function in a thermal environment of 20±7.5°C. The reflectors, due to its composite nature and thus its mismatch in coefficients of thermal expansion, suffer from thermal distortion that degrades the angular resolution of the telescopes in temperature outside this range. Thermal gradient also distorts the telescope in a larger scale. Even though sun shields and other heating elements on the spacecraft help in maintaining a reasonable thermal environment, thermal shields are integrated on top of the pre-collimator stage to provide the needed thermal control.

5.2   In-flight Performance

In this section we describe in-flight performance and calibration of the Suzaku XRTs. There are no data to verify the in-flight performance of the XRT-S, therefore we hereafter concentrate on the four XRT-I modules (XRT-I0 through I3) which focus incident X-rays on the XIS detectors.

5.2.1   Focal Positions

A point-like source MCG−6−30-15 were observed at the XIS aimpoint during August 17-18. Figure 5.4 shows the focal position of the XRT-Is, that the source is focused when the satellite points at the XIS aimpoint. The focal positions are located roughly within $0'\!.5$ from the detector center with an deviation of $\sim 0'\!.3$. This implies that the fields of view of the XIS coincides each other within $\sim 0'\!.3$.
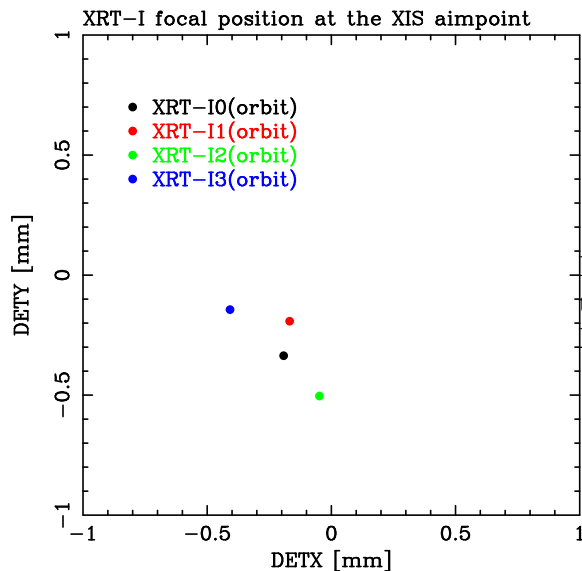
Figure 5.4: Focal positions at the XISs when the satellite points MCG−6−30-15 at the XIS aimpoint.

5.2.2   Optical Axis

The maximum transmission of each telescope module is achieved when a target star is observed along the optical axis. The optical axes of the four XRT-I modules are, however, expected to scatter in an angular range of $\sim 1'$. Accordingly, we have to define the axis to be used for real observations that gives reasonable compromise among the four optical axes. We hereafter refer to this axis as the observation axis.

In order to determine the observation axis, we have first searched for the optical axis of each XRT-I module by observing the Crab nebula at various off-axis angles. The observa-

tions of the Crab nebula were carried out in the following three groups of time. Hereafter all the off-axis angles are expressed in the detector coordinate system DETX/DETY (see `ftp://legacy.gsfc.nasa.gov/suzaku/doc/xis/suzakumemo-2006-39.pdf`).

1. 2005 Aug. 22 03:30UT – 15:33UT: a short observation near the center of the detectors, which is defined as the origin $(0', 0')$ of the DETX/DETY scheme, until 06:00UT followed by the four $10'$-off observations at $(\pm 10', 0')$ and $(0', \pm 10')$.

2. 2005 Aug. 24 23:58UT – Aug. 27 07:30UT: a series of the off-axis observations at $(\pm 3'.5, 0')$, $(0', \pm 3'.5)$, $(\pm 7'.0, 0')$, $(0', \pm 7'.0)$, $(\pm 20, 0')$, $(0', \pm 20')$, $(+50', 0')$ and $(+120', 0')$.

3. 2005 Sep. 15 01:00UT – Sep. 16 08:50UT: pointings at the XIS default position $(0', 0')$ and the HXD default position $(+3'.5, 0')$ as well as the remaining three $50'$ off pointings at $(-50', 0')$ and $(0', \pm 50')$.

Note that the field of view of the XIS detector is a square with $17'.8$ on a side. Thus only the data taken at the origin, at $\pm 3'.5$-off and at $\pm 7'.0$-off are available for determining the optical axes.

By fitting a model comprising of a Gaussian plus a constant to the data of counting rate as a function of the off-axis angle, we have determined the optical axis of each XRT-I module. The result is shown in Fig. 5.5. Since the optical axes moderately scatter around the origin, we have decided to adopt it as the observation axis for XIS-oriented observations as the default. Hereafter we refer to this axis as the XIS-default orientation, or equivalently, the XIS-default position. The optical axis of XRT-I0 shows the largest deviation of $\sim 1'.3$ from the XIS-default position. Nevertheless, the efficiency of XRT-I0 at the XIS-default position is more than 97% even in the highest 8–10 keV band (see Fig. 5.8). The optical axis of the HXD PIN detector, on the other hand, is deviated by $\sim 5'$ in the negative DETX direction (see for example, the instrument paper at `ftp://legacy.gsfc. nasa.gov/suzaku/doc/hxd/suzakumemo-2006-37.pdf`). Because of this, the observation efficiency of the HXD PIN at the XIS-default orientation is reduced to $\sim 93\%$ of the on-axis value. We thus provide the other default pointing position, the HXD-default position, for HXD-oriented observations, at $(-3'.5, 0')$ in the DETX/DETY coordinate. At the HXD-default position, the efficiency of the HXD PIN is nearly 100%, whereas that of the XIS is $\sim 88\%$ on the average.

5.2.3   Effective Area

In-flight calibration of the effective area has been carried out with the version 0.7 processed data (see `ftp://legacy.gsfc.nasa.gov/suzaku/doc/general/suzakumemo-2006-33.pdf`) of Crab nebula both at the XIS/HXD-default positions. The observations were carried out in 2005 September 15–16 (§3.1). The data were taken in the normal mode with the 0.1 s
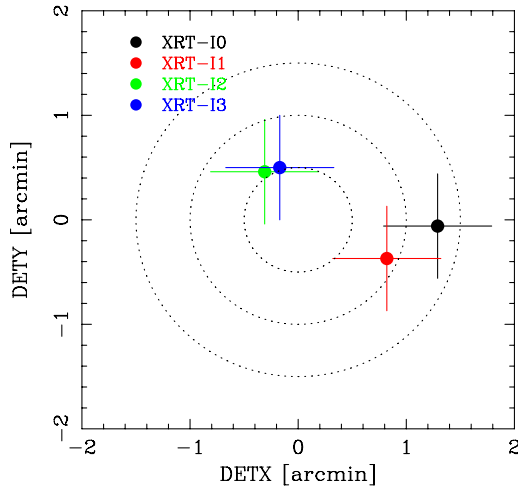
Figure 5.5: Locations of the optical axis of each XRT-I module in the focal plane determined from the observations of the Crab nebula in 2005 August–September. This figure implies that the image on each XIS detector becomes brightest when a target star is placed at the position of the corresponding cross. The dotted circles are drawn every $30''$ in radius from the XIS-default position (see text).

burst option in which the CCD is exposed during 0.1 s out of the full-frame read-out time of 8 s, in order to avoid the event pile-up and the telemetry saturation. The exposure time of 0.1 s is, however, comparable to the frame transfer time of 0.025 s. As a matter of fact, the Crab image is elongated in the frame-transfer direction due to so-called the out-of-time events, as shown in Fig. 5.6. Accordingly, the background-integration regions with a size of 126 by 1024 pixels are taken at the left and right ends of the chip for the XIS-default position, perpendicularly to the frame-transfer direction, as shown in the left panel of Fig. 5.6. For the observation at the HXD-default observation, the image center is shifted from the XIS-default position in the direction perpendicular to the frame-transfer direction for XIS0 and XIS3. Hence we can adopt the same background-integration regions as those of the XIS-default position for these two XIS modules. For XIS1 and XIS2, on the other hand, the image shift occurs in the frame-transfer direction, as shown in the right panel of Fig. 5.6. We thus take a single background-integration region with a size of 252 by 1024 pixels at the far side from the Crab image for the HXD-default position of these two detectors. As a result, the remaining source-integration region has a size of 768 by 1024 pixels, or $13'.3 \times 17'.8$ for all the cases, which is wide enough to collect all the photons from the Crab nebula.

After subtracting the background, taking into account the sizes of the regions, we have fitted the spectra taken with the four XIS modules with a model composed of a power law undergoing photoelectric absorption using XSPEC Version 11.2. For the photoelec-
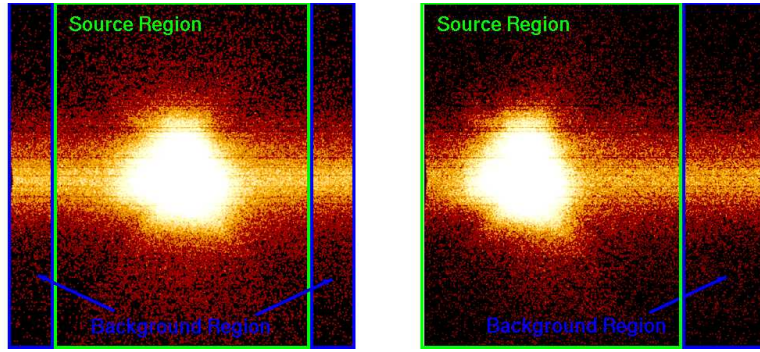
Figure 5.6: The source- and background-integration regions overlaid on the Crab images taken with XIS1 at the XIS-default position (left) and the HXD-default position (right) on 2005 September 15-16. The images are elongated in the frame-transfer direction due to the out-of-time events (see text). In order to cancel these events, the background regions with a size of 126 by 1024 pixels each are taken at the left and right ends of the chip for the XIS-default position, and a single region with a size of 252 by 1024 pixels is taken at the side far from the Crab image for the HXD-default position. The remaining source-integration region has a size of 768 by 1024 pixels, or $13'.3 \times 17'.8$. The background subtraction is carried out after after area-size correction.

tric absorption, we have adopted the model `phabs` with the cosmic metal composition (Anders & Grevesse 1989, Geochim. Cosmochim. Acta, 53, 197) First of all, we set all the parameters free to vary independently for all the XIS modules. The results are summarized for the XIS/HXD nominal positions separately in table 5.3, and are shown in Fig. 5.7. In doing the fit, we have adopted `ae_xi[12]_20060213.rmf` as the RMF, and `ae_xi[0123]_xisnom6_20060615.arf` or `ae_xi[0123]_hxdnom6_20060615.arf` as the ARF. These ARFs are made for a point source, whereas the Crab nebula is slightly extended ($\sim 2'$). We thus have created ARFs by utilizing the ray-tracing simulator (Misaki et al. 2005, Appl Opt, 44, 916) with a Chandra image as the input, and have confirmed that the difference of the effective area between these two sets of ARFs is less than 1%. We have neglected the energy channels below 1 keV, above 10 keV, and in the 1.5–2.0 keV band because of insufficient calibration related to uncertainties of the nature and the amount of the contaminant on the OBF and Si edge structure (see `ftp://legacy.gsfc.nasa.gov/suzaku/doc/xis/suzakumemo-2006-35.pdf`). Those energy channels are retrieved after the fit and shown in Fig. 5.7.

Toor & Seward (1974, AJ, 79, 995) compiled the results from a number of rocket and balloon measurements available at that time, and derived the photon index and the normalization of the power law of the Crab nebula to be 2.10 ± 0.03 and 9.7 photons cm^{-2} s^{-1} keV^{-1} at 1 keV, respectively. Overlaying photoelectric absorption with $N_H = 3 \times 10^{21}$ cm^{-2}, we obtain the flux to be 2.09×10^{-8} erg cm^{-2} s^{-1} in the 2–10 keV band.

Table 5.3: Best-fit parameters of the power law model to the Crab spectra taken in 2005 September 15-16.

Sensor ID	N_H	Photon Index	Normalization	Flux	χ^2_ν (d.o.f.)
XIS-default position					
XIS0	0.35±0.01	2.13±0.02	$10.48^{+0.27}_{-0.26}$	2.15	0.97 (199)
XIS1	0.30±0.01	2.07±0.02	9.52±0.23	2.14	1.27 (217)
XIS2	0.33±0.01	2.09±0.02	$10.09^{+0.26}_{-0.25}$	2.19	1.05 (200)
XIS3	0.34±0.02	2.07±0.02	$9.46^{+0.25}_{-0.24}$	2.13	1.11 (197)
HXD-default position					
XIS0	0.35±0.02	2.14±0.02	$9.79^{+0.31}_{-0.30}$	1.97	1.21 (155)
XIS1	0.29±0.02	2.09±0.02	$8.90^{+0.27}_{-0.26}$	1.94	1.07 (170)
XIS2	0.33±0.02	2.10±0.02	$9.89^{+0.28}_{-0.27}$	2.13	1.03 (181)
XIS3	0.32±0.02	2.06±0.02	$9.38^{+0.27}_{-0.26}$	2.15	1.19 (180)

N_H: Hydrogen column density in a unit of $10^{22} \mathrm{cm}^{-2}$.

Normalization: Power-law normalization in a unit of photons $\mathrm{cm}^{-2}\mathrm{s}^{-1}\mathrm{keV}^{-1}$ at 1 keV.

Photon index: Energy flux in a unit of $10^{-8}\mathrm{cm}^{-2}\mathrm{s}^{-1}$ in the 2-10keV band.
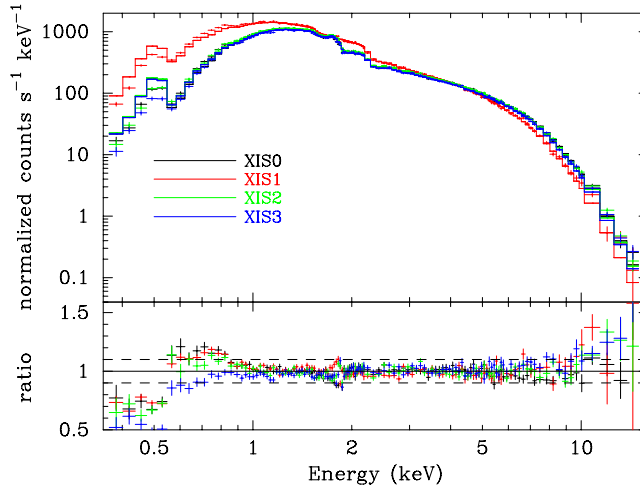
Figure 5.7: Power-law fit to the Crab spectra of all the four XIS modules taken at the XIS-default position. All the parameters are set free to vary independently for each XIS module. The fit is carried out in the 1.0-10.0keV band but excluding the interval 1.5-2.0 keV where a large systematic error associated with the Si K-edge remains, and the other channels are retrieved after the fit.

The best-fit parameters of all the XIS modules at the XIS-default position are close to these standard values. Although those at the HXD-default position show similar values,

the fluxes of XIS0 and XIS1 are smaller than the standard value by 6–7 %. Since the optical axes of these two detectors are farther away from the HXD-default position than those of the other two (Fig. 5.5), this may be due to insufficient calibration of the optical axes and/or the vignetting.

Since the best-fit parameters of the four XIS modules are close to the standard values, we have attempted to constrain the hydrogen column density and the photon index to be common among all the detectors. The best-fit parameters are summarized in table 5.4. The hydrogen column density $(0.32–0.33)\times10^{22}\mathrm{cm}^{-2}$ and the photon index 2.09 ± 0.01 are

Table 5.4: Best-fit parameters of the contemporaneous power-law fit to the Crab spectra taken in 2005 September 15-16.

Sensor ID	N_H	Photon Index	Normalization	Flux	χ^2_ν (d.o.f.)
		XIS-default position			
XIS0	0.33±0.01	2.09±0.01	9.93±0.13	2.17	1.22 (817)
XIS1	—	—	9.89±0.13	2.16	
XIS2	—	—	10.04±0.13	2.19	
XIS3	—	—	9.52±0.13	2.08	
average			9.845	2.15	
		HXD-default position			
XIS0	0.32±0.01	2.09±0.01	$9.22^{+0.15}_{-0.14}$	2.00	1.27 (692)
XIS1	—	—	9.09±0.14	1.98	
XIS2	—	—	9.77±0.15	2.13	
XIS3	—	—	9.65±0.15	2.10	
average			9.433	2.05	

N_H : Hydrogen column density in a unit of $10^{22}\mathrm{cm}^{-2}$.
Normalization : Power-law normalization in a unit of photons $\mathrm{cm}^{-2}\mathrm{s}^{-1}\mathrm{keV}^{-1}$ at 1 keV.
Flux : Energy flux in a unit of $10^{-8}\mathrm{cm}^{-2}\mathrm{s}^{-1}$ in the 2-10keV band.
— : Constrained to be the same as the corresponding parameter of XIS0.

consistent with the standard values.

5.2.4 Vignetting

The vignetting curves calculated by the ray-tracing simulator is compared with the observed intensities of the Crab nebula at various off-axis angles in Fig. 5.8. We have utilized the data of the Crab nebula taken during 2005 August 22–27 to search for the optical axis of each XRT. In the figure, we have drawn the vignetting curves in the two energy bands 3–6 keV and 8–10 keV. To obtain this, we first assume the spectral parameters of the Crab nebula to be a power law with $N_\mathrm{H} = 0.33 \times 10^{22}$ cm^{-2}, photon index = 2.09, and the normalization = 9.845 photons cm^{-2} s^{-1} keV^{-1} at 1 keV. These values are the averages of
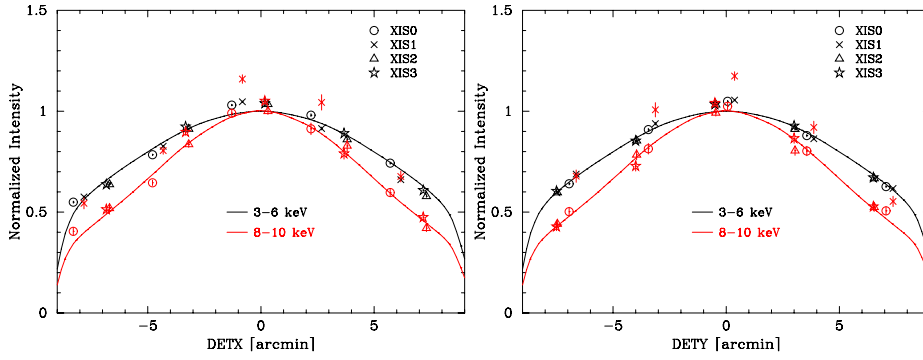
Figure 5.8: Vignetting of the four XRT-I modules using the data of the Crab nebula taken during 2005 August 22–27 in the two energy bands 3–6 keV and 8–10 keV. The model curves are calculated with the ray-tracing simulator with the spectral parameters of $N_H = 0.33 \times 10^{22}$ cm^{-2}, photon index $= 2.09$, and the normalization $= 9.845$ photons cm^{-2} s^{-1} keV^{-1} at 1 keV. Note that the abrupt drop of the model curves at $\sim 8'$ is due to the source approaching the detector edge. See the text for more detail. The excess of the data points of XIS1 is probably due to insufficient calibration of the backside-illuminated CCD.

the four detectors at the XIS-default position (table 5.4). We then calculate the counting rate of the Crab nebula on the entire CCD field of view in every $0'.5$ step both in the DETX and DETY directions using the ray-tracing simulator. Note that the abrupt drop of the model curves at $\sim 8'$ is due to the source approaching the detector edge. On the other hand, the data points provide the real counting rates in the corresponding energy bands within an aperture of $13'.3$ by $17'.8$. They consist of the observations at the five different off-axis angles $0'$, $\pm 3'.5$, and $\pm 7'.0$ both in DETX and DETY directions, where the origin is the XIS-default position. Note that the aperture adopted for the observed data can collect more than 99% of the photons from the Crab nebula, and hence the difference of the integration regions between the simulation and the observation does not matter. Finally, we renormalize both the simulation curve and the data so that the counting rate of the simulation curve at the origin becomes equal to unity.

These figures roughly show that the effective area is calibrated within $\sim 5\%$ over the XIS field of view, except for the 8–10 keV band of XIS1. The excess of the data point at the XIS-default position is already seen in Fig. 5.7. Although the reason for these excess is unclear, it is probably associated with insufficient calibration of the backside-illuminated CCD.

5.2.5   Angular Resolution and Aspect Error

Verification of the imaging capability of the XRTs has been made with the data of SS Cyg in quiescence taken during 2005 November 2 01:02UT–23:39UT. The total exposure time was 41.3 ks. SS Cyg is selected for this purpose because it is a point source and moderately bright (3.6, 5.9, 3.7, and 3.5 c s^{-1} for XIS0 through XIS3), and hence, it is needless to care about pile-up even at the image core.

In evaluating the imaging capability, it is found that variation of relative alignment between the XRT system and the Attitude and Orbit Controlling System (AOCS) becomes a significant problem. The variation is synchronized with the orbital motion of the spacecraft. This phenomenon is now understood to be due to the thermal distortion by the bright-earth illumination of the side panel #7 on which the instruments to measure the attitude of the spacecraft (the star trackers and the gyros) are mounted. The amplitude of the variation is as large as $\sim50''$ at most, which cannot be neglected in evaluating the imaging capability. A series of software to correct this alignment variation has been developed. In the meanwhile, we simply accumulate the data taken while the pointing of the XRT is stable. In Fig. 5.9, we show the image, the Point-Spread Function (PSF), and the EEF of all the XRT-I modules thus obtained. Due to this treatment, however, the total exposure time is reduced to be 9.1 ks. The HPD is obtained to be $1'.8$, $2'.3$, $2'.0$, and $2'.0$ for XRT-I0, 1, 2, and 3, respectively. These values are in general consistent with those expected from ground-based calibration measurements.

5.2.6   Stray Light

Observation of the stray light are carried out with the Crab nebula during 2005 August 22 – September 16 at the off-axis angles of $(\pm20', 0')$, $(0', \pm20')$, $(\pm50', 0')$, and $(0', \pm50')$ in (DETX, DETY). An example of the stray-light image is shown in the right panel of Fig. 5.10. This image is taken with XIS3 in the 2.5–5.5 keV band when the Crab nebula is offset at $(-20', 0')$ in (DETX, DETY). The left and central panels show simulated stray light images without and with the pre-collimator, respectively, of a monochromatic point source of 4.5 keV being located at the same off-axis angle. The ghost image seen in the left half of the field of view is due to the "secondary reflection". Although the "secondary reflection" cannot completely be diminished at the off-axis angle of $20'$, the center of the field of view is nearly free from the stray light. The semi-circular bright region in the middle panel, starting from (DETX, DETY) = $(-8'.9, +6'.5)$ through $\sim(0', 0')$ where the image becomes fainter, and ending up at $(-8'.9, -6'.5)$, originates from the innermost secondary reflector, because the space between the innermost reflector and the inner wall of the telescope housing is much larger than the reflector-reflector separation. This semi-circular bright region is marginally visible in the real Crab nebula image in the right panel. Another remarkable difference between the simulation and the real observation is the location of the brightest area; in the simulation, the left end of the image (DETX $\lesssim -7'.5$, $|$DETY$|\lesssim3'$)
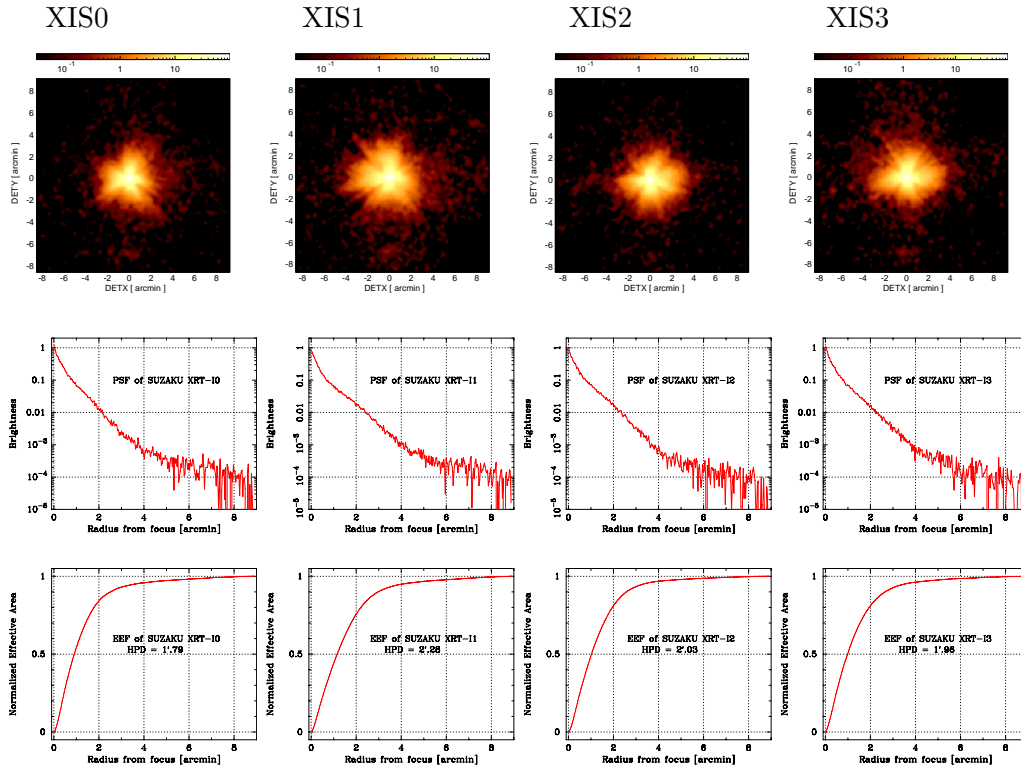
Figure 5.9: Image, Point-Spread Function (PSF), and EEF of the four XRT-I modules in the focal plane. All the images are binned with 2×2 pixels followed by being smoothed with a Gaussian with a sigma of 3 pixels, where the pixel size is 24 μm. The EEF is normalized to unity at the edge of the CCD chip (a square of $17'.8$ on a side). With this normalization, the HPD of the XRT-I0 through I3 is $1'.8$, $2'.3$, $2'.0$, and $2'.0$, respectively.

is relatively dark whereas the corresponding part is brightest in the Crab nebula image. These differences originate from relative alignments among the primary and secondary reflectors, and the blades of the pre-collimator, which are to be calibrated by referring to the data of the stray light observations in the near future.

In-flight stray-light observations were carried out with Crab at off-axis angles of $20'$ (4 pointings), $50'$ (4 pointing) and $120'$ (4 pointing) in August and September. We show an example of $20'$-off image of XRT-I3 together with simulation results of the same off-axis angle for the cases with and without the pre-collimator in Fig. 5.10. It is seen that the pre-collimator works for reducing the stray light in orbit.

Figure 5.11 shows angular responses of the XRT-I at 1.5 and 4.5 keV up to 2 degrees. The effective area is normalized at on-axis. The integration area is corresponding to the detector size of XIS ($17'.8 \times 17'.8$). The plots are necessary to plan observations of diffuse
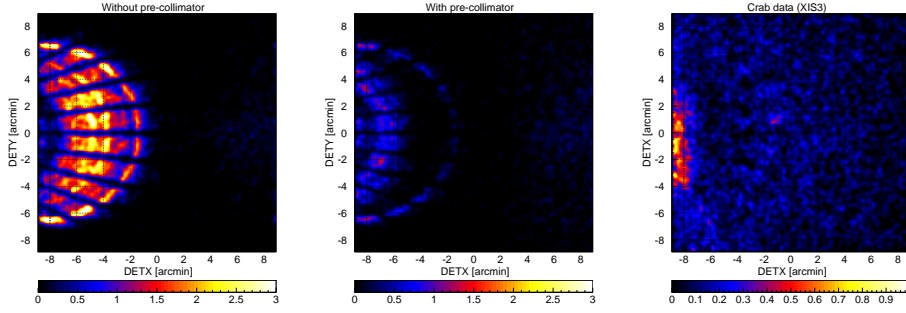
Figure 5.10: Focal plane images formed by stray lights. The left and middle panels show simulated images of a monochromatic point-like source of 4.51 keV locating at $(-20', 0')$ in (DETX, DETY) in the cases of without and with the pre-collimator, respectively. The radial dark lanes are the shades of the alignment bars. The right panel is the in-flight stray image of the Crab nebula in the 2.5–5.5 keV band located at the same off-axis angle. The unit of the color scale of this panel is counts per 16 pixels over the entire exposure time of 8428.8 s. The counting rate from the whole image is 0.78 ± 0.01 c s^{-1} including background. Note that the intensity of the Crab nebula measured with XIS3 at the XIS-default position is 458 ± 3 c s^{-1} in the same 2.5-5.5 keV band. All the images are binned with 2×2 pixels followed by being smoothed with a Gaussian with a sigma of 2 pixels, where the pixel size is 24 μm.
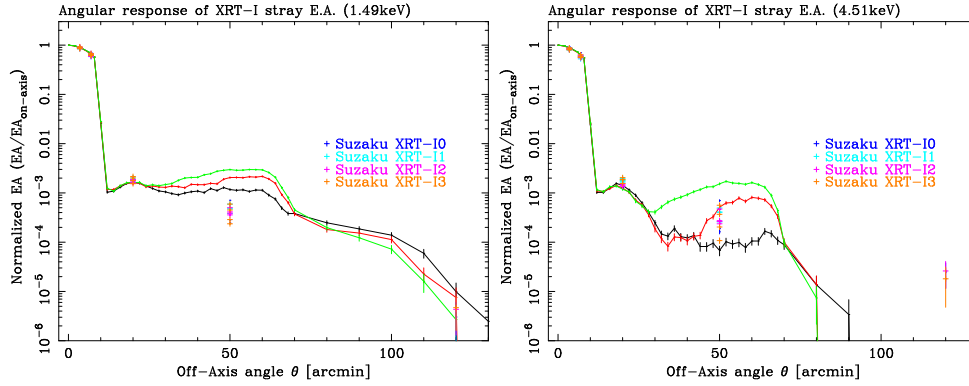
Figure 5.11: Angular responses of the XRT-I at 1.5 (left) and 4.5 keV (right) up to 2 degrees. The effective area is normalized at on-axis. The integration area is corresponding to the detector size of XIS ($17'.8 \times 17'.8$). The three solid lines in the plots correspond to different parameters of ray-tracing program while the crosses are the normalized effective area using the Crab pointings.

sources or faint emissions near bright sources, such as outskirts of cluster of galaxies, diffuse objects in the Galactic plane, SN 1987A, etc.

The three solid lines in the plots correspond to different parameters of ray-tracing program while the crosses are the normalized effective area using the Crab pointings. For example, the effective area of the stray lights at 1.5 keV is $\sim 10^{-3}$ at angles smaller than 70 arcmin off axis and $< 10^{-3}$ at angles larger than 70 arcmin off. The measured flux of stray lights are in good agreement with that of raytracing within an order. The solution of the black line is incorporated in the xissim for the AO2 simulation.

Chapter 6

X–ray Imaging Spectrometer (XIS)

6.1 Overview of the XIS

Suzaku has four X–ray Imaging Spectrometers (XISs), which are shown in Figure 6.1. These employ X–ray sensitive silicon charge-coupled devices (CCDs), which are operated in a photon-counting mode, similar to that used in the ASCA SIS, *Chandra* ACIS, and *XMM-Newton* EPIC. In general, X-ray CCDs operate by converting an incident X–ray photon into a charge cloud, with the magnitude of charge proportional to the energy of the absorbed X–ray. This charge is then shifted out onto the gate of an output transistor via an application of time-varying electrical potential. This results in a voltage level (often referred to as "pulse height") proportional to the energy of the X–ray photon.

The four *Suzaku* XISs are named XIS0, 1, 2 and 3, each located in the focal plane of an X–ray Telescope; those telescopes are known respectively as XRT-I0, XRT-I1, XRT-I2, and XRT-I3. Each CCD camera has a single CCD chip with an array of 1024×1024 picture elements ("pixels"), and covers an $18' \times 18'$ region on the sky. Each pixel is 24 μm square, and the size of the CCD is 25 mm $\times$ 25 mm. One of the XISs, XIS1, uses a back-side illuminated CCDs, while the other three use front-side illuminated CCDs. The XIS has been partially developed at MIT (CCD sensors, analog electronics, thermo-electric coolers, and temperature control electronics), while the digital electronics and a part of the sensor housing were developed in Japan, jointly by Kyoto University, Osaka University, Rikkyo University, Ehime University, and ISAS.

A CCD has a gate structure on one surface to transfer the charge packets to the readout gate. The surface of the chip with the gate structure is called the "front side". A front-side illuminated CCD (FI CCD) detects X-ray photons that pass through its gate structures, i.e. from the front side. Because of the additional photo-electric absorption at

50

Figure 6.1: The four XIS detectors before installation onto *Suzaku*.

the gate structure, the low-energy quantum detection efficiency (QDE) of the FI CCD is rather limited. Conversely, a back-side illuminated CCD (BI CCD) receives photons from "back," or the side without the gate structures. For this purpose, the undepleted layer of the CCD is completely removed in the BI CCD, and a thin layer to enhance the electron collection efficiency is added in the back surface. A BI CCD retains a high QDE even in sub-keV energy band because of the absence of gate structure on the photon-detection side. However, a BI CCD tends to have a slightly thinner depletion layer, and the QDE is therefore slightly lower in the high energy band. The decision to use only one BI CCD and three FI CCDs was made because of both the slight additional risk involved in the new technology BI CCDs and the need to balance the overall efficiency for both low and high energy photons.

Fig. 6.2 provides a schematic view of the XIS system. The Analog Electronics (AE) drives the CCD and processes its data. Charge clouds produced in the exposure area in the CCD are transferred to the Frame Store Area (FSA) after the exposure according to the clocks supplied by the AE. The AE reads out data stored in the FSA sequentially, amplifies the data, and performs the analog-to-digital conversion. The AE outputs the digital data into the memory in PPU named Pixel RAM. Subsequent data processing is
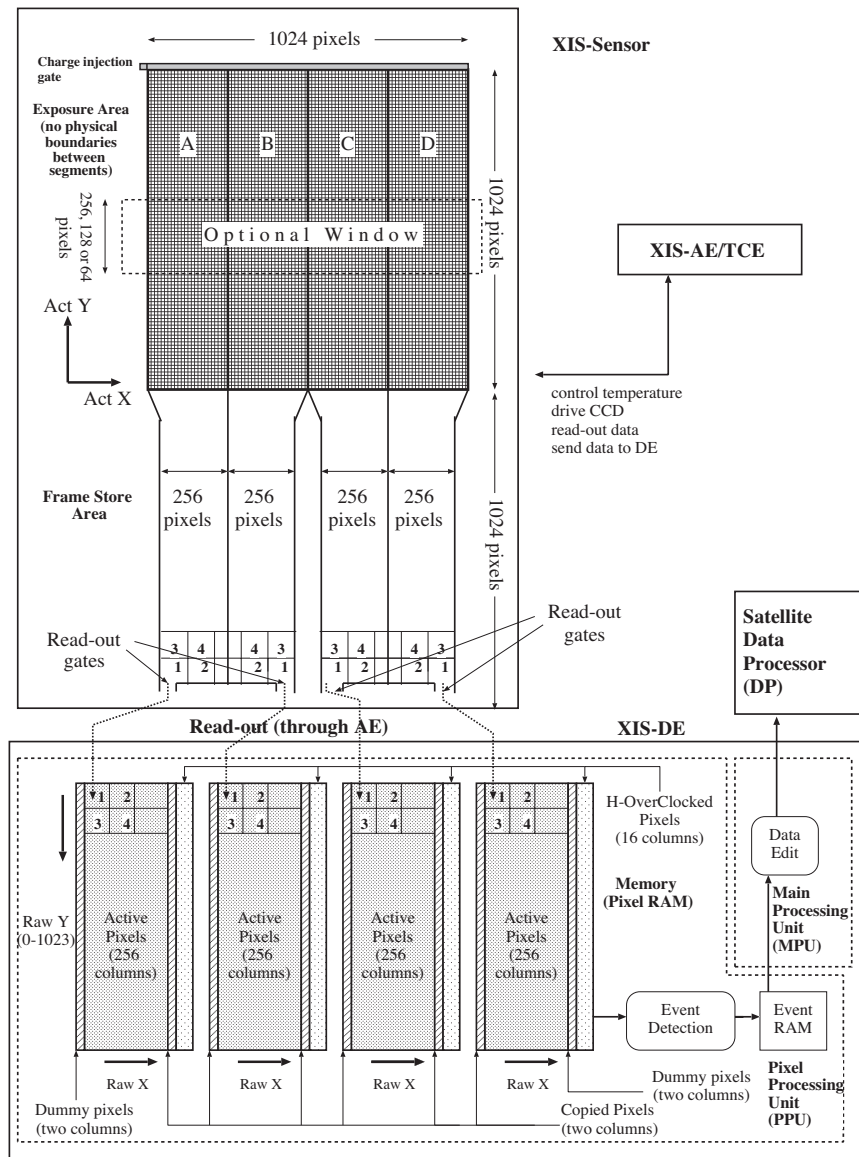
Figure 6.2: One XIS instrument. Each XIS consists of a single CCD chip with 1024×1024 X–ray sensitive cells, each 24 μm square. *Suzaku* contains four CCD sensors (XIS0 to 3), two AE/TCUs (AE/TCE01 and AE/TCE23), two PPUs (PPU01 and PPU23), and one MPU. AE/TCU01 and PPU01 service XIS0 and XIS1, while AE/TCE23 and PPU23 service XIS2 and XIS3. Three of the XIS CCDs are front-illuminated (FI) and one (XIS1) is back-illuminated (BI).

done by accessing the Pixel RAM. To minimize the thermal noise, the sensors need to

be kept at $\sim -90°$C during observations. This is accomplished by thermo-electric coolers (TECs), controlled by TEC Control Electronics, or TCE. The AE and TCE are located in the same housing, and together, they are called the AE/TCE. *Suzaku* has two AE/TCEs; AE/TCE01 is used for XIS0 and 1, and AE/TCE23 is used for XIS2 and 3. The digital electronics system for the XISs consists of two Pixel Processing Units (PPU) and one Main Processing Unit (MPU); PPU01 is associated with AE/TCE01, and PPU23 is associated with AE/TCE23. The PPUs accesses the raw CCD data in the Pixel RAM, carry out event detection, and send event data to the MPU. The MPU edits and packets the event data, and sends them to the satellite's main digital processor.

To reduce contamination of the X–ray signal by optical and UV light, each XIS has an Optical Blocking Filter (OBF) located in front of it. The OBF is made of polyimide with a thickness of 1000 Å, coated with a total of 1200 Å of aluminum (400 Å on one side and 800 Å on the other side). To facilitate the in-flight calibration of the XISs, each CCD sensor has two ^{55}Fe calibration sources [1]. These sources are located on the side wall of the housing and are collimated in order to illuminate two corners of the CCD. They can easily be seen in two corners of each CCD. A small number of these X–rays scatter onto the entire CCD.

After the launch of *Suzaku*, we have operated the four XISs successfully for more than a year. However, we had to adapt the XIS operation to the flight performance of the CCD, which included unforeseen phenomena. The XIS had unexpectedly large contamination on the OBF from some material in the satellite. This reduced the low-energy efficiency of XIS significantly. We monitor the contamination thickness by observing the calibration targets (eg. 1E0102–72, RXJ1856.5–3754) regularly. This effect is included in the response matrices. It is known that the CCD performance gradually degrade in space due to the radiation damage. This is because the charge traps are produced by cosmic-rays and are accumulated in the CCD. One of the unique features of XIS is the capability to inject small amount of charge to the pixels. Charge injection is quite useful to fill the charge traps periodically, and to make them almost harmless. The charge injection is adopted as a standard method in AO2 to cope with the increase of the radiation damage. Details of the contamination and the charge injection are explained later.

6.2 CCD Pixels and Coordinates

A single XIS CCD chip consists of four segments (marked A, B, C and D in Fig. 6.2) and correspondingly has four separate readout nodes. Pixel data collected in each segment are read out from the corresponding readout node and sent to the Pixel RAM. In the Pixel RAM, pixels are given RAWX and RAWY coordinates for each segment in the order of the readout, such that RAWX values are from 0 to 255 and RAWY values are from 0 to

---

[1]There is one more ^{55}Fe calibration source installed on the door. This source was used only in the initial operation before the door opened, and is no more available.

1023. These physical pixels are named *Active pixels*.

In the same segment, pixels closer to the read-out node are read-out faster and stored in the Pixel RAM faster. Hence, the order of the pixel read-out is the same for segments A and C, and for segments B and D, but different between these two segment pairs, because of the different locations of the readout nodes. In Fig. 6.2, numbers 1, 2, 3 and 4 marked on each segment and Pixel RAM indicate the order of the pixel read-out and the storage in the Pixel RAM.

In addition to the Active pixels, the Pixel RAM stores the *Copied pixels*, *Dummy pixels* and *H-Over-Clocked pixels* (cf. Fig. 6.2). At the borders between two segments, two columns of pixels are copied from each segment to the other. Thus these are named Copied pixels. On both sides of the outer segments, two columns of empty Dummy Pixels are attached. In addition, 16 columns of H-Over-Clocked pixels are attached to each segment.

Actual pixel locations on the chip are calculated from the RAW XY coordinates and the segment ID during ground processing. The coordinates describing the actual pixel location on the chip are named ACT X and ACT Y coordinates (cf. Fig. 6.2). It is important to note that the RAW XY to ACT XY conversion depends on the on-board data processing mode (cf. § 6.4).

6.3 Pulse Height Determination and Hot Pixel Rejection

When a CCD pixel absorbs an X–ray photon, the X–ray is converted to an electric charge, which in turn produces a voltage at the analog output of the CCD. This voltage ("pulse-height") is proportional to the energy of the incident X–ray. In order to determine the true pulse-height corresponding to the input X–ray energy, it is necessary to subtract the *Dark Levels* and correct possible *optical Light Leaks*.

Dark Levels are non-zero pixel pulse-heights caused by leakage currents in the CCD. In addition, optical and UV light might enter the sensor due to imperfect shielding ("light leak"), producing pulse heights that are not related to X–rays. Analysis of the ASCA SIS data, which utilized the X-ray CCD in photon-counting mode for the first time, showed that the Dark Levels were different for different pixels, and their average did not necessarily follow a gaussian. On the other hand, Light Leaks are considered to be rather uniform over the CCD.

For the *Suzaku* XIS, Dark Levels and Light Leaks are calculated separately in normal mode. Dark Levels are defined for each pixel; those are expected to be constant for a given observation. The PPU calculates the Dark Levels in the Dark Initial mode (one of the special diagnostic modes of the XIS); those are stored in the Dark Level RAM. The average Dark Level is determined for each pixel, and if the dark level is higher than the hot-pixel threshold, this pixel is labeled as a *hot pixel*. Dark Levels can be updated by

the Dark Update mode, and sent to the telemetry by the Dark Frame mode. Analysis of the ASCA data showed that Dark Levels tend to change mostly during the SAA passage of the satellite. Dark Update mode may be employed several times a day after the SAA passage.

Hot pixels are pixels which always output over threshold pulse-heights even without input signals. Hot pixels are not usable for observation, and their output has to be disregarded during scientific analysis. XIS detects hot pixels on-board by the Dark Initial/Update mode, and their positions are registered in the dark Level RAM. Thus, hot pixels can be recognized on-board, and they are excluded from the event detection processes. It is also possible to specify the hot pixels manually. There are, however, some pixels which output over threshold pulse-heights intermittently. Such pixels are called flickering pixels. It is difficult to identify and remove the flickering pixels on board; they are inevitably output to the telemetry and need to be removed during the ground processing. Flickering pixels sometimes cluster around specific columns, which makes it relatively easy to identify.

The Light Leaks are calculated on board with the pulse height data after the subtraction of the Dark Levels. A truncated average is calculated for 256×114 pixels (this size was 64×64 before January 18, 2006) in every exposure and its running average produces the Light Leak. In spite of the name of Light Leak, Light Leak does not represent in reality optical/UV light leak to the CCD. It mostly represents fluctuation of the CCD output correlated to the variations of the satellite bus voltage. XIS has little optical/UV light leak, which is negligible unless the bright earth comes close to the XIS field of view.

The Dark Levels and the Light Leaks are merged in the parallel-sum (P-Sum) mode, so Dark Update mode is not available in P-Sum mode. The Dark Levels, which are defined for each pixel as the case of the normal mode, are updated every exposure. It may be considered that the Light Leak is defined for each pixel in P-Sum mode.

6.4   On-board Event Analysis

The main purpose of the on-board processing of the CCD data is to reduce the total amount transmitted to ground. For this purpose, the PPU searches for a characteristic pattern of charge distribution (called an event) in the pre-processed (post- Dark Levels and Light Leaks subtraction) frame data. When an X–ray photon is absorbed in a pixel, the photoionized electrons can spread into at most four adjacent pixels. An event is recognized when a valid pulse-height (one between the Event Lower and Upper Thresholds) is found that exceeds the pulse-heights in the eight adjacent pixels (e.g. it is the peak value in the 3×3 pixel grid). In P-Sum mode, only the horizontally adjacent pixels are considered. The Copied and Dummy pixels ensure that the event search is enabled on the pixels at the edges of each segment. The RAW XY coordinates of the central pixel are considered the location of the event. Pulse-height data for the adjacent 5×5 square pixels (or in P-Sum

mode 3 horizontal pixels) are sent to the Event RAM as well as the pixel location.

The MPU reads the Event RAM and edits the data to the telemetry format. The amount of information sent to telemetry depends on the editing mode of the XIS. All the editing modes (in normal mode; see §6.5) are designed to send the pulse heights of at least 4 central pixels of an event to the telemetry, because the charge cloud produced by an X-ray photon can spread into at most 4 pixels. Information of the surrounding pixels may or may not output to the telemetry depending on the editing mode. The 5×5 mode outputs the most detailed information to the telemetry, i.e. all 25 pulse-heights from the 5×5 pixels containing the event. The size of the telemetry data per event is reduced by a factor of 2 in 3×3 mode, and another factor of 2 in 2×2 mode. Details of the pulse height information sent to the telemetry are described in the next section.

6.5 Data Processing Modes

There are two different kinds of on-board data processing modes. The *Clock modes* describe how the CCD clocks are driven, and determine the exposure time, exposure region, and time resolution. The Clock modes are determined by a kind of program ("micro-code") loaded to the AE. The *Editing modes* specify how detected events are edited, and determine the formats of the XIS data telemetry. Editing modes are determined by the digital electronics.

It is possible to select different mode combinations for the four XISs independently. However, we expect that most observations will use all four in Normal 5×5 or 3×3 Mode (without Burst or Window options). Other modes are useful for bright sources (when pile-up or telemetry limitations are a concern) or if a higher time resolution (<8 s) is required.

6.5.1 Clock Modes

There are two kinds of Clock Modes in XIS, i.e. Nomal and Parallel Sum Modes. Furthermore, two options (Window and Burst options) may be used in combination with the Normal Mode. However, see §6.5.3 for the restriction in the usage of the Parallel Sum Mode.

- **Normal Mode:** If neither *Window* nor *Burst* option (see below) is specified, the exposure time is 8 seconds, and all the pixels on the CCD are read out every 8 seconds. This can be combined with either of the 5×5, 3×3, and 2×2 Editing modes.

- **Parallel Sum Mode:** The pixel data from multiple rows are summed in the Y-direction on the CCD, and the sum is put in the Pixel RAM as a single row. The number of rows to add is commandable, but only 128-row summation is supported

Option	Effective area (nominal: 1024×1024 pixels)	Exposure time (in 8 s period)
None	1024×1024 pixels	8 s
Burst	1024×1024 pixels	$(8/2^n)$ s $\times$ 1 exposure
Window	256×1024 pixels	2 s $\times$ 4 exposures
	128×1024 pixels	1 s $\times$ 8 exposures
Burst & Window	256×1024 pixels	$(2/2^n)$ s $\times$ 4 exposure
	128×1024 pixels	$(1/2^n)$ s $\times$ 8 exposure

Note: n is an integer.

Table 6.1: Effective area and exposure time for different burst and window options

at present. Parallel Sum mode can be used only with the Timing Editing mode, and the Y coordinate is used to determine the event arrival time. As a result, no spatial resolution is available in the Y-direction. The time resolution of the Parallel Sum Mode is 8 s/1024 $\sim$ 7.8 ms.

6.5.2 Window and Burst Options

Table 6.1 indicates how the effective area and exposure time are modified by the Burst and Window options.

In the Normal Clock mode, the *Window* and *Burst* options can modify the effective area and exposure time, respectively. The two options are independent, and may be used simultaneously. These options cannot be used with the Parallel Sum Clock mode.

- **Burst Option:** All the pixels are read out every 8 seconds (if the Window option is not specified), but the exposure time can be reduced by a factor of 2^n ($n = 1, 2, 3, \ldots$) from the nominal 8 s. This option may be used to avoid photon pile-up when observing a bright source. However, a dead time is introduced in the exposure. If the exposure is t s, there is a $8 - t$ s dead-time every 8 s.

- **Window Option:** This option allows shorter exposure times by reading out more frequently only a portion of the CCD. Only the parts of the chip within the Y-direction range specified by the commandable Window is used for exposure (cf. Fig. 6.2). The Window width in the Y-direction is either 256, 128 pixels around the aim point. When the Window width is 256 pixels (1/4 Window), the exposure time becomes a quarter of that without the Window option (i.e. 2 s), and the Pixel RAM is filled with the data from four successive exposures. Similarly, when the Window width is 128 pixels (1/8 Window), the exposure time becomes 1/8 of that without the Window option respectively, and the Pixel RAM is filled with the data from 8 successive exposures.

We show in Fig. 6.3 the time sequence of exposure, frame-store transfer, CCD readout, and storage to the pixel RAM (in PPU) in normal mode with or without Burst/Window option. Note that, when 1/8 Window option is applied, significant fraction of the source photons may be lost due to the tail of the XRT point spread function. Furthermore, the fractional loss may be modulated by the attitude fluctuation of the satellite, which is synchronized with the orbital motion of the satellite.
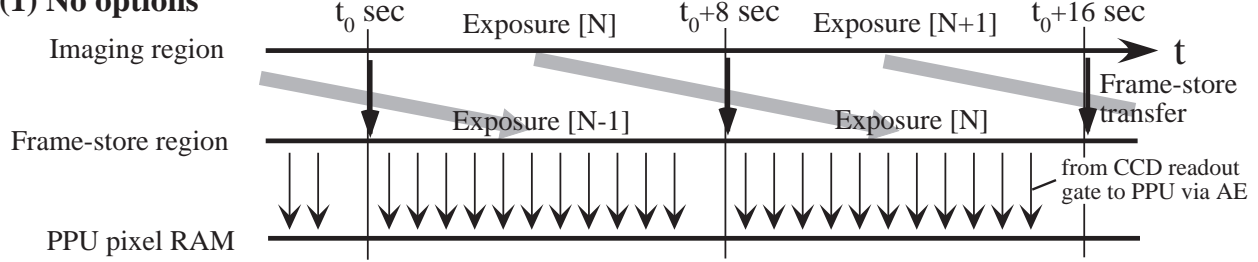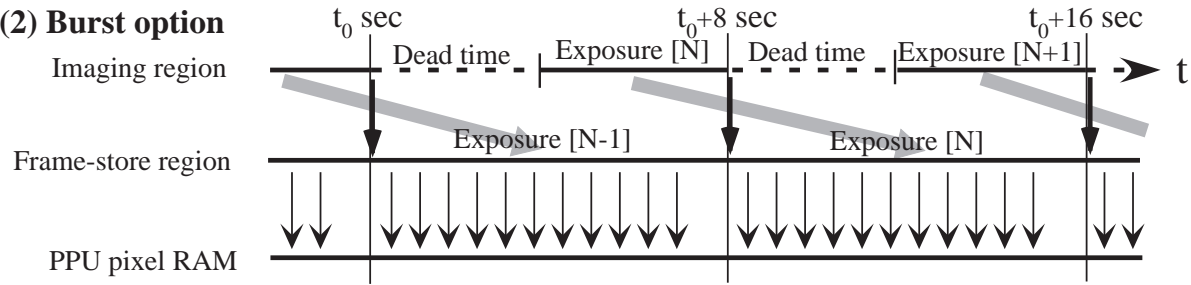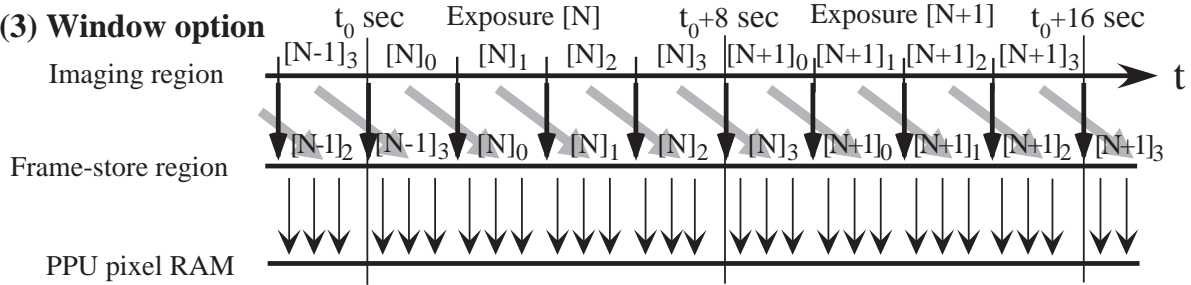
Figure 6.3: Time sequence of the exposure, frame-store transfer, CCD readout, and data transfer to the pixel RAM in PPU is shown (1) in normal mode without options, (2) in normal mode with Burst option, and (3) in normal mode with Window option. In this example, the 1/4 Window option is assumed.

6.5.3 Editing Modes

Editing modes may be divided into two categories, observation modes and diagnostics modes. We describe here mainly the observation modes. General users need not use the data in diagnostic modes. Among the observation modes, three modes (5×5, 3×3, and 2×2) are usable in normal modes, and only the timing mode in the P-Sum mode.

Observation Modes

- 5×5 **mode:** All the pulse heights of the 25 pixels centered at the event center are sent to the telemetry. This is used with the Normal Clock mode.

- 3×3 **mode:** Pulse heights of the 9 pixels centered at the event center are sent to the telemetry with the 1-bit information (pulse height larger than the Split Threshold Outer or not) for the surrounding 16 pixels. This is used with the Normal Clock mode.

- 2×2 **mode:** Pulse heights of the 2×2 square pixels are sent to the telemetry. The 2×2 pixels are selected to include the event center, second highest pixel in the cross centered at the event center, and the 3rd (or 4th) highest pixel in the cross. The 1-bit information (pulse height larger than the Split Threshold Outer or not) of the 8-attached pixels is also output to the telemetry. This is used with the Normal Clock mode.

- **Timing mode:** Total pulse height and the *Grades* of the event is output to the telemetry. Pulse heights of at most three pixels in the X-direction are summed to give the total pulse height if they are over the Inner Split Threshold. Position and number of pixels exceeding the threshold determines the *Grades*. This is used only with the P-Sum Clock mode. Window and Burst Options are not available in the Timing mode.

We show in Fig. 6.4 the pixel pattern whose pulse height or 1-bit information is sent to the telemetry. We do not assign grades to an event on board in the Normal Clock mode. This means that a dark frame error, if present, can be corrected accurately during the ground processing even in 2×2 mode. The definition of the grades in P-Sum mode is shown in Fig. 6.5.

There are slight differences between the 5×5, 3×3 and 2×2 modes. No significant difference is found so far between the 5×5 and 3×3 modes. However, 2×2 mode is slightly different from 3×3 or 5×5 mode. The difference is produced during the CTE correction in the ground processing. Because the pulse height information is limited in the 2×2 mode, some of the CTE corrections cannot be applied to the 2×2 mode data. This causes slight difference in the gain and quantum detection efficiency of 2×2 mode data. The XIS team may eventually need to prepare different calibration data for the 2×2 mode. However,

meanwhile, calibration accuracy of the 2×2 mode data is slightly worse than the 5×5 and 3×3 mode data. The 2×2 mode is employed only when a bright source is observed (see tables 6.7 and 6.8). Those who plan to observe a bright source should be aware of these systematics in 2×2 mode. The 2×2 mode is not used in BI CCD, because relatively large CTI in BI CCD produces significant calibration difference from 5×5 and 3×3 modes.

Note on the timing mode

In timing mode, data quality may be significantly degraded compared to the normal mode, while the calibration remains very preliminary stage. We do not expect that the calibration advances quickly in near future. Furthermore, there are some operational restrictions. From these reasons, the XIS team does not recommend to use the timing mode. Those who consider using the timing mode should use the mode at their own risk.

Timing mode is available only in the FI CCDs. There are relatively large numbers of hot/flickering pixels in BI CCD, which are difficult to remove completely on board. The remained hot/flickering pixels are found to fill the telemetry easily, because a single hot pixel can produce 1024 events in 8 s in the timing mode. Because of this telemetry occupation by the hot/flickering pixels, we cannot use the timing mode in BI CCD. Note that this does not happen in normal mode. The FI CCDs have only a small number of hot/flickering pixels. However, we found that we need to sometimes reset the Dark Level for its stable update (say, once per 96 min.). This means that we cannot take very long continuous data. This may not become a practical restriction, because the data acquisition becomes intermittent anyway due to the SAA passage and the earth occultation of the target.

Because only one dimensional information is available in timing mode, distinction between X-ray and non-X-ray events becomes inaccurate. This means that timing mode has significantly higher non-X-ray background than the normal mode. Although the actual background rate in timing mode is under investigation, it can be one or two orders of magnitude larger than the normal mode.

Flight calibration of the timing mode is very preliminary, and many of the performance is not calibrated yet. For example, it is not verified yet whether or not its full time resolution, 7.8 ms, can be really achieved on orbit. Energy calibrations, eg. gain and energy resolution, are known to change in the timing mode. Because the CTI correction in timing mode is not possible yet in the ground processing, timing mode has significantly different gain than the (CTI-corrected) normal mode. This also degrades the energy resolution. Effective area of the CCDs may also change in the timing mode. Even a small number of hot pixels produce a relatively large number of dead area in the CCD, which reduces the effective area. This reduction could be time dependent, because some of the hot pixels often disappear and reappear.

Diagnostic Modes

Besides the observation modes explained above, the XIS instrument has several diagnostic

5X5 mode 3X3 mode 2X2 mode

■ Center pixel of the event

▩ PH of the pixel is sent to the telemetry

▨ 1-bit information is sent to the telemetry
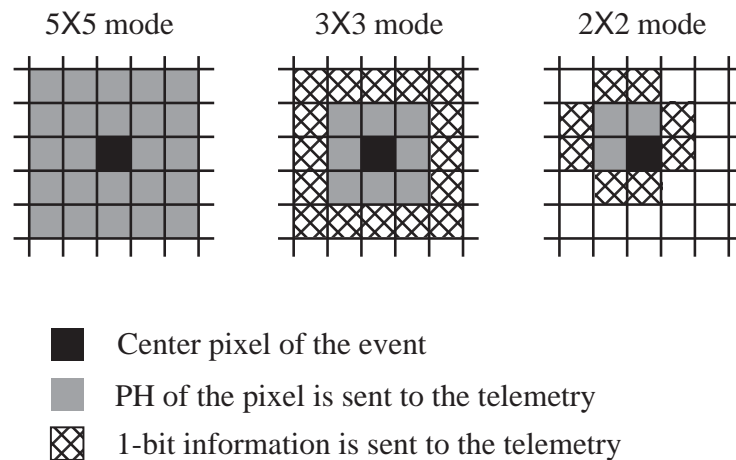
Figure 6.4: Information sent to the telemetry is shown for 5×5, 3×3, and 2×2 modes. 1-bit information means whether or not the PH of the pixel exceeds the outer split threshold. In 2×2 mode, the central 4 pixels are selected to include the second and the third (or fourth) highest pixels among the 5 pixels in a cross centered at the event center.

◄—— Serial transfer (RAWX ——►)

Grade 0: single Grade 1: leading split Grade 2: trailing split Grade 3: others

■ Center pixel of the event.

▦ Pulse height of the pixel is equal to or larger than the (inner) split threshold. This pulse height is added to the total pulse height.
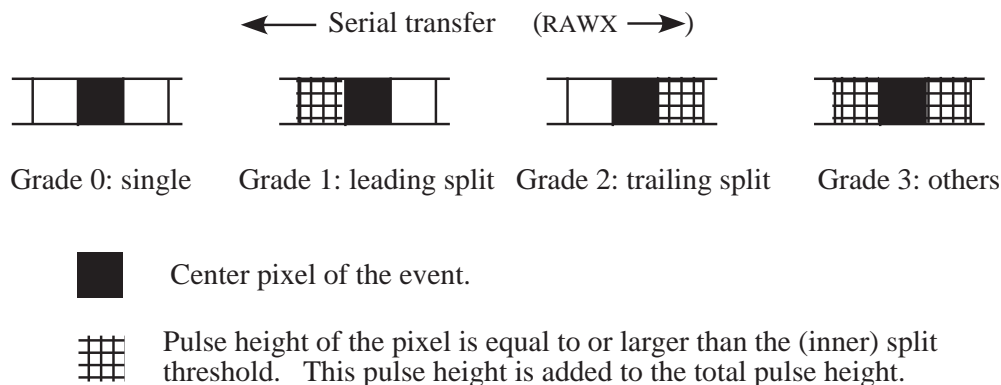
Figure 6.5: Definition of the grades in the P-Sum/timing mode. Total pulse height and the grade of the event are output to the telemetry. Note that the grades are defined referring to the direction of the serial transfer, so the central pixel of a grade 1 event has the *larger* RAWX value, while the opposite is true for a grade 2 event.

modes, Frame mode, Dark Initial mode, Dark Update mode, and Dark Frame mode. Frame mode simply dumps the raw CCD data to the telemetry. This mode may be useful for the health check of the CCD. Other modes are used primarily in determining/checking the dark levels. Dark Init mode is employed when the burst/window options are changed. Dark update mode is used just after the SAA passage to update the hot pixel list on board.

It is unlikely that those would be used by guest observers.

6.5.4 Discriminators

Three kinds of discriminators, area, grade and class discriminators, can be applied during the on-board processing. The grade discriminator is available only in the timing mode. The class discriminator was implemented after the launch of *Suzaku* and was used since January, 2006. In most cases, guest observers need not to change the default setting of these discriminators.

The class discriminator classifies the events into two classes, "X-rays" and "others," and output only the "X-ray" class to the telemetry when it is enabled. This class discriminator is always enabled to reduce the telemetry usage of non-X-ray events. The "other" class is close to, but slightly different from grade 7. When XIS points to blank sky, more than 90% of the detected events is particle events (mostly grade 7). If we reject these particle events on board, we can make a substantial saving in telemetry usage. This is especially useful when the data rate is medium or low. The class discriminator realizes such a function in a simple manner. When all the 8 pixels surrounding the event center exceeds the Inner Split Threshold, the event is classified as the "other" class, and the rest of the events as the "X-ray" class. With such a simple method, we can reject more than three quarters of the particle events. The class discriminator works only for 5x5 and 3x3 modes. It is not available in 2x2 and timing mode.

The area discriminator is used when we want to reject some (or most) of the frame data from the event extraction. The discriminator works on the Pixel RAM. When the discriminator is enabled, a part of the Pixel RAM is not used for the event extraction. This may be useful when a bright source is present in the XIS field of view other than the target source. If we set the discrimination area to include only the bright source, we can avoid outputting unnecessary events to the telemetry. Only a single, rectangular area can be specified in a segment for discrimination. Either inside or outside of the area can be rejected from the event extraction. The area discriminator works on the Pixel RAM, not for the physical area of the CCD. This is important when we apply the discriminator with the window option.

The Grade discriminator is used only in the timing mode. Any combination of the 4 grades can be selected to discriminate the grade for telemetry output.

Suzaku does not have the level discriminator, which was used in ASCA SIS. The same function can be realized, however, by changing the event threshold.

6.6   Spaced-row Charge Injection

Performance of CCD gradually degrades in the space environment due to the radiation damage by cosmic-ray particles. Spaced-row Charge Injection (CI) is used to restore the performance of CCD, especially in the charge transfer efficiency (CTE) and the energy resolution. The CI will be used in AO2 observations by default whenever it is possible. Description in this section is based on the data available as of Oct. 1, 2006. Since our knowledge and experience on the spaced-row CI are rapidly accumulating, the guest observers are recommended to visit the *Suzaku* web site for the latest information.

6.6.1   Principle of the Spaced-row Charge Injection

Performance of XIS is gradually degrading since the launch of *Suzaku* due to the radiation damage. Energy resolution at the time of writing (Sept. 2006) measured by the on-board calibration source of ^{55}Fe is about 200 eV (FWHM) at 5.9 keV, while it was ∼130–135 eV just after the launch.

In principle, a precision charge injection capability can mitigate the effects of in-flight radiation damage (Bautz et al. SPIE 2004, Vol. 5501, p111). A sufficient quantity of charge injected periodically during the array readout process (spaced-row CI) will tend to fill radiation-induced traps, and in so doing reduce the effects of these traps on the devices charge transfer efficiency (CTE). Because the traps need to be filled quite often, we inject charge every 54 rows in every exposure. The charge injected rows are not usable to detect X-ray photons, and become dead area.

This method was successfully implemented in the calibration observation of 1E0102–72 and the Perseus cluster done at the end of Aug. 2006, and the energy resolution was found to recover to approximately 150 eV at 6 keV. Although the spaced-row CI is effective to recover the energy resolution in the iron band, its effect is not investigated yet in low energy band especially below 1 keV as of Oct. 1, 2006. However, according to the analysis of the corner pixel distribution, which is a good measure of the excess noise after the Dark Level subtraction, no significant change is found in the distribution even with the CI. This means that the CI would not degrade the energy resolution even at very low energy. Further calibration of CI on the low-energy performance is in progress.

6.6.2   Applicable Modes

As of Oct. 1, 2006, spaced-row CI is applicable only for the normal mode. Application of CI in combination with the burst, window, window+burst options is under investigation now. However, we expect that the spaced-row CI may be available simultaneously with the burst and the window options. Latest information on the availability of the CI may be found in the *Suzaku* web page. Spaced-row CI is not applicable to the timing mode.
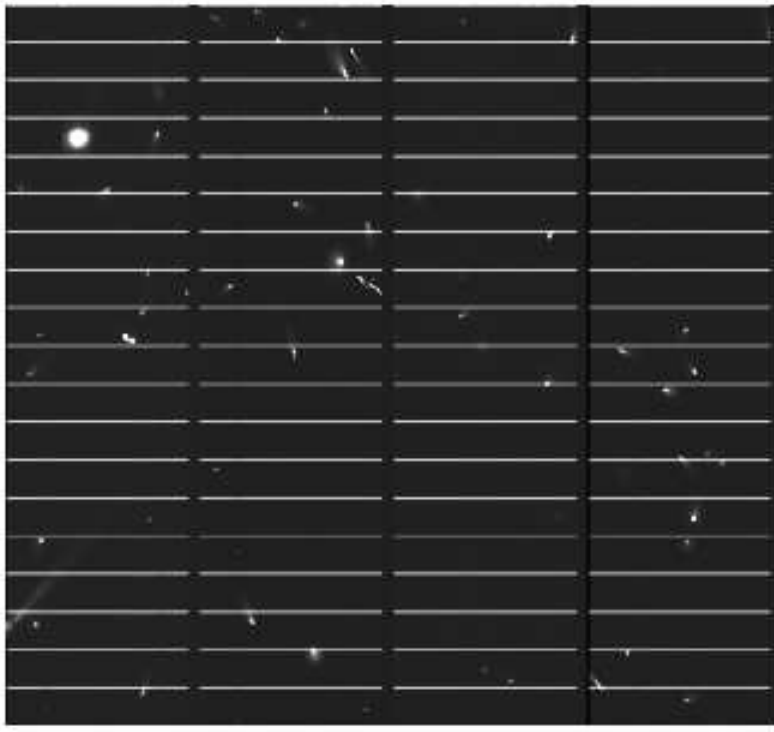
Figure 6.6: The frame mode data of XIS2 taken with spaced-row CI. The bright lines at every 54 row correspond to the charge injected lines. The lines are disconnected because the overclocked regions are also displayed at the segment boundaries.

6.6.3 Impacts on the Data

Here we summarize how the CI affects the data compared when no CI is used. There are several demerits associated with the CI. Guest observers should be aware of these characteristics of the CI data.

1. Energy resolution will improve from ∼200–220 eV (FWHM) to ∼140–150 eV at the iron band. Energy resolution may be improved also at lower energies, but the improvement is not verified yet at the time of writing.

2. Dead rows are produced every 54 row. The width of the dead line is 3 and 4 rows for the FI and BI sensor, respectively. The dead lines are fixed in RAWX, RAWY coordinate and are common to all the sensors. This means that the dead area will be 5.6% (for FI) and 7.4% (for BI) of the image. Because the width of the dead area is much smaller than the point-spread-function of the XRT and satellite attitude

fluctuates, we believe that these dead area would not hamper the image analysis.

3. Out-of-time events will increase. It takes about 25 ms to transfer the image area data to the frame-store area when no CI is implemented. This will increase to 156 ms when spaced-row CI is used. This means that the fraction of the out-of-time events increases from 0.3% to 2.0%.

4. Number of hot pixels slightly increase with the spaced-row CI. This may introduce slight increase of the dead area due to the hot pixels, but the increase is negligible compared to the dead area due to the injected charge itself.

5. Some of the analysis software might not be available even if the AO2 data are distributed to the guest observers. XIS team will try to finish the calibration of the CI data and to prepare the required analysis software by the start of AO2. However, it is difficult to predict at this stage when the team can finish preparing the analysis software. Please consult the *Suzaku* web site for the latest status of the analysis software.

6.7 Degradation of Low Energy Efficiency

The good low energy response is an important unique feature of the XIS. However, we noticed the effective area below 2 keV has been decreasing with time after the launch. The degradation is characterized by the additional absorption of carbon-dominated material. The thickness of this extra absorber is different for each sensor, but takes maximum at the center of the XIS CCD and decreases toward the edge of the field of view. Although the origin of the extra absorber has not yet been identified, we consider it is most likely some contaminant accumulating on the surface of the XIS optical blocking filters (OBF), which is one of the coldest parts inside the satellite.

In order to examine this efficiency degradation, we have observed soft and stable X-ray sources, such as, 1E0102–72, RXJ1856.5–3754, and the Cygnus loop, repeatedly. Atmospheric fluorescent lines of nitrogen and oxygen are also useful to evaluate the spatial dependence of the contaminant thickness over the CCD. Analysis of these data lead to our current knowledge of the extra absorber (or the contaminant on the OBF), as summarized below.

1. The extra absorber is made mainly of carbon. The absorber also contains oxygen, but its contribution is less than 1/5 of carbon in number.

2. Figure 6.7 shows the time evolution of the extra absorber thickness plotted as a function of time after the XIS door open. The evolution seems gradually slow down and is almost saturated 200–300 days after the XIS door open. The solid curves are the best-fit exponential functions to the data, whose time constants are 90–220 days.

Note that the absorber thickness in this plot is measured at the center of the FOV, where the absorber thickness is maximum.

3. Spatial distribution of the absorber thickness for XIS1 (BI-CCD) is shown in Figure 6.8 as a function of the distance from the FOV center. The extra absorber is thinner near the edge of the FOV. This radial profile and its time evolution is approximated with a simple analytic function (see Koyama et al., 2006).
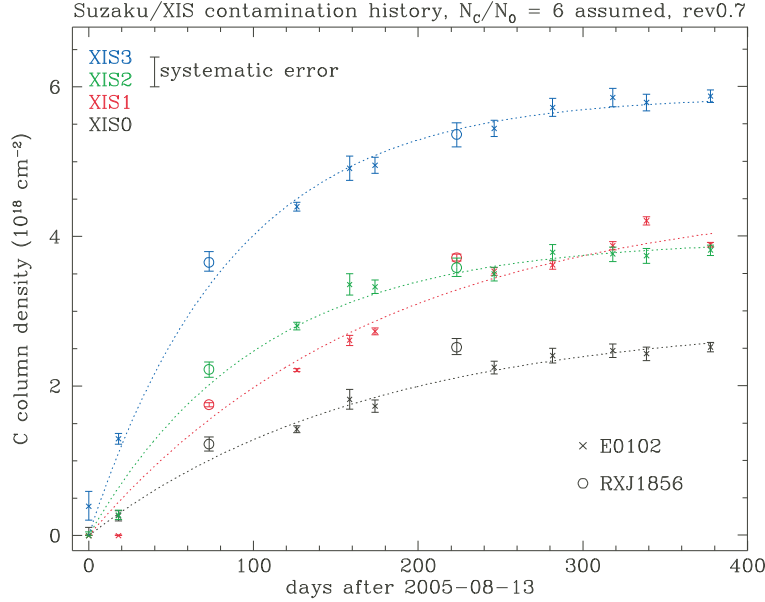
Figure 6.7: An empirical model for the on-axis contamination evolution, assuming DEHP (C24H38O4, or $C/O = 6$ by number) as contaminant. Crosses and open circles indicate the C column density of the contaminant derived from the E0102−72 and RXJ 1856 observations, respectively. Dotted lines indicate the best fit empirical model to the time evolution of the contamination for each sensor.

These results, the empirical models of the contamination thickness in particular, are implemented in *Suzaku* analysis software. The instrument team discourages the use of XSPEC models to describe this extra absorption (such as `xisabs`, `xiscoabs`, `xiscoabh`, `xispcoab`) but rather the use of a modified `.arf` file in which the absorption is taken into account.

Such an `.arf` file can be generated with the *Suzaku* ftool `xissimarfgen`. Detailed description is found in Ishisaki et al. and the *Suzaku* web site. For diffuse sources, one need to make arf with `xissimarfgen` considering the extension of the source. In this case, one should not include `xisabs`, `xiscoabs`, `xiscoabh`, `xispcoab` in the spectral fit.

Calibration of the efficiency degradation due to the extra-absorption is still under
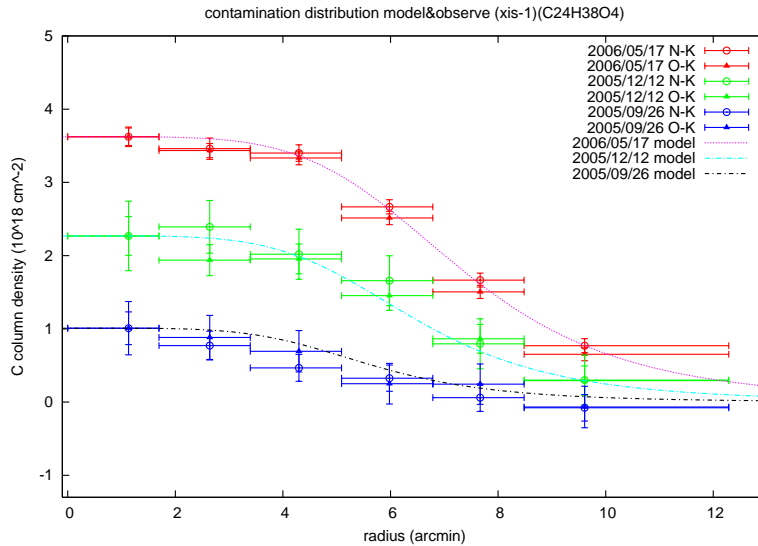
Figure 6.8: Time evolution of the radial profile of the contamination thickness derived from N and O fluorescent lines from the day earth (i.e. Sun lit Earth)) atmosphere. Each color indicates the profile at three epochs from just after "XIS door-open" to the recent AO1 observation. Open circles and filled triangles represent the data points determined by the N and O fluorescence lines, respectively. The best fit model is also shown in the figure. Note that, for the on-axis column densities, the results in Figure 6.7 are used.

progress. For example, relative contribution of oxygen to carbon has not yet been determined accurately. At present, we adopt the ratio of 1/6 in above models, but there are indications that the ratio is different for each sensor or changing in time. We also know, for some sources, the effective area decrease is evident above 2 keV (typically 5%), where our current absorption models with carbon and oxygen predicts little effects. We might need further study on this point. Furthermore, the radial profile of the extra absorber has been studied in detail only for XIS1 (BI-CCD), but not in detail for other sensors.

Future prospect of the efficiency degradation is difficult to predict. However, extrapolation of the current evolution curves (Figure 6.7) will be appropriate for the proposals. For the AO-2 proposers we are going to provide the arf in which efficiency degradation expected on 2007 August is taken into account. These arf's will be generated with `xissimarfgen`. The arf's for diffuse sources should be generated with `xissimarfgen` by proposers.

6.8   Non-X-ray background

All four XISs have low backgrounds, due to a combination of the *Suzaku* orbit and the instrumental design. The large effective area at Fe K (comparable to the *XMM-Newton* PN) combined with this low background make *Suzaku* a powerful tool for investigating hot

and/or high energy sources as well. In the XIS, the background originates from the cosmic X–ray background (CXB) combined with charged particles (the non-X–ray background, or NXB). Currently, flickering pixels are a negligible component of the background. When observing the dark earth (*i.e.* the NXB), the background rate between 0.4–12 keV in is 0.1–0.2 cts/s in the FI CCDs and 0.3–0.6 cts/s in the BI CCD. Note that these are the fluxes after the grade selection is applied with only grade 0, 2, 3, 4 and 6 selected. We show in Figure 6.9 the NXB spectra for each sensor, and their magnifications in Figure 6.10.
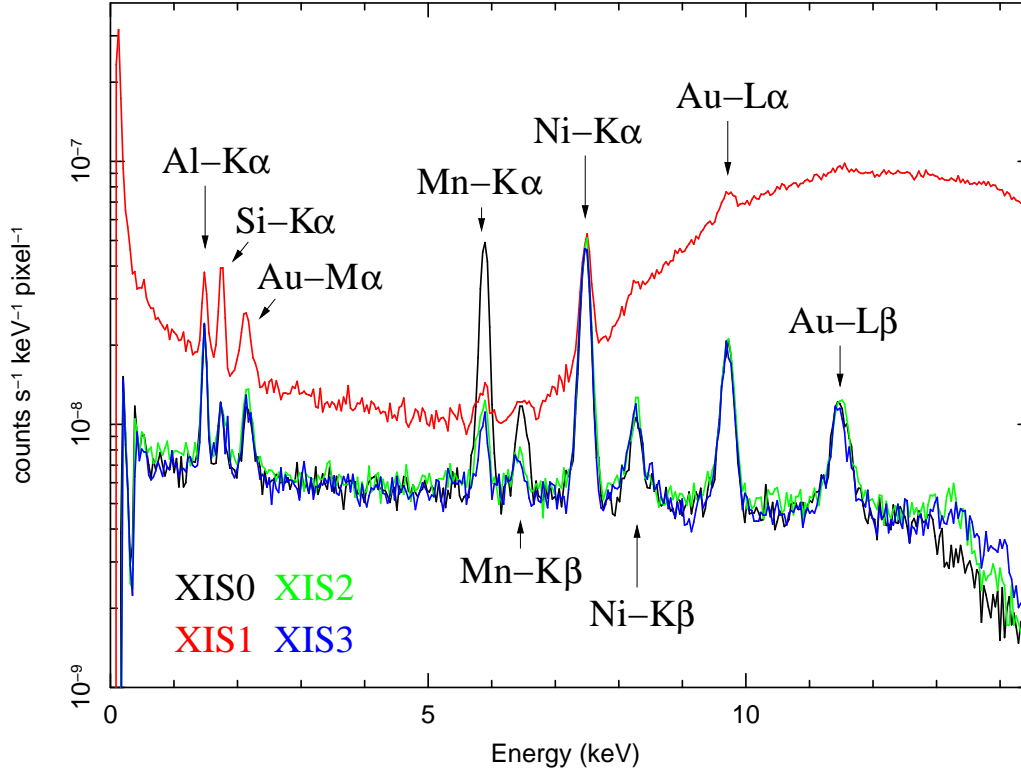
Figure 6.9: The XIS background rate for each of the four XIS detectors, with prominent fluorescent lines marked. These spectra are based on ∼ 800 ks of observations towards the dark Earth.

Note that these are the fluxes after the grade selection is applied with only grade 0, 2, 3, 4 and 6 selected. There are also fluorescence features arising from the calibration source as well as material in the XIS and XRTs. The Mn lines are due to the scattered X-rays from the calibration sources. As shown in Table 6.2 the Mn lines are almost negligible except for XIS-S0. The O lines are mostly contamination from the day earth (§6.9.3). The other lines are fluorescent lines from the material used for the sensor. Table 6.2 shows the current best estimates for the strength of these emission features, along with their 90% upper and lower limits.
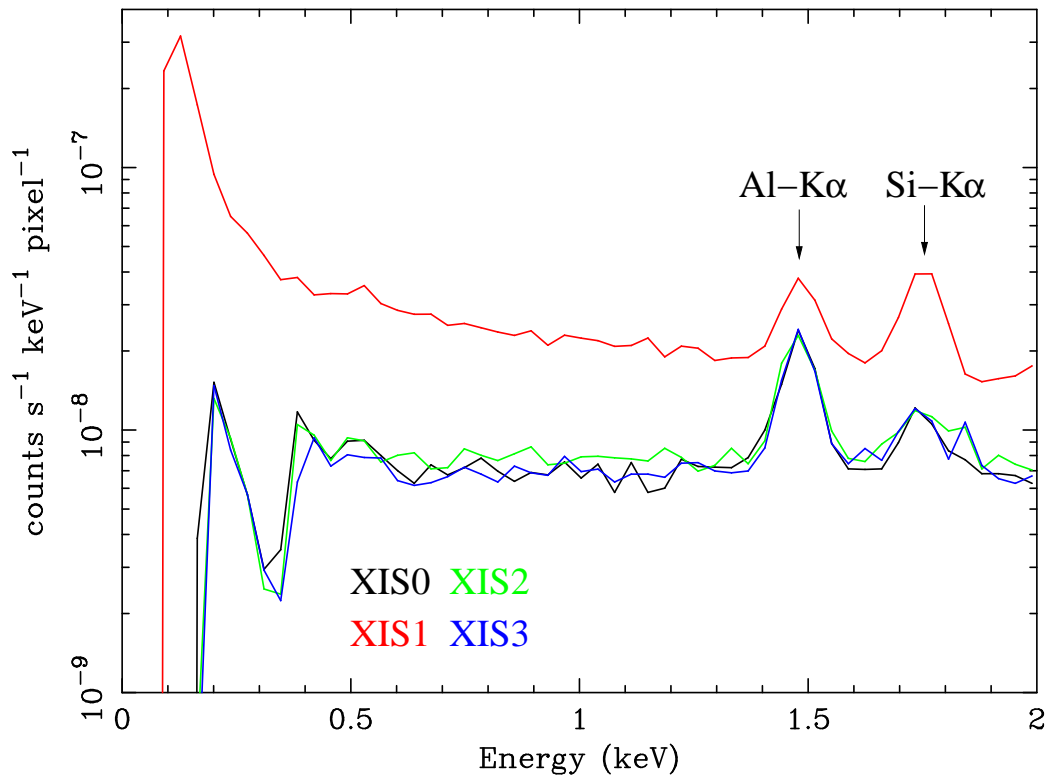
Figure 6.10: The XIS background rate for each of the four XIS detectors, showing only energies between 0.1–2.0 keV. Below 0.3 keV the background rate for the FI chips cannot be determined due to their low effective area.

The NXB is not uniform over the chip. Its flux tends to be slightly higher at larger ACTY as shown in Fig. 6.11. This is because some fraction of NXB is produced in the frame-store region. The fraction may be different between the fluorescent lines and the continuum. This causes slight difference in the ACTY dependence of the NXB.

Total flux of NXB depends on the cut-off rigidity (COR))as shown in Fig. 6.12. This may be natural as the NXB is produced by the charged particles, whose flux is higher at lower COR. This means that, when we use the NXB database to subtract the backgroud, we need to select the NXB with an appropriate range of COR, which match with the COR distribution of the on-source observations. For this purpose, the NXB database available from the *Suzaku* web page is sorted with the COR.

When we estimate the telemetry ocupation of the background, we need to consider not only the X-ray grades (0, 2, 3, 4, 6) but also non-X-ray grades (1, 5, 7). Although the class discriminator removes a large ftaction of non-X-ray background, we still have a non-negligible flux of the background. The background rate on the FI chips (including all
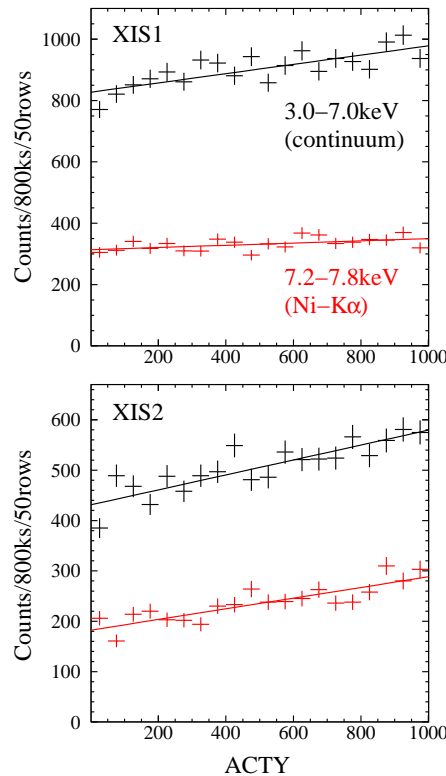
Figure 6.11: ACTY dependence of the NXB for XIS1 and XIS2. The NXB flux tends to be higher at larger ACTY, because some fraction of NXB is produced in the frame-store region.

the grades) is normally less than 10 cnts/sec and that of BI CCD is less than 20 cnts/sec. These values represent 90% upper limits of variations in the background count rates when the class discriminator is applied. These background rates are important when evaluating the possibility of the telemetry saturation at the low data rates (§6.9.4).

6.9   Notes on the XIS observations

6.9.1   Photon pile-up

The XIS is essentially a position-sensitive integrating instrument, with the nominal interval between readouts of 8 s. If during the integration time more than one photons strike the same CCD pixel, or one of its immediate neighbors, these cannot be correctly detected as independent photons: this is the phenomenon of photon pile-up. Here, the modest angular resolution of the *Suzaku* XRT is an advantage. However, photon pile-up could be
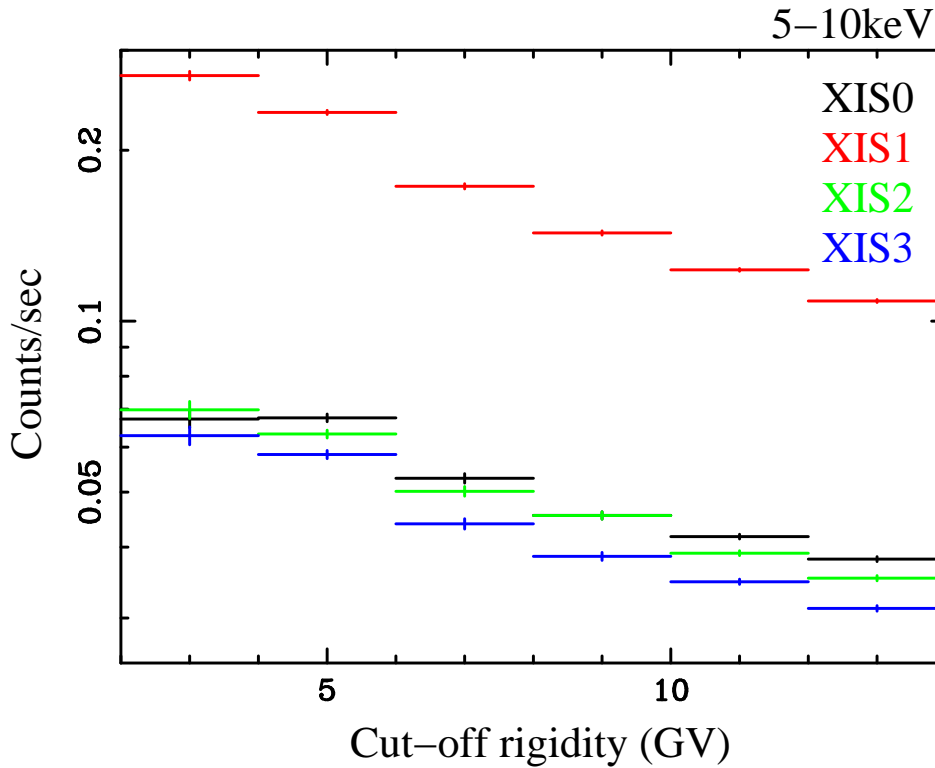
Figure 6.12: Cut-off rigidity dependence of the NXB (average intensity in 5–10 keV) for each sensor. The NXB flux varies by a factor of $\sim$2 depending on the cut-off rigidity.)

a problem when observing bright sources.

If the pile-up occurs, both the image and spectral data are distorted. The energy spectrum tends to become harder from the following reason. In most cases, soft photon flux is much larger than the hard photon flux. This means that, when pile-up occurs, soft photons tend to pile up rather than the hard photons. When soft photons piled up, they may be either discarded as a non-X-ray event or regarded as a signle hard photon. This results in the flux decrease in the soft band and the flux increase in the hard band. The pile-up tends to harden the energy spectrum. Because the decrease of the soft photons overwhelm the increase of the hard photons, the pile-up tends to decrease the total photon flux. In an extreme case, all the events may be discarded as non-X-ray events at the image center, and the local photon flux becomes effectively zero. This means that a point source image would have a hole at the center. This is the simplest method to detect the photon pile-up.

Because the impact of the pile-up to the energy spectrum is different from source to source, it is difficult to give a general criteria of photon pile-up applicable to any sources.

Table 6.2: Major XIS Background Emission Lines

Line	Energy keV	XIS-S0 10^{-9} ct/s/pix	XIS-S1 10^{-9} ct/s/pix	XIS-S2 10^{-9} ct/s/pix	XIS-S3 10^{-9} ct/s/pix
O K	0.5249	18.5 ± 0.5	$69.3^{+2.7}_{-2.6}$	$14.3^{+1.5}_{-1.3}$	$14.1^{+1.1}_{-1.2}$
Al K	1.49	1.98 ± 0.23	3.01 ± 0.51	$1.50^{+0.31}_{-0.28}$	$1.57^{+0.25}_{-0.23}$
Si K	1.740	$0.299^{+0.2080}_{-0.2074}$	2.21 ± 0.45	$0.0644(< 0.282)$	$0.543^{+0.212}_{-0.213}$
Au M	2.1229	0.581 ± 0.234	$1.13^{+0.280}_{-0.291}$	$0.359^{+0.211}_{-0.212}$	$6.69^{+2.91}_{-2.90}$
Mn Kα	5.898	$8.35^{+0.36}_{-0.34}$	0.648 ± 0.289	$0.299^{+0.209}_{-0.2086}$	$0.394^{+0.181}_{-0.18}$
Mn Kβ	6.490	$1.03^{+0.22}_{-0.216}$	$0.294(< 0.649)$	$0.00(< 0.111)$	$0.428^{+0.225}_{-0.226}$
Ni Kα	7.470	7.20 ± 0.31	6.24 ± 0.53	$3.78^{+0.26}_{-0.25}$	$7.13^{+0.36}_{-0.37}$
Ni Kβ	8.265	0.583 ± 0.183	$1.15^{+0.5}_{-0.489}$	0.622 ± 0.206	$0.983^{+0.247}_{-0.249}$
Au Lα	9.671	$3.52^{+0.27}_{-0.28}$	$3.28^{+1.16}_{-0.99}$	$1.88^{+0.31}_{-0.28}$	$3.54^{+0.36}_{-0.35}$
Au Lβ	11.514	$2.25^{+0.73}_{-0.59}$	2.91 ± 1.29	$0.752^{+0.428}_{-0.304}$	$2.67^{+0.61}_{-0.53}$

Note: Typical accumulation time are 110-160 ks

For example, if one tries to look for a weak hard tail in a soft source, photon pile-up may be strictly removed as it can easily mimic the hard tail. On the other hand, a heavily absorbed source with a hard spectrum may be rather insensitive to the photon pile-up. However, some kind of guideline might be useful for the guest observers to roughly estimate the significance of pile-up. We will give detailed estimation later, but the results may be summarized as follows. **In practice, point sources with < 100 cts/exposure can be observed in the normal mode (full window)**. For somewhat brighter sources, window options can be used to reduce the exposure time per frame (the count rate limit is inversely proportional to the exposure time — 1/4 window option reduces the exposure time from 8 s to 2 s, and raises the limit from ~ 12.5 cts/s to $\sim$50 cts/s).

Detailed calculation of photon pile-up is give in Table 6.3. In this table, we summarize the estimated count rates at which the pile-up fraction in an annulus reaches 0, 20, and 50%. For example, for a source with the expected count rate of ~ 12.5 cts/s, $> 50\%$ of the events within ~ 10 pixel of the image center are piled up. On the other hand, the pile-up fraction is restrained below 20% outside the circle of 20 pixel in radius. Note that the attitude fluctuation of the satellite does not mitigate the photon pile-up, because the attitude drift is negligible within the exposure of 8 sec.

When pile-up occurs, the effects need to be removed in the course of the data analysis. Most simple method is to remove the image center from the event extraction region. This means that the events are extracted from an annular region to calculate the energy spectra. In this case, an appropriate arf file need to be calculated depending on the inner/outer radii of the annulus.

Table 6.3: Total count rate which causes prescribed fraction of pile-up at the annulus of the PSF

Radius [pix][1]	Pile-up fraction		
	3%	20%	50%
∼5	13.4	30.0	45.9
5∼10	17.6	43.3	67.7
10∼15	25.6	64.3	101
15∼20	33.8	85.4	134
20∼25	42.6	108	171
25∼30	55.8	142	224
30∼35	70.6	180	285
35∼40	88.2	226	356
40∼45	100	256	404
45∼50	119	304	480
50∼55	141	362	571

Note: in unit of cts/s.
[1] 1 pixel = 1.04 arcsec.

6.9.2 Out-of-time events

X-ray photons detected during the frame-store transfer do not correspond to the true image, but instead appear as a streak or blur in the readout direction. These events are called out-of-time events, and they are an intrinsic feature of CCD detectors. Similar streaks are seen from bright sources observed with *Chandra* and *XMM-Newton*. Out-of-time events produce a tail in the image, which can be an obstacle to detecting a low surface brightness feature in an image around a bright source. Thus the out-of-time events reduce the dynamic range of the detector. Since XIS spends 25 ms (without CI) and 156 ms (with CI) in the frame-store transfer, about 0.3% ($= 0.025/8 \times 100$; without CI) and 2.0% (with CI) of all events will be out-of-time events. However, because the orientation of the CCD chip is different among the sensors, one can in principle distinguish a true feature of low surface brightness and the artifact due to the out-of-time events by comparing the images from two or more XISs.

6.9.3 Day Earth Contamination

When the XIS field of view is close to the day earth (i.e. Sun-lit Earth), fluorescent lines from the atmosphere contaminate low-energy part of the XIS data, especially in the BI chip. Most prominent is the oxygen line, but the nitrogen line may be also noticed (see Fig. 6.10). These lines may be mostly removed when we apply the standard data screening criteria (XIS FOV is at least 20 degree away from the day earth) during the ground processing.

Table 6.4: Telemetry allocation (kbit/s)

Data rate	Weekday (XRS/XIS/HXD)	Weekend (XRS/XIS/HXD)
Superhigh	10/144/66	—
High	10/144/66	—
Medium	1/60/40	1/25/40
Low	1/15/10	1/1/10

However, the flux of the atmospheric fluorescent lines are more or less variable and could become rather large depending on the solar activities.

Small amount of contamination could remain after the standard data screening. Even in this case, the lines may be removed if we subtract background extracted in the same XIS field of view. If background data from other observations or the background database are used, the background subtraction may not completely eliminate the atmospheric lines. In this case, the data screening criterion, i.e. 20 degree from the day earth, may need to be changed.

6.9.4 Telemetry limit

If a large number of events are detected in a frame, only a part of the events is output to the telemetry. The data which cannot be output to the telemetry are discarded. This phenomenon is called a telemetry saturation.

Current telemetry allocation among the XRS/XIS/HXD detectors is summarized in Table 6.4. Although the XRS is not functioning, small amount of telemetry is allocated to monitor the HK data. The ratio depends on the data rate and may be changed in future. Due to staffing constraints, the available telemetry is slightly lower over the weekend. "High" rate telemetry is always 144 kbits/s, but "Medium" rate is 60 kbits/s during the week and 25 kbits/s over the weekend. Therefore, mission operation team tries not to allocate bright sources in the weekend.

Because the on-board XIS data are processed in unit of 8 seconds in accordance with the standard exposure time, the available telemetry per sensor is 36864 byte in data rate "High", 15360 byte in the data rate "Medium (weekday)", and 6400 byte in data rate "Medium (weekend)". Here we assume an equal distribution of telemetry allocation among the 4 sensors. As the HK data and the frame header occupy some constant fraction of the telemetry, the rest is allocated to the X-ray events.

We list in table 6.5 a typical size of an event in each editing mode. Because the event is lightly compressed on board, the event size listed in the table should be regarded just representative values. The event compression efficiency depends on the grades of the events,

Table 6.5: Typical event size after compression (byte)

Edit mode	Minimum	Maximum	Average
5×5	28	52	40
3×3	15	23	19
2×2	8	11	9
Timing	4	4	4

Table 6.6: Telemetry limits (cts/s/XIS)

Data rate	5×5	3×3	2×2	timing
Superhigh	112 (101)	236 (220)	498 (475)	1120 (1085)
High	112 (101)	236 (220)	498 (475)	1120 (1085)
Medium (weekday)	45 (39)	95 (85)	201 (187)	452 (430)
Medium (weekend)	17 (13)	36 (30)	77 (68)	172 (159)
Low (weekday)	10 (7)	20 (16)	43 (36)	96 (86)

Note: Nominal telemetry allocation for XIS and its equal distribution among the 4 sensors are assumed. Values in the parenthesis are maximum mean count rates which do not cause telemetry saturation even if the 3σ statistical fluctuation is considered.

thus the spectral shape of the source. Table 6.6 shows the estimated telemetry limits of XIS in various editing modes and the telemetry data rates. We take into account $+3\sigma$ fluctuation of the count rate. The upper limit of source count rate can be estimated by subtracting the background count rates (10/20 cnts/s for FI/BI at 90% upper limits) from the values in Table 6.6.

6.10 Guideline for the XIS clock/editing mode selection

When we consider an appropriate XIS clock/editting mode for a target, we generally need to consider both the telemetry limit and the photon pile-up. However, only the telemetry limit may be concerned for the diffuse sources, which are more extended than the angular resolution of the XRT.

We give the recommended editing mode for a give data rate for a diffuse source in Table 6.7. In the table, we consider $+3\sigma$ fluctuation of the source count rate and the contribution of the background count rate. Here we assume that the source count rates for the FI CCDs are nearly equal to that for the BI CCD. However, the ratio of source count rates depends on the energy spectrum. In case of the ratio of > 2, the boundaries of the source count rate is changed by a factor of $1.3 \sim 1.5$ and some of telemetry modes cannot

Table 6.7: Recommended XIS modes for a diffuse source

Rate[1]	Telemetry Mode	
cts/s	High	Medium
0–66	5×5	3×3
66–82	5×5	FI : 2×2, BI : 3×3
82–124	3×3	FI : 2×2, BI : 3×3
124–202	3×3	(not usable in standard settings)[2]
202–343	FI : 2×2, BI : 3×3	(not usable in standard settings)[2]
> 343	Apply burst option	

[1]Count rate for a single XIS sensor.
[2]Difficult to obtain useful data due to the telemetry saturation, unless output event rate was reduced, e.g., by the area discriminator. GOs cannot select the data rate.

be used.

We summarize the recommended XIS modes for a point source in Table 6.8. Here we adopt 20 cts/s as a pile-up limit, which corresponds to the pile-up fraction of $< 50\%$ at > 15 pixel from the image center. However, as explained previously, appropriate pile-up limit depends on the spectral shape of the source and the science goal of the observations. If a pile-up needs to be avoided completely, one should consider using the window option even if the source count rate is ~ 20 cts/s. For a source brighter than ~ 320 cts/s, it may be difficult to avoid the photon pile-up and/or the telemetry saturation. Guest observers who plan to observe very bright sources should consult with the *Suzaku* personnel at ISAS/JAXA or the NASA *Suzaku* GOF for the optimal observation mode.

6.11 In-flight Calibration of XIS

In this section, we summarize the current status of the XIS flight calibration. Because the calibration information is updated frequently, it is expected that the description in this section may become obsolete quite soon. Latest calibration information may be found in the *Suzaku* web page. The XIS team has been calibrating mainly the 5×5 and 3×3 data in the normal mode, because they are the most frequently used modes. At the time of writing, we have just started the calibration of the data with the window and window+burst options including 2×2 mode. However, calibration of the timing mode remains very preliminary stage yet. Since the introduction of the spaced-row CI may change the XIS performance largely, the XIS team will soon work on the recalibration of the CI data, which will be added to the current calibration data.

In the followings, we describe the current status of the on-board calibration. The

Table 6.8: Recommended XIS modes for a point source

Rate[1]	Telemetry Mode		Clock	Efficiency[2]
cts/s	High	Medium		%
0–20	5×5	3×3	Normal	100
20–66	5×5	3×3	1/4 Window	100
66–80	5×5	FI : 2×2, BI : 3×3	1/4 Window	100
80–132	5×5	3×3	1/4 Window + 1 sec Burst	50
132–160	5×5	FI : 2×2, BI : 3×3	1/4 Window + 1 sec Burst	50
80–124	3×3	FI : 2×2, BI : 3×3	1/8 Window	100
124–160	3×3	(not usable in standard settings)[3]	1/8 Window	100
160–264	5×5	3×3	1/4 Window + 0.5 sec Burst	25
264–320	5×5	FI : 2×2, BI : 3×3	1/4 Window + 0.5 sec Burst	25
160–248	3×3	FI : 2×2, BI : 3×3	1/8 Window + 0.5 sec Burst	50
248–320	3×3	(not usable in standard settings)[3]	1/8 Window + 0.5 sec Burst	50

[1]Count rate for a single XIS sensor.
[2]Out-of-time event due to the Spaced-row CI is not considered.
[3]Difficult to obtain useful data due to the telemetry saturation, unless output event rate was reduced, e.g., by selecting only one/two out of 4 sensors. GOs cannot select the data rate.

calibration items are as follows; (1) charge transfer efficiency, (2) energy scale, (3) energy resolution, (4) pulse height distribution function, (5) quantum efficiency at the low X-ray energy band (contamination) and (5) quantum efficiency at the high X-ray energy band.

6.11.1 Charge Transfer Efficiency and Energy Scale

The CTI is increasing since the launch of *Suzaku* due to the irradiation of charged particles on-orbit. We continuously measure the center energy and FWHM of the main peak from the two ^{55}Fe calibration sources. These calibration sources illuminate CCD segments A and D at the far corners from the read-out nodes. Figure 6.13 shows the on-orbit time history of the center energy of the main peak. The apparent linear trend is due to a charge loss caused by the gradual increase of the CTI.

Thus, we measured the CTI with the observation of the calibration source of ^{55}Fe, the

galactic center region, the Sgr C region and a couple of clusters of galaxies mainly using the iron band and the Cygnus loop for low X-ray energy band. Since the X-ray sources are diffuse extending over the FOV of XIS and have strong emission lines, they are suitable for the calibration of CTI as a function of the distance from the read-out node.

Through the observation, we update the relevant correction parameters regularly and keep the absolute energy error within ±0.2% at the iron Kα energy and within ±5 eV below 1 keV, successfully. The energy scale was verified with the PV data of some clusters of galaxies and E0102–72 for the iron and oxygen bands, respectively.

As of Oct. 1, 2006, the calibration at $\sim$ 2 keV band including silicon edge is rather poor. This is the main uncertainty in the energy scale calibration, which may be improved soon.
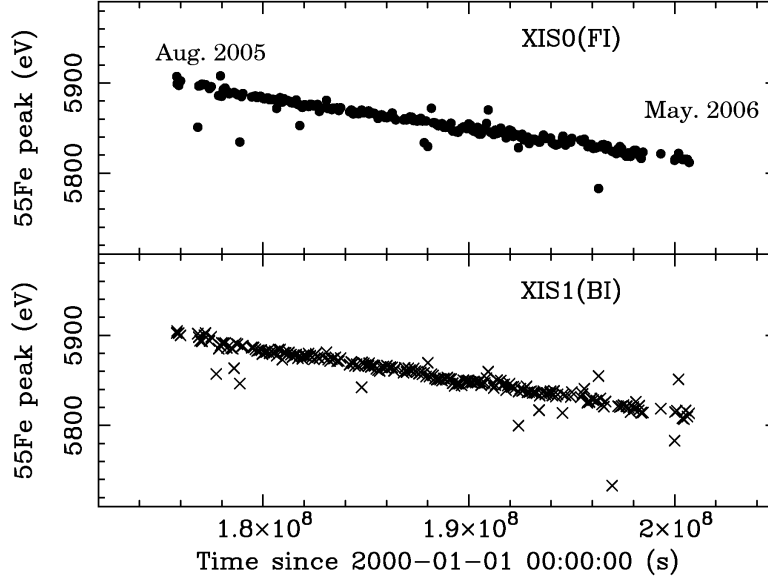

Figure 6.13: The time history of the center energy of Mn Kα from the ^{55}Fe calibration sources for XIS0 (FI) and XIS1 (BI).

6.11.2   Energy Resolution and Pulse Height Distribution Function

The calibration of degradation of the energy resolution with time is done with the calibration source of ^{55}Fe and E0102–72 and is verified with the data of the galactic center region and the Cygnus loop. Figure 6.14 shows the time history of the energy resolution of the main peak of the calibration line of 5.9 keV X-ray irradiated at the edge of the detector.

Against the pre-flight energy resolution of 60 eV at $\sim$ 0.65 keV, Figure 6.15 shows the
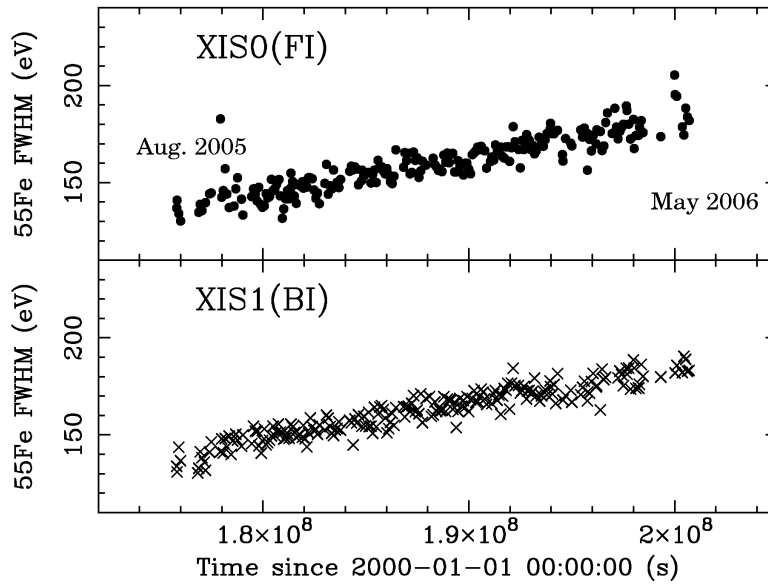
Figure 6.14: The time history of the energy resolution for Mn Kα from the ^{55}Fe calibration sources for XIS0 (FI) and XIS1 (BI).

"extra" line width obtained with the data of E0102–72 by comparison with those from the Chandra HETG.

Evolution of the XIS energy resolution may be expressed by the following formula. Positional dependence of the energy resolution is negligibly small at present compared to its accuracy of determination. This formula is simply obtained by introducing a time dependence to the coefficients of the incident X-ray energy E_X.

$$\Delta E(E_X, t) = \sqrt{a + b(t)E_X + c(t)E_X^2}$$

While a is read-out noise fixed to the value obtained with the ground calibration, the time variable parameters of $b(t)$ and $c(t)$ are determined with the data of ^{55}Fe and E0102-72 mentioned above. Main source of the degradation in the energy resolution is the column-to-column variations of the CTE. CTE of each column can be measured with high accuracy and efficiency using the charge injection. Thus, CTE can be corrected for each column. The XIS team has been measuring the CTI of each column once or twice every two months from May 2006. The degradation of the energy resolution may be incorporated in rmf. Guest observers can make the appropriate rmf for their observations using `xisrmfgen`, which is not yet relaesed as of Oct. 1, 2006, but will be released soon.

In spite of the degradation of the energy resolution, the XIS team dose not expect to change the pulse height distribution function (line profile to the monochromatic X-rays) on-
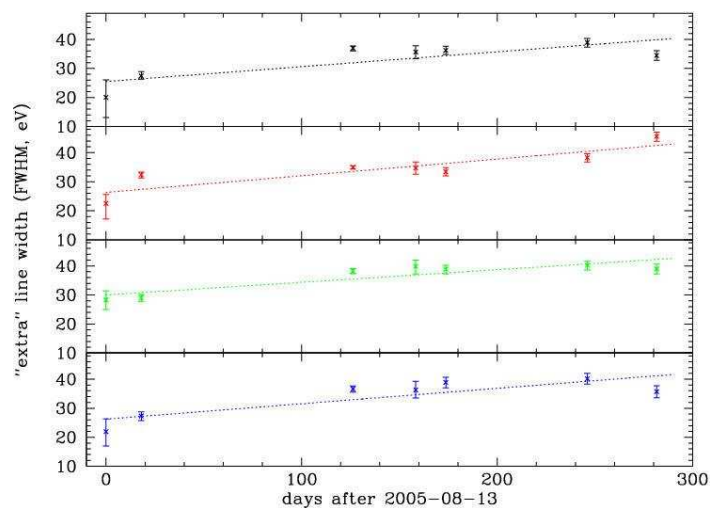
Figure 6.15: The time history of the "extra" line width at O-K band against the pre-flight energy resolution of 60eV in FWHM.

orbit except for the energy resolution. The results from the pre-flight ground experiments are used in `xisrmfgen`.

6.11.3 Quantum Efficiency

The contamination is the main issue related to the calibration of the quantum efficiency at the low X-ray energy band. The status of the calibration is found in the section 6.7. The calibration of quantum efficiency above $\sim 1 - 2$ keV is done mainly with the Crab nebula. The current status is given in the section of XRT.

Chapter 7

Hard X–ray Detector

Figure 7.1: The Hard X–ray Detector before installation.

The Hard X–ray Detector (HXD; see Figure 7.1) is a non-imaging, collimated hard X–ray scintillating instrument sensitive in the ~ 10 keV to ~ 600 keV band. It has been developed jointly by the University of Tokyo, Aoyama Gakuin University, Hiroshima Uni-

81

versity, ISAS/JAXA, Kanazawa University, Osaka University, Saitama University, SLAC, and RIKEN. Its main purpose is to extend the bandpass of the *Suzaku* observatory to the highest feasible energies, thus allowing broad-band studies of celestial objects.
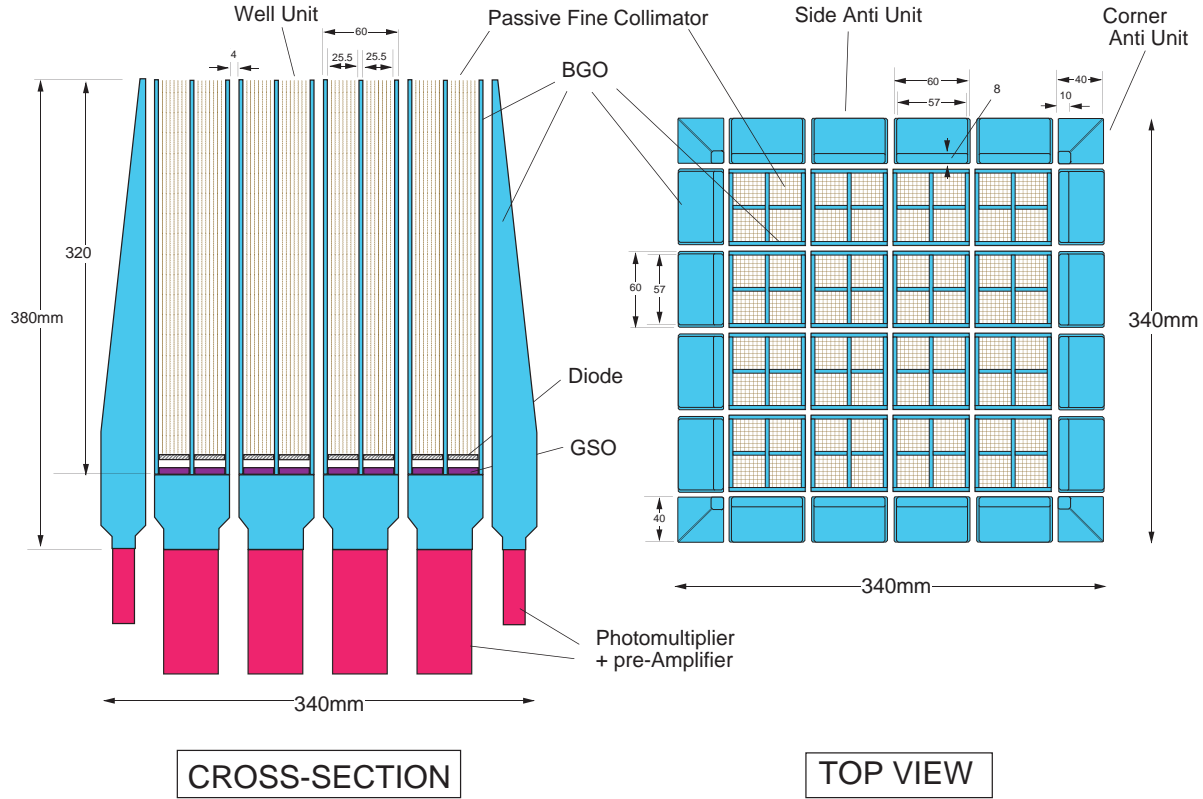

Figure 7.2: Schematic picture of the HXD instrument, which consists of two types of detectors: the PIN diodes located in the front of the GSO scintillator, and the scintillator itself.

The HXD sensor (HXD-S) is a compound-eye detector instrument, consisting of 16 main detectors (arranged as a 4×4 array) and the surrounding 20 crystal scintillators for active shielding. Each unit actually consists of two types of detectors: a GSO/BGO phoswich counter, and 2 mm-thick PIN silicon diodes located inside the well, but in front of the GSO scintillator. The PIN diodes are mainly sensitive below ~ 60 keV, while the GSO/BGO phoswich counter (scintillator) is sensitive above ~ 40 keV. The scintillator signals are read out by photomultiplier tubes (PMTs). The schematic drawing of the HXD is given in Fig. 7.2. The HXD features an effective area of ~ 160 cm^2 at 20 keV, and ~ 260 cm^2 at 100 keV; (see Fig. 2.5). The energy resolution is ~ 4.0 keV (FWHM) for the PIN diodes, and $7.6/\sqrt{E}$ % (FWHM) for the scintillators where E is energy in MeV. The HXD time resolution is 61 μs.

7.1   GSO/BGO Counter Units

Each main detector unit is of a well-type design with active anti-coincidence shields. The shields and the coarse collimator itself are made of Bismuth Germanate (BGO; $Bi_4Ge_3O_{12}$) crystals, while the X–ray sensing material "inside the well" is GSO (Gadolinium Silicate, or $Gd_2SiO_5(Ce)$) crystal. The aspect ratio of the coarse collimators yields an acceptance angle for the GSO of 4.5º (FWHM). Each unit thus forms a 2×2 matrix, containing four 24 mm $\times$ 24 mm, 5 mm thick GSO crystals, each placed behind the PIN diode. The BGO crystals are also placed underneath the GSO sensors, and thus each well is a five-sided anti-coincidence system. The effective thickness of the BGO active shield is thus about 6 cm for any direction from the PIN and GSO, except for the pointing direction.

The reason for the choice of the two different crystals for the sensor and the shield is dictated by the large stopping ability of both, yet the very different rise/decay times, of ~ 700 ns for BGO, and ~ 120 ns for GSO, at a working temperature of -20ºC. This allows for an easy discrimination of the shield vs. X–ray sensor signals, where a single PMT can discriminate between the two types of scintillators in which an event may have occurred. Any particle events or Compton events that are registered by both the BGO and GSO can be rejected by this phoswich technique, utilizing custom-made pulse-shaping LSI circuits.

7.2   PIN-Si Diodes

The low energy response of the HXD is provided by 2 mm thick PIN silicon diodes, placed in front of each GSO crystal. The geometrical area of the diode is 21.5×21.5 mm^2, while the effective area is limited to be $\sim 16.5 \times 16.5$ mm^2 by the guard ring structure. The temperature of PIN diodes are controlled to be -15$\pm$3 C to suppress electrical noises caused by the leakage current, and almost fully depleted by giving a bias voltage of ~ 500 V [1]. The PIN diodes absorb X–rays with energies below ~ 70 keV, but gradually become transparent to harder X–rays, which in turn reach and are registered by the GSO detectors. The X–rays are photoelectrically absorbed in the PIN diodes, and the signal is amplified, converted to a digital form, and read out by the associated electronics. The PIN diodes are of course also actively shielded from particle events by the BGO shields, as they are placed inside the deep BGO wells. In addition, to reduce the contamination by the cosmic X-ray background, passive shields called "fine collimators" are inserted in the well-type BGO collimator above the PIN diodes. The fine collimator is made of 50 μm thick phosphor bronze sheet, arranged to form a 8×8 square meshes of 3 mm wide and 300 mm long each.

---

[1]The bias voltage from two out of four high-voltage units is reduced to 400 V (as of 2006 October). The total effective area of PIN diodes will decrease by $\sim 6\%$ above 20 keV.

7.3 HXD Field of View

The field of view of the HXD changes with incoming energy. Below ~ 100 keV, the passive fine collimators define a $34' \times 34'$ FWHM square opening as shown in figure 7.3. The narrow field of view compared to Beppo-SAX-PDS and RXTE-HEXTE experiments is one of the key advantages of HXD observations. Above ~ 100 keV, the fine collimators become transparent and the BGO active collimator defines a $4.5° \times 4.5°$ FWHM square opening. In summary, all the PIN energy range and the lower quarter of the GSO range has a field of view of $34'$, while the GSO events above ~ 100 keV have wider field of view, up to $4.5°$.
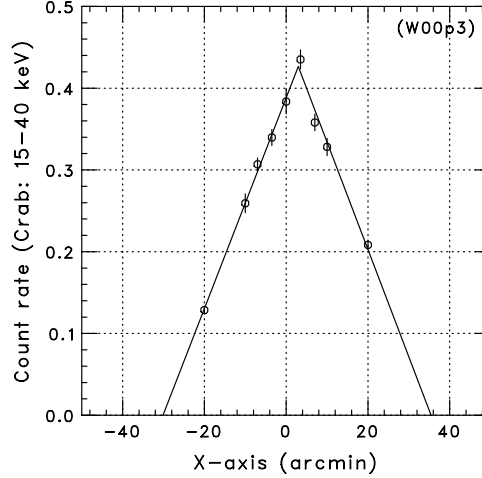

Figure 7.3: An angular response of single fine-collimator along the satellite X-axis, obtained from offset observations on the Crab nebula.

7.4 In-Orbit background of PIN and GSO

Although the HXD is a non-imaging instrument, its instantaneous background can be reproduced through modeling, without requiring separate off-source observations. The HXD has been designed to achieve an extremely low in-orbit background ($\sim 10^{-4}$ c s^{-1} cm^{-2} keV^{-1}), based on a combination of novel techniques: (1) the five-sided tight BGO shielding as mentioned above; (2) the use of the 20 shielding counters made of thick BGO crystals which surround the 16 main GSO/BGO counters; (3) sophisticated onboard signal processing and onboard event selection, employing both high-speed parallel hardware circuits in the Analog Electronics, and CPU-based signal handling in the Digital Electronics; and (4) the careful choice of materials that do not become strongly radio-activated under in-orbit particle bombardment. Finally, (5) the narrow field of view below ~ 100 keV defined by the fine collimator effectively reduces both the CXB contribution

and the source confusion. For example, the CXB is only $\sim 5\%$ of the PIN count-rate and its fluctuation is estimated to be $\lesssim 1\%$.
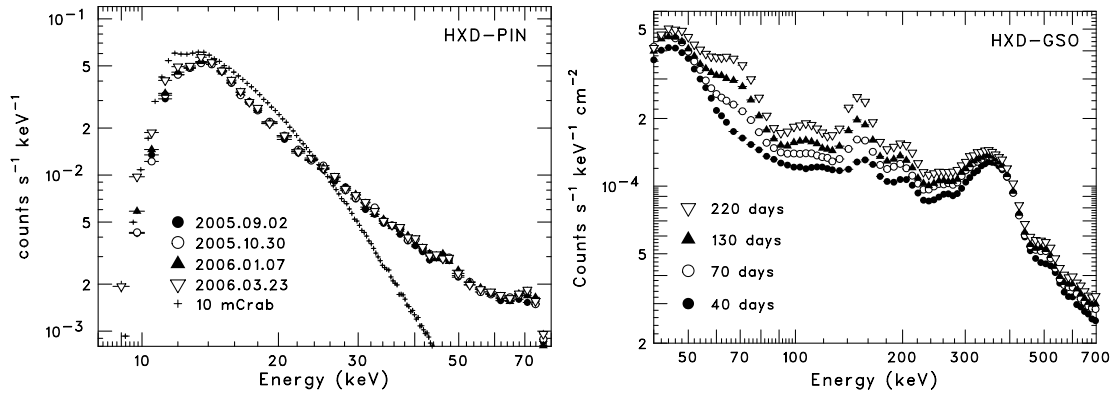

Figure 7.4: [Left] A comparison of average non X–ray background spectra of PIN, measured during the first six months of the mission. The Crab spectrum scaled down with two orders of magnitude are shown together. [Right] The evolution of averaged GSO-NXB spectra during the first half year after the launch.

The non X–ray background (NXB) of PIN diodes, measured in orbit, is plotted in the left panel of Fig. 7.4. The average background counting rate summed over the 64 PIN diodes is ~ 0.6 ct s^{-1}, which is roughly equal to a 10 mCrab intensity. In addition, almost no long-term growth has been observed in the PIN-NXB during the first year of Suzaku, thanks to the small activation effect of silicon. On the contrary, as shown in the right panel of Fig. 7.4, a significant long-term accumulation caused by the in-orbit activation has been observed in the GSO-NXB, especially at the early phase of the mission. The background spectrum of GSO contains several activation peaks, whose intensities exponentially increased with individual half-lives. Since the longest half-life is about one year, the GSO-NXB level can be treated as saturated in the AO-2 phase.

Figure 7.5 illustrates the comparison between detector backgrounds of hard X-ray missions. The lowest background level per effective area is achieved by the HXD at an energy range of 12–70 and 150–500 keV. The in-orbit sensitivity of the experiment can be roughly estimated by comparing the background level with celestial source intensities indicated by dotted lines. Below 30 keV, the level is smaller than 10 mCrab intensity, which means a sensitivity better than 0.3 mCrab can be obtained, if an accuracy of 3% is achieved in the background modeling.

Since the long-term variation of both PIN-NXB and GSO-NXB can be expected to be stable, the main uncertainties of the background come from temporal and spectral short-term variations. As shown in Fig 7.6, the PIN-NXB shows a significant short-term variability, with a peak-to-peak amplitude of factor 3, anti-correlating with the cut-off rigidity (COR) in the orbit. Since the COR affects the flux of incoming primary cosmic-
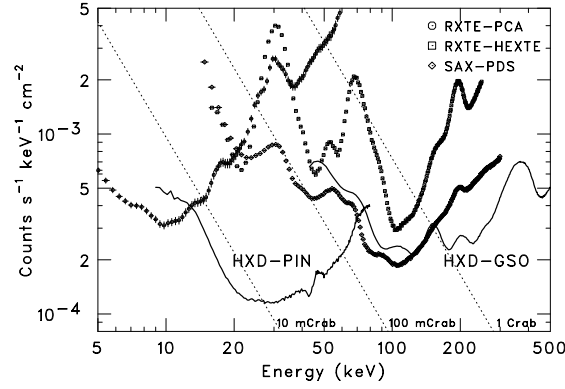
Figure 7.5: A comparison of the in-orbit detector background of PIN/GSO, averaged over 2005 August to 2006 March and normalized by individual effective areas, with those of RXTE-PCA, RXTE-HEXTE, and BeppoSAX-PDS. Dotted lines indicate 1 Crab, 100 mCrab, and 10 mCrab intensities.
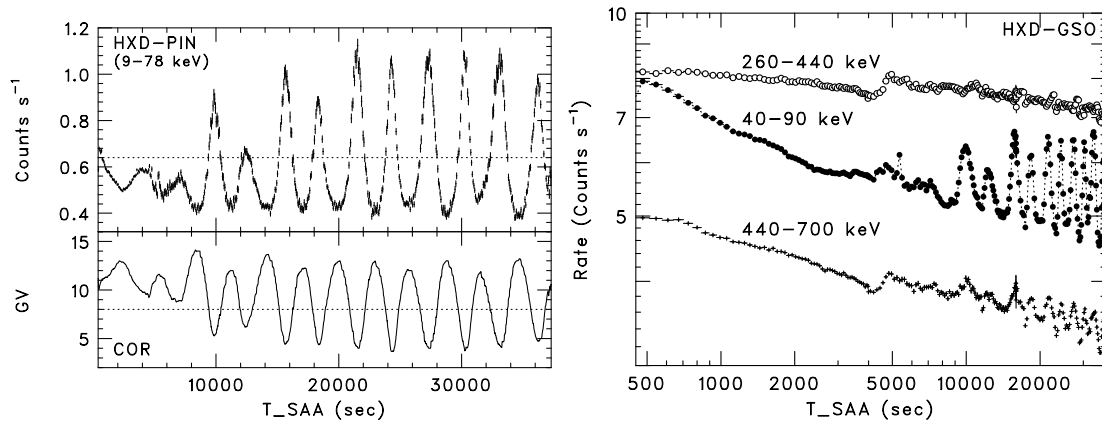

Figure 7.6: [Left] A light curve of the non X–ray background of PIN, folded with the elapsed time after the SAA passage (*top*), and a plot of averaged cut-off rigidity at the corresponding position (*bottom*). [Right] The same folded light curves of the GSO background, in 40–90, 260–440, and 440-70 keV energy band.

ray particles, most of the PIN-NXB is considered to originate in the secondary emissions produced by the interactions between cosmic-ray particles and surrounding materials of the detector. When a screening criterion of COR>8, a standard cut ¿ in the pipe-line processing, is applied for the event extraction, the amplitude decreases to a factor ∼1.5. During this temporal variation of the PIN-NXB, its spectral shape slightly changes; larger deviations from the average are observed at the higher energy range. In case of the GSO-NXB, as shown in the right panel of FIg 7.6, the temporal variation differs at different energy

bands. In the lower energy range, a rapid decline after the SAA passage clearly appears, in addition to the similar anti-correlation with the COR. Therefore in the background modeling, all these temporal and spectral behaviors have to be properly handled.

7.5   Background modeling and current reproducibility

As is the case for every non-imaging instrument (and in particular, for those sensitive in the hard X-ray range), the limiting factor for the sensitivity of the HXD is the reproducibility in the background estimation. Since this is the first space flight of the HXD-type detector, and the reproduction of the in-orbit background is not at all an easy task, the modeling accuracy evolves with the experience of in-orbit data, and the latest status of the estimation error and procedures will be regularly presented on the *Suzaku* websites listed in Appendix C. For the AO-2 proposal preparation, the method, limitations, and reproducibilities (as a function of the integration time and the energy range) of the current background modeling are briefly described below. When preparing the AO-2 proposal, authors should evaluate the systematic error in their planned observation based on the information in this document.

Since there is a strong anti-correlation between the PIN-NXB and COR, the background modeling of the PIN is primarily based on the counting rate of high-energy charged particles, directly measured by the PIN diodes. Due to large energy depositions inside the silicon, penetrations of cosmic-ray particles cause large signals in the corresponding PIN diodes, and hence activate the upper discriminator (UD) in the analog electronics, and then recorded as the PIN-UD monitor count in HK data. Therefore, the PIN-UD rate directly indicates the flux of primary cosmic-ray particles, and the background counting rate at any period can be estimated based on the corresponding PIN-UD rate. In the actual modeling procedure, the PIN-NXB rate is described by a summation of raw PIN-UD rate and integrated PIN-UD rate with a fixed decaying time constant, to take into account the small effect of the activation during SAA passages. The spectral shape of the PIN-NXB is assumed to depend on the "estimated" background rate, and is extracted from a database of PIN-NXB spectrum at each estimated rate, which is built from the earth occultation data. In Fig. 7.7, comparisons between the real data obtained during the earth occultation of a 4-day long observation and the model prediction of PIN-NXB are shown, individually for 15–40 and 40–70 keV energy bands and for 1, 4, 8, 16, 32 ks and 1 day time-scales. In the shorter time-scales, the reproducibility become worse, not only statistically but also systematically because of the difficulty of modeling. The distributions of the residuals, obtained from ten long observations are shown in Fig. 7.8

The temporal and spectral behaviors of the GSO-NXB are more complicated than those of the PIN-NXB, since they are determined from individual characteristics of radio-active isotopes produced by the in-orbit activation. The current modeling of the GSO-NXB utilizes the fittings of light curves in 32 energy bands, which are obtained in the earth occultation periods. In individual energy bands, normalizations of model components,

namely, a cosmic-ray particle term calculated from the PIN-UD rate, and a few activation terms which show exponential decays with fixed time constants after the SAA passages, are determined. Then, the background rate at a certain band during the observation of celestial sources can be predicted by adopting the same set of parameters. Note that the spectrum should be rebinned into 32 energy band to match the background model in analysis. In Fig. 7.9, comparisons between the real data obtained during the earth occultation of a 4-day long observation and the model prediction of GSO-NXB are shown, individually for 50–100 and 100–200 keV energy bands and for 1, 4, 8, 16, 32 ks and 1 day time-scales. The distributions of the residuals, obtained from ten long observations are shown in Fig. 7.10

As already mentioned, authors should by themselves evaluate the systematic error necessary to include in one's observation and analysis plan. Here, we present an example of a 100 ks observation aiming at a "detection" (i.e., not spectroscopy) of any hard emission. For PIN and GSO, the most sensitive energy bands are at the softest ends. In Figs. 7.8 and 7.10, the HXD background reproducibility of 1-day long observations is found to be $\sim \pm 4\%$ and $\sim \pm 2\%$, for PIN in 15-40 keV and GSO in 50-100 keV, respectively. Of these, the PIN background is so low that its modeling accuracy is currently limited by statistics of the background database accumulated so far. As the background data become more plenty, the PIN background accuracy will naturally improve, to attain, say, 3% in 1–2 years. Observers can later re-analyze their data using more improved future background models, to get more reliable background subtraction. The GSO background, in contrast, is systematics limited, and hence the strategy for improving its modeling is less straightforward. While the particular examples presented here attain an accuracy of $\sim \pm 2\%$, it is not yet confirmed that this accuracy can be achieved by all 1-day long observations to be conducted under various conditions. Therefore, observers are recommended at this stage to employ a slightly more conservative estimate, $\sim \pm 3\%$, as the immediate GSO background modeling accuracy, with a prospect that the accuracy will be improved to $\sim \pm 2\%$ (or potentially even better) through future re-analyses of the same data using improved GSO background modelings. For reference, Fig. 7.11 presents the theoretical sensitivity calculation results; the limit when a 3% systematic error of the background modeling is assumed for both PIN and GSO, and the limit solely determined by the statistical error with a 100 ks exposure. Since the statistical and systematic errors differ according to the situation, proposer should consider the expected errors based on the integration time and energy band they are interested in.

For the line detection, the situation is far more complicated. The gain accuracy, response anomalies, and time dependent background spectra should all be taken into account. Authors interested in line detection is strongly recommended to contact the HXD experts.

7.6 Data analysis procedure

HXD data are accumulated by event by event basis. After on-board data selection, event data are further screened by the ground pipe-line analysis process. By referring to the

trigger and flag information (including the inter-unit anti-coincidence hit patterns), the pipe-line assigns specific grades to the HXD events such as pure PIN events and pure GSO events. Detector responses and background files that match the particular grade of the events will be provided by the HXD team. With progress of background modeling, these background files will be updated for all existing observations to date. Note that currently there are no user-specified parameters for the HXD.

7.7 The Anti-coincidence counters as a Wide-band All-sky Monitor (WAM)

Tight active shielding of HXD results in a large arrays of guard counters surrounding the main detector parts. These anti coincidence counters, made of ~ 4 cm thick BGO crystals, have a large effective area for sub-MeV to MeV gamma-rays. With limited angular ($\sim 5°$) and energy ($\sim 30\%$ at 662 keV) resolutions, they works as a Wide-band All-sky Monitor (WAM).

Analog signals from normally four counters in each side of HXD sensor are summed up and a pulse height histogram is recorded each second. Thus the WAM is monitoring the hard X-ray universe as well as the Solar flares. If a transient event such as gamma-ray burst (GRB) is detected, four energy band light curve with finer (31.25 ms) timing resolution is also recorded. The energy coverage of WAM is from ~ 50 keV to ~ 5 MeV, and its effective area is ~ 800 cm^2 at 100 keV and 400 cm^2 at 1 MeV. These data are shared with PI and the HXD team; the PI can utilize the full set of WAM data. Because these transient events, especially GRBs, need spontaneous contribution to the community, the HXD team will make the analysis products, such as light curves and spectra, public as soon as possible from: `http://www.astro.isas.jaxa.jp/suzaku/HXD-WAM/WAM-GRB/`.
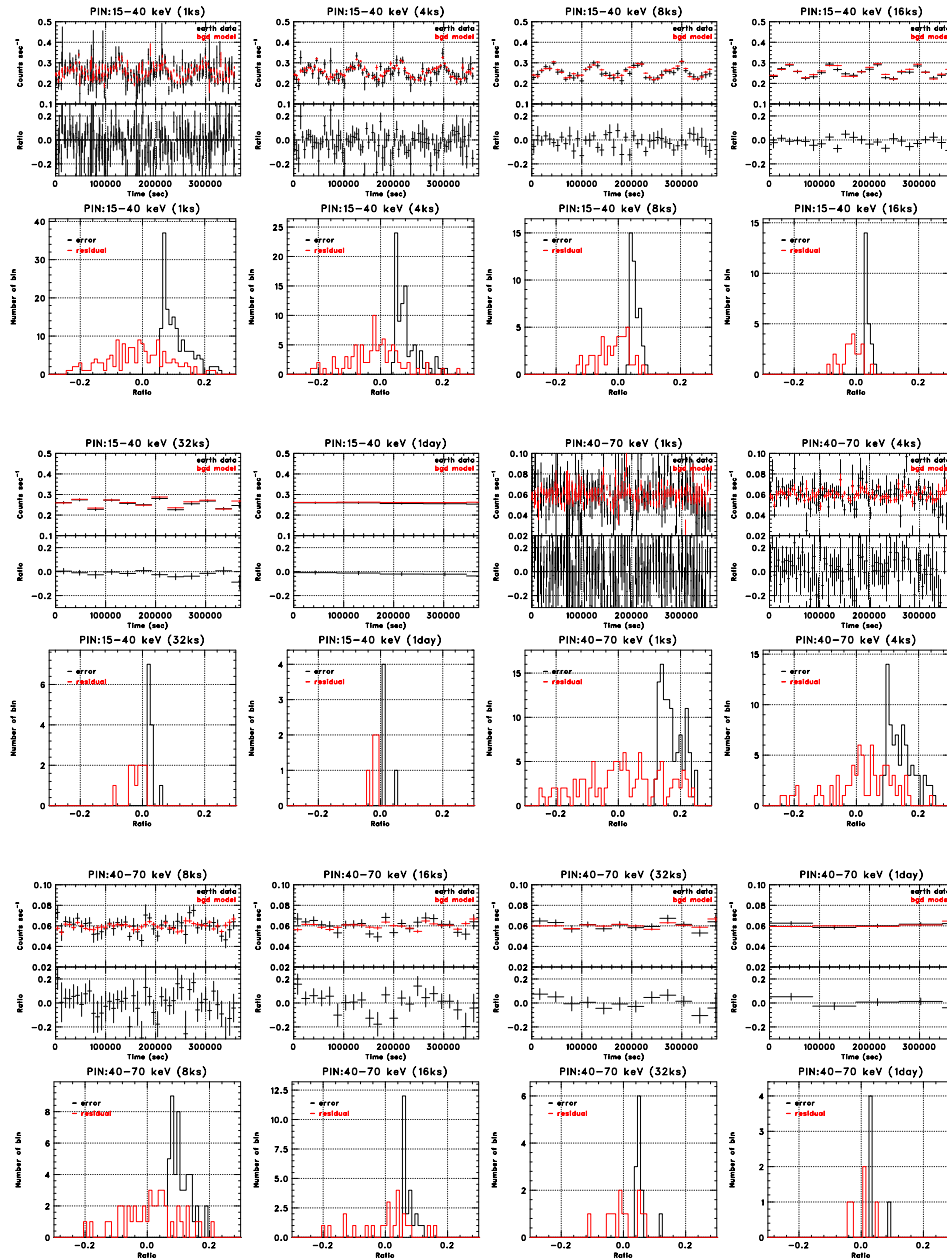
Figure 7.7: Example of comparisons between the real data and the background model prediction of the PIN-NXB for various time bins of 1, 4, 8, 17, 32 ks, and 1 day, for one SWG observation. Earth occultation data of ten long (a few days) observations are used in the plot. The first 6 panels show the case in the energy range of 15–40 keV, while the last 6 panels do the case in the 40-70 keV. The upper figures show the comparisons of the light curves and residuals. Here the residuals represent the ratio against the total background count rate. The lower figures show the distributions of the residual (red) and the statistical error (black).
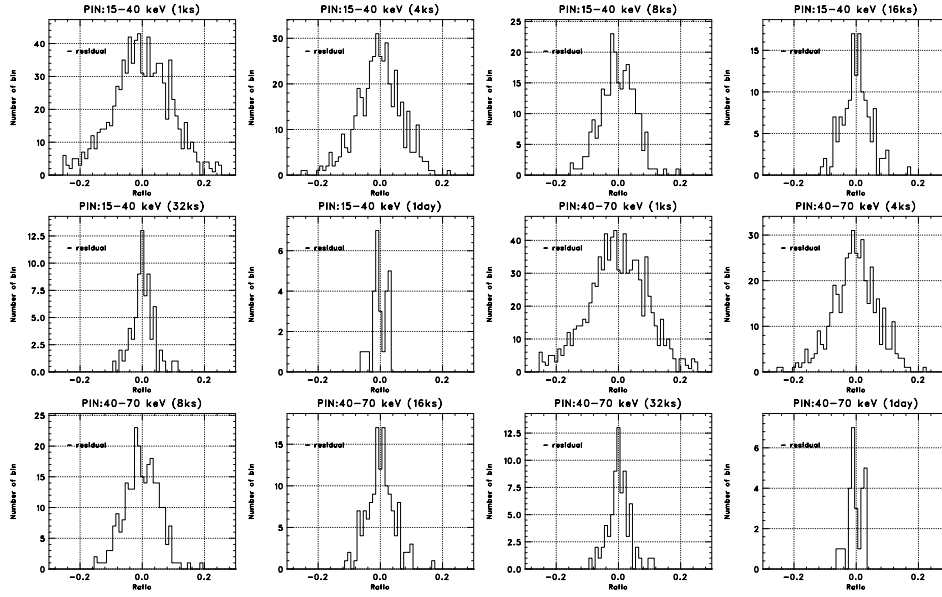
Figure 7.8: The same plots as the residual distributions of the PIN-NXB modeling shown in figure 7.7, but extracted from ten long observations.
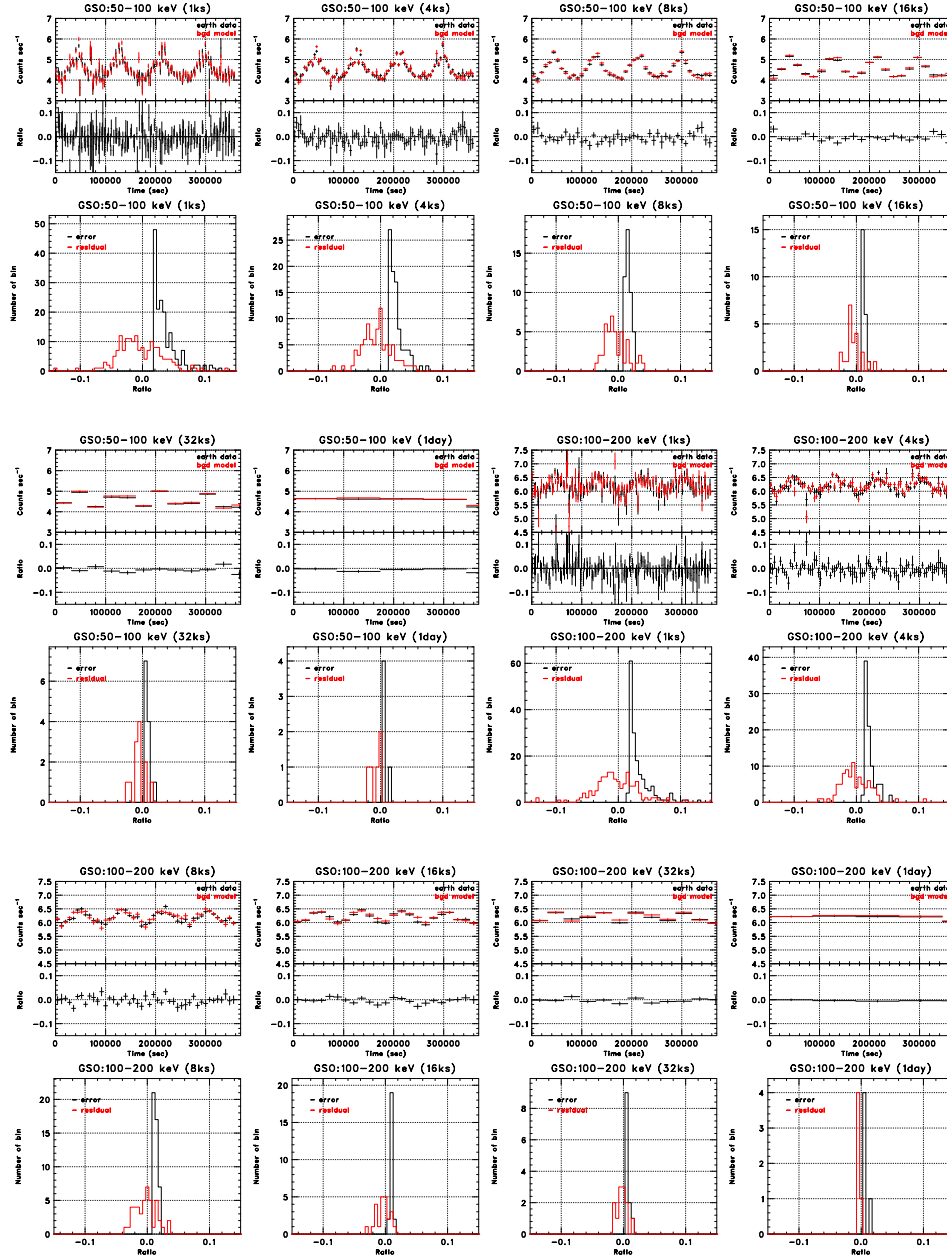
Figure 7.9: Similar plots as figure 7.7, but for the GSO-NXB.
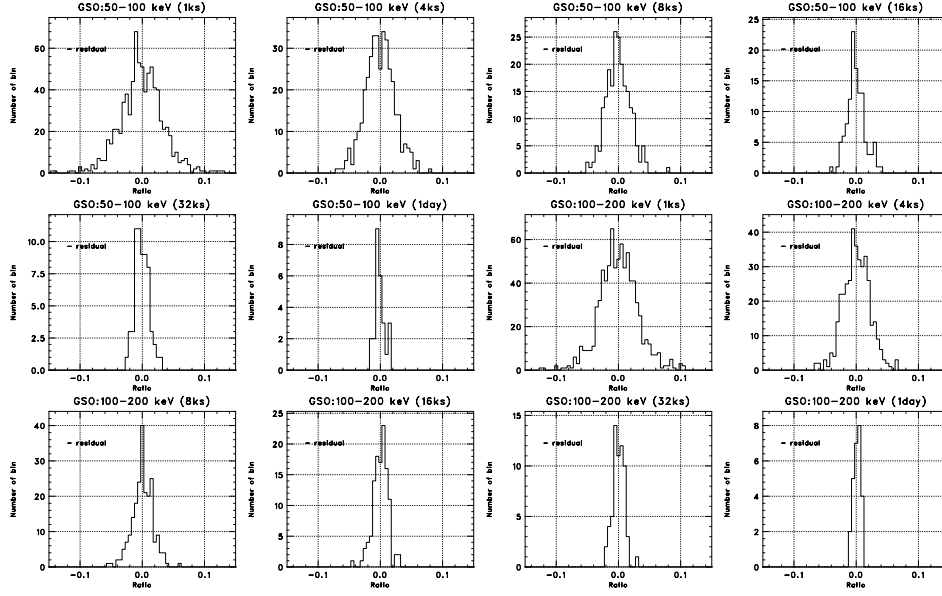
Figure 7.10: Similar to figure 7.8, but for the GSO-NXB.
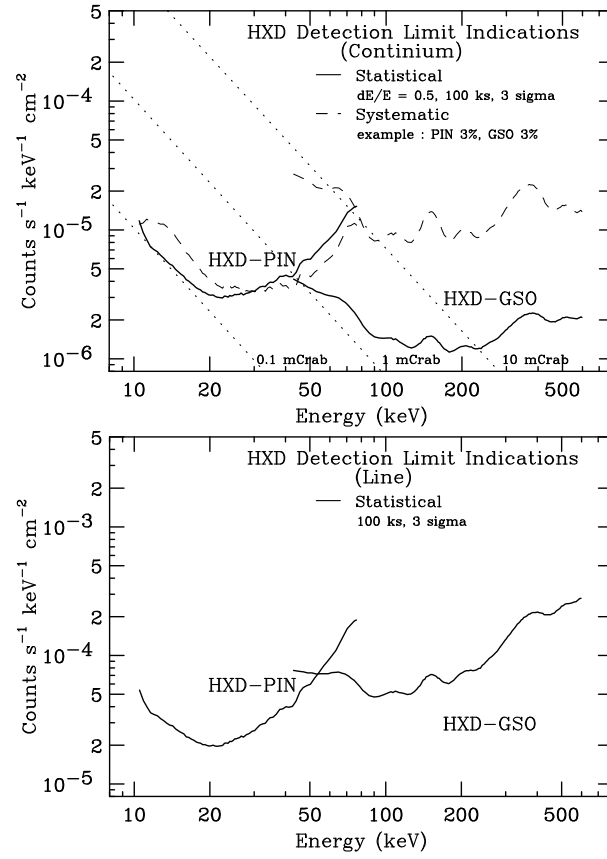
Figure 7.11: Example of detection limit of the HXD, for continuum (left) and for line (right) detection. Solid lines stand for statistical limit, while dashed lines for an example of systematic errors, the value of which should be evaluated by the authors themselves. In the right plot, no systematic error is presented since it is very difficult to evaluate. See also figure 7.5. See text for detail on both plots.

Appendix A

Acronyms

The following table lists acronyms used in this document.

Acronym	Definition
AAVSO	American Association of Variable Stars Observers
AE	Analog Electronics
AO	Announcement of Opportunity
AGN	Active Galactic Nuclei
ARF	Ancillary Response File
ASCA	Advanced Satellite for Cosmology and Astrophysics
ASM	All-Sky Monitor (on *RXTE*)
BGD	Background
BGO	Bismuth Germanate
BI	Back-Illuminated
CALDB	Calibration Database
CCD	Charge-Coupled Device
CI	Charge Ingestion
Co-I	Co-investigator
CPU	Central Processing Unit
CTE	Charge Transfer Efficiency
CTI	Charge Transfer Inefficiency
CXB	Cosmic X–ray Background
DDT	Director Discretionary Time
DE	Digital Electronics
Dec	Declination
DP	Data Processor
DSN	Deep Space Network
EA	Effective Area
EEF	Encircled Energy Function
EOB	Extensible Optical Bench
EPIC	European Photon Imaging Camera (on *XMM-Newton*)
ESA	European Space Agency
FI	Front-Illuminated
FWHM	Full-Width Half-Maximum
FITS	Flexible Image Transport System
FOV	Field Of View
FSA	Frame Store Area
FTOOLS	FITS Tools

Acronym	Definition
GO	Guest Observer
GOF	Guest Observer Facility
GRB	Gamma-Ray Burst
GSFC	Goddard Space Flight Center
GSO	Gadolinium Silicate
HEASARC	High Energy Astrophysics Science Archive Research Center
HESS	High Energy Stereoscopic System
HETG	High Energy Transmission Grating (on *Chandra*)
HEXTE	High Energy X-ray Timing Experiment (on *RXTE*)
HPD	Half-Power Diameter
HRI	High Resolution Imager (on *ROSAT*)
HV	High Voltage
HXD	Hard X–Ray Detector
ISAS	Institute of Space and Astronautical Science
INTEGRAL	INTErnational Gamma-Ray Astrophysics Laboratory
JAXA	Japan Aerospace Exploration Agency
LETG	Low Energy Transmission Grating (on *Chandra*)
LSI	Large Scale Integration
MIT	Massachusetts Institute of Technology
MPU	Main Processing Unit
NRA	NASA Research Announcement
NASA	National Aeronautics and Space Administration
NOI	Notice Of Intent
NSPIRES	NASA Solicitation and Proposal Integrated Review and Evaluation System
NXB	Non-X–ray Background
OBF	Optical Blocking Filter
PDS	Phoswich Detector System (on *Bepppo-SAX*)
PH	Pulse Height
PIN	Positive Intrinsic Negative
PI	Principal Investigator
PI	Pulse Invariant
PIMMS	Portable Interactive Multi-Mission Simulator
PM	Photo-Multiplier
PPU	Pixel Processing Unit
PSF	Point Spread Function
PSPC	Position-Sensitive Proportional Counter (on *ROSAT*)
P-Sum	Parallel-Sum
QDE	Quantum Detection Efficiency
RA	Right Ascension
RAM	Random Access Memory
RDD	Residual Dark-current Distribution
RGS	Reflection Grating Spectrometer (on *XMM-Newton*)
RFA	Research Focus Area
RMF	Redistribution Matrix File
ROSAT	RÖntgen SATellite
RPS	Remote Proposal Submission
RXTE	Rossi X-ray Timing Explorer
SAA	South Atlantic Anomaly

Acronym	Definition
SAX	Satellite per Astronomia X
S/C	Spacecraft
SGR	Soft Gamma-ray Repeater
SLAC	Stanford Linear Accelerator Center
SMC	Small Magellanic Cloud
SN	SuperNova
SWG	Science Working Group
TBD	To Be Determined
TCE	TEC Control Electronics
TCU	Thermal Control Unit
TEC	Thermo-Electric Cooler
TOO	Target Of Opportunity
US	United States
USC	Uchinoura Space Center
UV	Ultra Violet
VHS	Very High State
VSNET	Variable Star NETwork
WAM	Wide-band All-sky Monitor
XIS	X–Ray Imaging Spectrometer
XRB	X-ray Binary
XRS	X–Ray Spectrometer
XRT	X–Ray Telescope
XRT-I	X–Ray Telescope for one of the four XIS detectors

Appendix B

SWG Target List

The SWG target list is presented here twice, sorted both by type of source and by Right Ascension (RA) and Declination (Dec). Details of targets with constraints are listed in the last section. The details of data processing and filtering are still incomplete, so the total time listed for each observation that is already complete is an only an estimate of the actual good time available.

Data from selected sources will be released before the AO is due. The exact list of sources and times to be released has not been finalized; please check the *Suzaku* website listed in Appendix C for more information.

B.1 Targets Sorted by Category

B.1.1 Calibration

Target	RA	Dec	Stat	Exp.	#obs	Remarks
E0102-72	01 04 02.4	-72 01 60.0	Obs	75	2	XIS window open
E0102-72	01 04 02.4	-72 01 60.0		20	1	XIS
N132D	05 25 03.3	-69 38 27.2	Obs	105	6	HXD HV ON
Crab	05 34 32.0	+22 00 52.2	Obs	170	31	
Eta Carina	10 45 03.6	-59 41 04.3		20	1	XIS
Lockman Hole	10 52 00.0	+57 18 00.0		100	1	HXD
North Ecliptic Pole	18 11 12.0	+66 00 0.0	Obs	70	1	
Vega	18 36 56.3	+38 47 01.3	Obs	10	1	Optical light leak check
PKS2155-304	21 58 52.1	-30 13 32.1		60	1	XIS; coordinated obs. with XMM-Newton
Cas A	23 23 24.0	+58 48 54.0		10	1	XIS

99

B.1.2   Gamma-Ray Burst

Target	RA	Dec	Pri.	Exp.	#obs	Remark
GRB AFTERGLOW	00 00 00.0	+00 00 00.0	A(TOO)	150	TBD	

B.1.3   Galactic Compact Objects

Target	RA	Dec	Stat	Exp	#obs	Remark
73P/SW3	01 24 08.4	-10 09 02.		35	2	Constrained, May 2006
AB Dor	05 28 44.7	-65 26 56.0	Obs	5	1	
Eta Carina	10 45 03.6	-59 41 04.2	Obs	35	1	
PSR1509-58	15 13 56.1	-59 08 08.2	Obs	50	1	
X1543-475	15 47 08.6	-47 40 09.		200	10	Constrained TOO in outburst (ASM) one of seven
XTE J1550-564	15 50 58.8	-56 28 35.0		40	1	TOO, VHS of one of two sources
XTE J1550-564	15 50 58.8	-56 28 35.0		200	10	Constrained TOO in outburst (ASM) one of seven
4U1626-67	16 32 16.8	-67 27 42.8	Obs	5	1	
4U1626-67	16 32 16.8	-67 27 43.		100	1	
X1630-472	16 34 01.1	-47 23 34.4		200	10	Constrained TOO in outburst (ASM) one of seven
GRO J1655-40	16 54 00.0	-39 50 44.		40	1	TOO, VHS of one of two sources
Her X-1	16 57 49.8	+35 20 32.6	Obs	30	1	
XTE J1650-500	16 50 01.0	-49 57 45.0		200	10	Constrained TOO in outburst (ASM) one of seven
GRO J1655-40	16 54 0.0	-39 50 42.0	Obs	35	1	
GRO J1655-40	16 54 00.0	-39 50 44.9		200	10	Constrained TOO in outburst (ASM) one of seven
GX 339-4	17 02 49.4	-48 47 22.6		200	10	Constrained TOO in outburst (ASM) one of seven
GX 349+2	17 05 44.5	-36 25 23.		50	1	
RXJ BGD2	17 09 05.0	-41 02 06.0	Obs	30	1	
RXJ BGD1	17 09 31.9	-38 49 22.8	Obs	30	1	
RXJ 1713-3946	17 12 17.0	-39 56 09.6	Obs	60	1	
GX17+2	18 16 01.4	-14 02 09.6	Obs	5	1	
AM Her	18 16 13.3	+49 52 04.8	Obs	10	1	
V4641 SGR	18 19 21.6	-25 24 25.		100	1	TOO, in outburst (VSNET/ASM)
XTE J1859+226	18 58 41.5	+22 39 29.9		200	10	Constrained TOO in outburst (ASM) one of seven
GRS1915+105	19 15 11.6	+10 56 44.2	Obs	80	1	
CH CYG	19 24 13.9	+50 10 11.		60	1	
Cyg X-1	19 58 21.8	+35 12 06.5	Obs	15	1	
73P/SW3	20 26 48.8	+29 44 27.		5	1	Constrained, May 2006
AE AQUARII	20 40 09.2	-00 52 15.		100	1	
73P/SW3	21 20 37.0	+24 41 28.		20	3	Constrained, May 2006
SS CYG	21 42 42.7	+43 35 09.		40	1	
SS CYG	21 42 42.7	+43 35 09.		60	1	TOO, in outburst (AAVSO)

B.1.4 Galactic Diffuse Emission

Target	RA	Dec	Stat	Exp	#obs	Remark
Tycho center	00 25 20.4	+64 08 16.		100	1	
Tycho offset	00 47 00.0	+65 30 00.		50	1	
SMC DIFFUSE 1	00 52 09.6	-72 49 48.		50	1	
E0102-72	01 04 02.4	-72 01 59.9	Obs	25	1	
MBM12	02 55 50.0	+19 30 10.		100	1	
DEM L71/N23	05 05 46.4	-67 56 43.1	Obs	40	1	
N103B	05 08 54.3	-68 44 17.9	Obs	35	1	
SN 1987A	05 35 28.0	-69 16 11.		40	1	
A0535+26	05 38 54.5	26 18 57.6	Obs	20	1	
RXJ 0852-4622 NW	08 48 58.0	-45 39 03		200	1	
HESS J1616-508-BGD	16 14 38.8	-51 10 34.7	Obs	20	1	
HESS J1616-508	16 16 29.0	-50 53 58.2	Obs	45	1	
HESS J1616-508-BGD2	16 17 50.9	-50 41 27.6	Obs	20	1	
RCW86 SW	14 41 08.6	-62 40 25.		100	1	
SN1006 SW-BG	14 58 36.0	-42 24 00.0	Obs	35	1	
SN1006 SW-rim	15 02 00.0	-42 4 12.0	Obs	50	1	
SN1006 NW	15 02 33.6	-41 48 00.		50	1	
SN1006 SE	15 03 28.8	-42 04 48.		50	1	
SN1006 NE-rim	15 03 50.4	-41 46 48.0	Obs	50	1	
SN1006 NE-BG	15 06 48.0	-41 24 00.0	Obs	50	1	
Galactic Bulge	15 45 43.2	-31 41 59.3	Obs	60	1	
North Polar Spur	17 22 21.0	+ 4 45 23.8	Obs	35	1	
Sgr C	17 44 37.3	-29 28 10.		100	1	
Gal Center Bgd2	17 44 49.0	-29 21 07.2	Obs	10	2	
Sgr C Bgd	17 44 56.2	-29 45 52.		10	1	
Gal Center Src2	17 45 12.7	-29 10 15.6	Obs	75	2	
Gal Center Src1	17 46 02.6	-28 55 33.6	Obs	70	2	
Gal Center Bgd1	17 46 05.5	-29 30 54.0	Obs	10	2	
Gal Center Bgd1	17 46 05.5	-29 30 54.0	Obs	5	1	
Gal Center Bgd3	17 46 21.6	-28 39 03.6	Obs	10	2	
Galactic Center 2	17 47 05.4	-28 37 52.		100	1	
Sgr B2	17 47 30.1	-28 26 27.2	Obs	60	1	
GC Sgr B2 Bgd	17 48 22.2	-28 07 58.8	Obs	10	1	
Galactic Bulge 2	18 02 29.0	-29 35 10.		10	1	
HESS J1804-216 BG	18 03 50.4	-22 01 27.		50	1	
HESS J1804-216	18 04 41.1	-21 40 33.		50	1	
Galactic Bulge 3	18 18 50.0	-31 29 09.		50	1	
Galactic Ridge	18 44 00.0	-04 04 12.		100	1	
Galactic Bulge 6	18 50 45.0	-33 53 34.		10	1	
BD+30.3639	19 34 45.1	30 30 57.6	Obs	30	1	
Cyg Loop	20 53 57.5	+32 22 24.		20	1	Roll constrained
Cyg Loop	20 54 59.1	+32 11 17.		20	1	Roll constrained
Cyg Loop	20 55 49.2	+31 57 39.		20	1	Roll constrained
Cyg Loop	20 56 42.3	+31 44 43.		20	1	Roll constrained
Cas A	23 23 24.0	58 48 54.0	Obs	20	1	

B.1.5 Extragalactic Compact Sources

Target	RA	Dec	Stat	Exp	#obs	Remark
GRB TOO	00 00 00.0	+00 00 00.		150	3	
NGC 1313 ULX	03 18 15.4	-66 31 59.9	Obs	40	1	
3C120	04 33 11.1	+05 21 15.		160	4	
NGC 2110	05 52 11.4	-07 27 22.0	Obs	85	1	
1H 0707-495	07 08 41.5	-49 33 06.		100	1	
SWIFT J0746.3+254	07 46 25.9	+25 49 02.		100	1	
0836+714	08 41 24.3	+70 53 41.		50	1	
NGC 2992	09 45 42.1	-14 19 35.		120	3	Constrained
MCG-5-23-16	09 47 40.1	-30 56 56.		100	1	
1ES1101-232	11 03 37.6	-23 29 30.		80	1	HESS TOO, 2 of 6
MRK 421	11 04 27.3	+38 12 31.		80	1	HESS TOO, 2 of 6
NGC 3516	11 06 47.5	+72 34 07.0	Obs	100	1	
NGC 4051	12 03 09.6	+44 31 53.		150	1	
PG 1211+143	12 14 17.7	+14 03 13.		100	1	
NGC 4945	13 05 27.5	-49 28 05.5	Obs	15	1	
NGC 4945	13 05 27.5	-49 28 05.5	Obs	15	1	
Cen A	13 25 27.6	-43 01 08.8	Obs	40	1	
MCG-6-30-15	13 35 53.8	-34 17 44.		300	4	
MCG-6-30-15	13 35 54.0	-34 17 42.4	Obs	50	1	
ARP220	15 34 57.1	+23 30 11.		100	1	
Mkn 501	16 53 52.2	+39 45 37		80	1	HESS TOO, 2 of 6
QSO1727+5	17 28 18.3	+50 13 09.8	Obs	3	1	
PKS 2005-489	20 09 25.4	-48 49 53.		80	1	HESS TOO, 2 of 6
PKS2155-304	21 58 52.1	-30 13 32.		80	1	HESS TOO, 2 of 6
H 2356-309	23 59 07.8	-30 37 37.		80	1	HESS TOO, 2 of 6

B.1.6   Extragalactic Diffuse Sources

Target	RA	Dec	Stat	Exp	#obs	Remark
ABELL2801	00 38 31.3	-29 02 47.		25	1	
ABELL2804	00 39 38.7	-28 53 21.		25	1	
ABELL2811-OFF	00 40 54.0	-28 42 57.		25	1	
ABELL2811	00 42 09.3	-28 32 33.		25	1	
NGC 720	01 53 00.5	-13 44 19.		100	1	
A426	03 19 48.1	+41 30 42.		50	1	
Fornax Cluster	03 38 34.6	-35 29 07.8	Obs	50	1	
Fornax Cluster NO	03 38 34.6	-35 14 07.		80	1	
A3376 WEST RELIC	06 00 00.0	-40 02 00.		150	1	
ABELL 3376	06 02 15.0	-39 57 00.0	Obs	130	1	
NGC 2403	07 36 51.4	+65 36 09		70	1	
M82 Wind	09 55 28.5	+69 45 19.4	Obs	20	1	
A1060	10 36 24.0	-27 31 35.		40	1	
A1060 OFFSET	10 37 45.0	-27 31 35.		60	1	
A1413	11 55 18.9	+23 38 31.		100	1	
NGC 4388	12 25 46.9	+12 39 43.		100	1	
NGC 4636	12 42 54.0	+02 45 07.		80	1	
CENTAURUS CLUSTER	12 48 49.3	-41 18 40.		30	1	
CENCL OFFSET1	12 48 49.3	-41 26 38.		40	1	
CENCL OFFSET2	12 48 49.3	-41 10 40.		40	1	
HCG62	12 53 06.0	-09 12 15.		100	1	
ABELL 1795	13 48 52.6	+26 35 31.		120	1	
A2052	15 16 45.5	+07 00 01.1	Obs	15	1	$(+7',+7')$
A2052	15 16 45.5	+07 00 01.1	Obs	20	1	$(-7',+7')$
A2052	15 16 45.5	+07 00 01.1	Obs	10	1	$(-7',-7')$
A2052	15 16 45.5	+07 00 01.1	Obs	15	1	$(+7',-7')$
A2218 offset	16 17 48.0	+65 27 36.0	Obs	35	1	
A2218	16 35 54.2	+66 12 59.8	Obs	35	1	
A2218 offset B	16 39 30.8	+65 13 31.2		50	1	
A2312	18 53 48.2	+68 23 06.0	Obs	4	1	

B.2   Targets Sorted by RA

Abbrev.	Target Type
GRB	Gamma-Ray Burst
CAL	Calibration
GDE	Galactic Diffuse Emission
GCS	Galactic Compact Sources
EDS	Extragalactic Diffuse Sources
ECS	Extragalactic Compact Sources

Target	RA	Dec	Cat	Stat	Exp.	#obs
GRB AFTERGLOW	00 00 00.0	+00 00 00.0	GRB		150	3
ABELL2811	00 42 09.3	-28 32 33.	EDS		25	1
ABELL2811-OFF	00 40 54.0	-28 42 57.	EDS		25	1
ABELL2804	00 39 38.7	-28 53 21.	EDS		25	1
ABELL2801	00 38 31.3	-29 02 47.	EDS		25	1
Tycho center	00 25 20.4	+64 08 16.	GDE		100	1
Tycho offset	00 47 00.0	+65 30 00.	GDE		50	1
SMC DIFFUSE 1	00 52 09.6	-72 49 48.	GDE		50	1
E0102-72	01 04 02.4	-72 01 60.0	CAL	Obs	75	2
E0102-72	01 04 02.4	-72 01 60.0	CAL		20	1
E0102-72	01 04 02.4	-72 01 60.0	GDE	Obs	25	1
73P/SW3	01 24 08.4	-10 09 02.	GCS		35	2
NGC720	01 53 00.5	-13 44 19.	EDS		100	1
MBM12	02 55 50.0	+19 30 10.	GDE		100	1
NGC 1313 ULX	03 18 15.4	-66 31 59.9	ECS	Obs	40	1
A426	03 19 48.1	+41 30 42.	EDS		50	1
Fornax Cluster	03 38 34.6	-35 29 07.8	EDS	Obs	50	1
FORNAX CLUSTER NO	03 38 34.6	-35 14 07.	EDS		80	1
3C120	04 33 11.1	+05 21 15.	ECS		160	4
DEM L71/N23	05 05 46.4	-67 56 43.1	GDE	Obs	40	1
N103B	05 08 54.3	-68 44 17.9	GDE	Obs	35	1
N132D	05 25 03.3	-69 38 27.2	CAL	Obs	105	6
AB Dor	05 28 44.7	-65 26 56.0	GCS	Obs	5	1
Crab	05 34 32.0	+22 00 52.2	CAL	Obs	170	31
SN 1987A	05 35 28.0	-69 16 11.	GDE		40	1
A0535+26	05 38 54.5	26 18 57.6	GDE	Obs	20	1
NGC 2110	05 52 11.4	-07 27 22.0	ECS	Obs	85	1
A3376 WEST RELIC	06 00 00.0	-40 02 00.	EDS		150	1
ABELL 3376	06 02 15.0	-39 57 00.0	EDS	Obs	130	1

Target	RA	Dec	Cat	Stat	Exp.	#obs
1H 0707-495	07 08 41.5	-49 33 06.	ECS		100	1
NGC 2403	07 36 51.4	+65 36 09		70	1	
SWIFT J0746.3+254	07 46 25.9	+25 49 02.	ECS		100	1
0836+714	08 41 24.3	+70 53 41.	ECS		50	1
RXJ 0852-4622 NW	08 48 58.0	-45 39 03	GDE		200	1
NGC 2992	09 45 42.1	-14 19 35.	ECS		120	3
MCG-5-23-16	09 47 40.1	-30 56 56.	ECS		100	1
M82 Wind	09 55 28.5	+69 45 19.4	EDS	Obs	20	1
Eta Carina	10 45 03.6	-59 41 04.3	CAL		20	1
Eta Carina	10 45 03.6	-59 41 04.3	GCS	Obs	35	1
Lockman Hole	10 52 00.0	+57 18 00.0	CAL		100	1
A1060	10 36 24.0	-27 31 35.	EDS		40	1
A1060 OFFSET	10 37 45.0	-27 31 35.	EDS		60	1
1ES1101-232	11 03 37.6	-23 29 30.	ECS		80	1 (TOO,2/6)
MRK 421	11 04 27.3	+38 12 31.	ECS		80	1 (TOO,2/6)
NGC 3516	11 06 47.5	+72 34 07.0	ECS	Obs	100	1
A1413	11 55 18.9	+23 38 31.	EDS		100	1
NGC 4051	12 03 09.6	+44 31 53.	ECS		150	1
PG 1211+143	12 14 17.7	+14 03 13.	ECS		100	1
NGC4388	12 25 46.9	+12 39 43.	EDS		100	1
NGC4636	12 42 54.0	+02 45 07.	EDS		80	1
CENTAURUS CLUSTER	12 48 49.3	-41 18 40.	EDS		30	1
CENCL OFFSET1	12 48 49.3	-41 26 38.	EDS		40	1
CENCL OFFSET2	12 48 49.3	-41 10 40.	EDS		40	1
HCG62	12 53 06.0	-09 12 15.	EDS		100	1
Cen A	13 25 27.6	-43 1 08.8	ECS	Obs	40	1
NGC 4945	13 05 27.5	-49 28 05.5	ECS	Obs	15	1
NGC 4945	13 05 27.5	-49 28 05.5	ECS	Obs	15	1
MCG-6-30-15	13 35 53.8	-34 17 44.	ECS		300	4
MCG-6-30-15	13 35 54.0	-34 17 42.4	ECS	Obs	50	1
ABELL 1795	13 48 52.6	+26 35 31.	EDS		120	1
RCW86 SW	14 41 08.6	-62 40 25.	GDE		100	1
SN1006 SW-BG	14 58 36.0	-42 24 00.0	GDE	Obs	35	1
SN1006 SW-rim	15 02 00.0	-42 4 12.0	GDE	Obs	50	1
SN1006 NW	15 02 33.6	-41 48 00.	GDE		50	1
SN1006 SE	15 03 28.8	-42 04 48.	GDE		50	1
SN1006 NE-rim	15 03 50.4	-41 46 48.0	GDE	Obs	50	1
SN1006 NE-BG	15 06 48.0	-41 24 00.0	GDE	Obs	50	1
PSR1509-58	15 13 56.1	-59 08 08.2	GCS	Obs	50	1
A2052	15 16 45.5	+07 00 01.1	EDS	Obs	15	1
A2052	15 16 45.5	+07 00 01.1	EDS	Obs	20	1
A2052	15 16 45.5	+07 00 01.1	EDS	Obs	10	1
A2052	15 16 45.5	+07 00 01.1	EDS	Obs	15	1
ARP220	15 34 57.1	+23 30 11.	ECS		100	1
Galactic Bulge	15 45 43.2	-31 41 59.3	GDE	Obs	60	1
X1543-475	15 47 08.6	-47 40 09.	GCS		200	10 (TOO,1/7)
XTE J1550-564	15 50 58.8	-56 28 35.0	GCS		200	10 (TOO,1/7)
XTE J1550-564	15 50 58.8	-56 28 35.0	GCS		40	1 (TOO,1/2)

Target	RA	Dec	Cat	Stat	Exp.	#obs
HS J1616-508-BGD	16 14 38.8	-51 10 34.7	GDE	Obs	20	1
HESS J1616-508	16 16 29.0	-50 53 58.2	GDE	Obs	45	1
A2218 offset	16 17 48.0	+65 27 36.0	EDS	Obs	35	1
A2218 offset B	16 39 30.8	+63 13 31.2	EDS		50	1
HS J1616-508-BGD2	16 17 50.9	-50 41 27.6	GDE	Obs	20	1
4U1626-67	16 32 16.8	-67 27 43.	GCS		100	1
4U1626-67	16 32 16.8	-67 27 42.8	GCS	Obs	5	1
X1630-472	16 34 01.1	-47 23 34.4	GCS		200	10 (TOO,1/7)
A2218	16 35 54.2	+66 12 59.8	EDS	Obs	85.9	1
XTE J1650-500	16 50 01.0	-49 57 45.0	GCS		200	10 (TOO,1/7)
Mkn 501	16 53 52.2	+39 45 37	ECS		80	1 (TOO,2/6)
GRO J1655-40	16 54 00.0	-39 50 44.	GCS		40	1 (TOO,1/2)
GRO J1655-40	16 54 00.0	-39 50 44.9	GCS		200	10 (TOO,1/7)
GRO J1655-40	16 54 00.0	-39 50 42.0	GCS	Obs	35	1
Her X-1	16 57 49.8	+35 20 32.6	GCS	Obs	30	1
GX 339-4	17 02 49.4	-48 47 22.6	GCS		200	10 (TOO,1/7)
GX 349+2	17 05 44.5	-36 25 23.	GCS		50	1
RXJ BGD2	17 09 05.0	-41 02 06.0	GCS	Obs	30	1
RXJ BGD1	17 09 31.9	-38 49 22.8	GCS	Obs	30	1
RXJ 1713-3946	17 12 17.0	-39 56 09.6	GCS	Obs	60	1
North Polar Spur	17 22 21.0	+04 45 23.8	GDE	Obs	35	1
QSO1727+5	17 28 18.3	+50 13 09.8	ECS	Obs	3	1
Sgr C	17 44 37.3	-29 28 10.	GDE		100	1
Gal Center Bgd2	17 44 49.0	-29 21 07.2	GDE	Obs	10	2
Sgr C Bgd	17 44 56.2	-29 45 52.	GDE		10	1
Gal Center Src2	17 45 12.7	-29 10 15.6	GDE	Obs	75	2
Gal Center Src1	17 46 02.6	-28 55 33.6	GDE	Obs	70	2
Gal Center Bgd1	17 46 05.5	-29 30 54.0	GDE	Obs	10	2
Gal Center Bgd3	17 46 21.6	-28 39 03.6	GDE	Obs	10	2
Galactic Center 2	17 47 05.4	-28 37 52.	GDE		100	1
Sgr B2	17 47 30.1	-28 26 27.2	GDE	Obs	60	1
GC Sgr B2 Bgd	17 48 22.2	-28 07 58.8	GDE	Obs	10	1
N. Ecliptic Pole	18 11 12.0	+66 00 00.0	CAL	Obs	70	1
GX17+2	18 16 01.4	-14 02 09.6	GCS	Obs	5	1
AM Her	18 16 13.3	+49 52 04.8	GCS	Obs	10	1
V4641 SGR	18 19 21.6	-25 24 25.	GCS		100	1 (TOO)
Vega	18 36 56.3	+38 47 01.3	CAL	Obs	10	1
A2312	18 53 48.2	+68 23 06.0	EDS	Obs	4	1
Galactic Bulge 2	18 02 29.0	-29 35 10.	GDE		10	1
HESS J1804-216 BG	18 03 50.4	-22 01 27.	GDE		50	1
HESS J1804-216	18 04 41.1	-21 40 33.	GDE		50	1
Galactic Bulge 3	18 18 50.0	-31 29 09.	GDE		50	1
Galactic Ridge	18 44 00.0	-04 04 12.	GDE		100	1
Galactic Bulge 6	18 50 45.0	-33 53 34.	GDE		10	1
XTE J1859+226	18 58 41.5	+22 39 29.9	GCS		200	10 (TOO,1/7)
GRS1915+105	19 15 11.6	+10 56 44.2	GCS	Obs	80	1
CH CYG	19 24 13.9	+50 10 11.	GCS		60	1
BD+30.3639	19 34 45.1	30 30 57.6	GDE	Obs	30	1
Cyg X-1	19 58 21.8	+35 12 06.5	GCS	Obs	15	1

Target	RA	Dec	Cat	Stat	Exp.	#obs
PKS 2005-489	20 09 25.4	-48 49 53.	ECS		80	1 (TOO,2/6)
73P/SW3	20 26 48.8	+29 44 27.	GCS		5	1
AE AQUARII	20 40 09.2	-00 52 15.	GCS		100	1
Cyg Loop	20 53 57.5	+32 22 24.	GDE		20	1
Cyg Loop	20 54 59.1	+32 11 17.	GDE		20	1
Cyg Loop	20 55 49.2	+31 57 39.	GDE		20	1
Cyg Loop	20 56 42.3	+31 44 43.	GDE		20	1
73P/SW3	21 20 37.0	+24 41 28.	GCS		20	3
SS CYG	21 42 42.7	+43 35 09.	GCS		40	1
SS CYG	21 42 42.7	+43 35 09.	GCS		60	1 (TOO)
PKS2155-304	21 58 52.1	-30 13 32.1	CAL		60	1
PKS2155-304	21 58 52.1	-30 13 32.	ECS		80	1 (TOO,2/6)
Cas A	23 23 24.0	+58 48 54.0	CAL		10	1
Cas A	23 23 24.0	58 48 54.0	GDE	Obs	20	1
H 2356-309	23 59 07.8	-30 37 37.	ECS		80	1 (TOO,2/6)

Appendix C

Important Web/e-mail addresses

Primary *Suzaku* **Sites**

Japan: `http://www.astro.isas.jaxa.jp/suzaku/`

US : `http://suzaku.gsfc.nasa.gov/`

ESA: `http://www.rssd.esa.int/suzaku`

Suzaku **GOF:**

`http://suzaku.gsfc.nasa.gov/`

The "Proposal & Tools" button is of particular note.

Tools:

Viewing	`http://heasarc.gsfc.nasa.gov/Tools/Viewing.html`
PIMMS	`http://heasarc.gsfc.nasa.gov/docs/software/tools/pimms.html`
MAKI	`http://heasarc.gsfc.nasa.gov/Tools/maki/maki.html`
XSPEC	`http://heasarc.gsfc.nasa.gov/docs/xanadu/xspec/index.html`
WebPIMMS	`http://heasarc.gsfc.nasa.gov/Tools/w3pimms.html`
WebSPEC	`http://heasarc.gsfc.nasa.gov/webspec/webspec.html`

Questions:

The US GOF can be reached using the web form available at the bottom of every page within the Suzaku GOF site.

Technical Description

Japan: `http://www.astro.isas.jaxa.jp/suzaku/research/proposal/ao2/`

US: `http://suzaku.gsfc.nasa.gov/docs/suzaku/prop_tools/suzaku_td/`

ESA: `http://www.rssd.esa.int/index.php?project=ASTROE2&page=AODocs`

US (ftp): `ftp://legacy.gsfc.nasa.gov/suzaku/nra_info/suzaku_td.ps.gz`

Accepted Target List

Japan: `http://www.astro.isas.jaxa.jp/suzaku/research/accept/`

US: `http://heasarc.gsfc.nasa.gov/docs/suzaku/tlminfo/ao1list.html`

RPS (for Japanese proposals)

`http://rps.astro.isas.jaxa.jp/cgi-bin/RPS/SUZAKU/RPS.pl`

RPS (for US proposals)

`http://heasarc.gsfc.nasa.gov/akbar/suzaku/`

RPS (for ESA proposals)

`http://www.rssd.esa.int/RPS/SUZAKU/RPS.pl`

(Or email `rps@rssd.esa.int`)